

Ultrasonic Detection of Acoustically Transparent Cracks Using Harmonics

PROEFSCHRIFT

ter verkrijging van de graad van doctor
aan de Technische Universiteit Delft,
op gezag van de Rector Magnificus Prof. ir. K.C.A.M. Luyben,
voorzitter van het College voor Promoties,
in het openbaar te verdedigen
op vrijdag 21 februari 2014 om 12:30 uur

door

Khalid CHOUGRANI

natuurkundig ingenieur
geboren te Aklim, Marokko

Dit proefschrift is goedgekeurd door de promotor:
Prof. dr. ir. A. Gisolf

Samenstelling promotiecommissie:

Rector Magnificus,	voorzitter
Prof.dr.ir. A. Gisolf,	Technische Universiteit Delft, promotor
Prof.dr.ir. I. Solodov,	University of Stuttgart
Prof.dr.ir. R. Benedictus,	Technische Universiteit Delft
Prof.dr. I.M. Richardson,	Technische Universiteit Delft
Dr.ir. D.J. Verschuur,	Technische Universiteit Delft
Dr.ir. A.W.F. Volker,	TNO
Dr.ir. M.C.M. Bakker,	Technische Universiteit Delft
Prof.dr. H.P. Urbach,	Technische Universiteit Delft, reservelid

ISBN 978-94-6186-280-8

Copyright © 2014, by K. Chougrani

Laboratory of Acoustical Wavefield Imaging, Faculty of Applied Sciences, Delft University of Technology, P.O. Box 5046, 2600 GA, Delft, The Netherlands.

All rights reserved. No part of this publication may be reproduced, stored in a retrieval system or transmitted in any form or by any means, electronic, mechanical, photocopying, recording or otherwise, without the prior written permission of the author.

SUPPORT

This research is financially supported by Applus RTD.

Typesetting system: L^AT_EX.

Published by Uitgeverij BOXPress, 's-Hertogenbosch, The Netherlands.

Printed by Proefschriftmaken.nl

Contents

1	Introduction	5
1.1	Nondestructive testing	5
1.2	Ultrasonic inspection	5
1.2.1	Conventional techniques	5
1.2.2	Imaging techniques	8
1.3	Non-linear acoustics	10
1.4	Fatigue of materials	10
1.4.1	Crack initiation and growth	11
1.4.2	Fracture modes and crack closure	11
1.5	Limitations of the current inspection approach	11
1.6	Thesis objective and outline	13
2	Theoretical formulation	15
2.1	Contact between solids	15
2.1.1	Introduction to atomic bonds	15
2.1.2	Van der Waals forces	15
2.1.3	Contact models	17
2.2	Non-linear signature of a contacting interface	18
2.3	Numerical modeling	19
2.3.1	Mass-spring lattice model	19
2.3.2	Implementation of van der Waals in an MSLM scheme	22
3	Numerical results	26
3.1	Material displacement	26
3.2	Crack transparency and harmonic generation	26
4	Experiments	42
4.1	Artificial crack interface	42
4.1.1	Experimental setup	42
4.1.2	Interface closure	42
4.1.3	Detection of harmonics	45
4.2	Fatigue crack interface	50
4.2.1	Fatiguing of a test specimen	50
4.2.2	Crack closure and harmonic generation	51
4.2.3	Harmonic detection along the crack length	57

4.3	Comparison with theoretical formulation	72
4.3.1	Crack closure	72
4.3.2	Harmonic generation	72
5	Conclusions and recommendations	77
5.1	Conclusions	77
5.2	Recommendations	78
	Appendices	81
A	Symbols and abbreviations	81
A.1	Symbols	81
A.2	Abbreviations	82
	Appendices	84
B	Derivation of van der Waals stress	84
	Appendices	87
C	Magnitude of harmonics at various loads and fixed excitation voltages	87
C.1	Reflected harmonics	88
C.2	Transmitted harmonics	93
	Appendices	98
D	Power spectra at various excitation voltages and a fixed load	98
D.1	Reflection	99
D.2	Transmission	104
	Summary	113
	Samenvatting	115
	Curriculum vitae	117
	Acknowledgements	118
	Index	120

Chapter 1

Introduction

1.1 Nondestructive testing

For many years nondestructive testing (NDT) has been playing a vital role in safety of humans, assets and the environment. Furthermore, NDT contributes substantially to the safety and prosperity of our society. Advances in technology have led to improvements of NDT instrumentation, by which complex parts of various assets can be inspected for damage and anomalies. NDT is continuously applied in industries using critical components, such as in aerospace, nuclear and petrochemical applications.

NDT covers a wide range of methods by which materials, such as steel components, can be examined without influencing their physical properties. For instance, in petrochemical industry, ultrasonic testing (UT) and radiography testing (RT) are extensively utilized and well accepted methods for the inspection of different assets, such as pressure vessels, storage tanks and pipelines.

Over the last decades, an increased demand has been observed for emerging technologies aiming at improving existing inspection approaches. To this end, UT and RT techniques have been improved and new imaging techniques have been introduced since the implementation of ultrasonic array technology and digital X-ray sensors in the NDT field. Furthermore, due to restrictions dictated by governmental bodies regarding the quality of new assets, the use of new materials and their maintenance, advanced technologies are required for a better defect detection, sizing, and characterization.

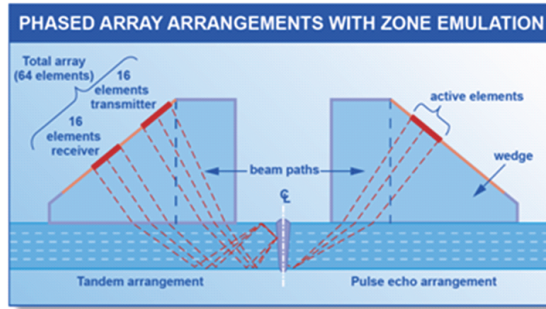
1.2 Ultrasonic inspection

1.2.1 Conventional techniques

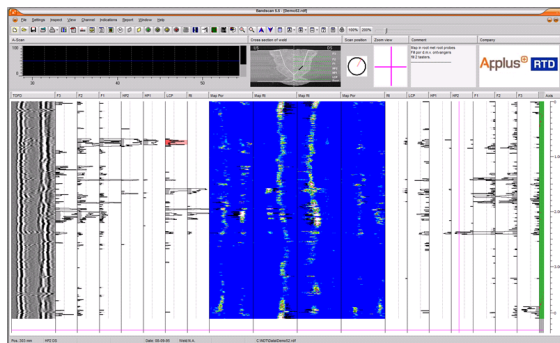
Ultrasonic examination is mainly based on the use of ultrasonic waves generated by piezoelectric elements (Krautkrämer 1977, Kuttruff 1991). Depending on the application, different wave types and probe configurations can be chosen, by which reflection and diffraction signals can be exploited for detection and sizing of defects. Techniques,

such as pulse echo (PE), time of flight diffraction (ToFD) and phased array (PA) are widely used to this purpose. Based on the inspection requirements, a combination of these techniques might be required. The main advantage of this combination is increasing the probability of detection of a defect and improving sizing accuracy.

For the PE technique, reflected waves resulting from discontinuities and material boundaries are exploited using different probe arrangements. For instance, a single probe can be used as a transmitter and as a receiver simultaneously, or arranged in the so-called tandem configuration, where one probe is transmitting and the other one is receiving (Figure 1.1a). The tandem technique was first introduced for the inspection of heavy-wall steel components and then extended to the inspection of nuclear assets (de Raad & Dijkstra 2007, Dijkstra 2012). Nowadays, the tandem technique benefits from the array technology and it is adopted for automatic ultrasonic testing (AUT) of girth welds in new construction pipelines (Ginzel 2006, de Raad & Dijkstra 2007). Figure 1.1b shows an example of a strip chart data presentation used in AUT inspection.



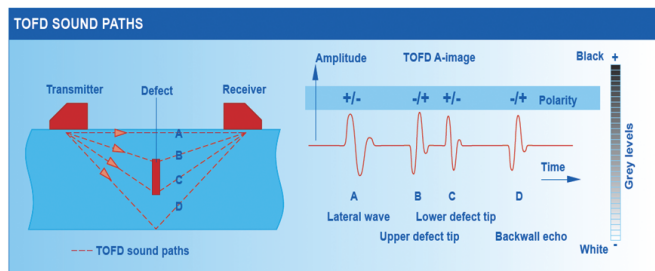
(a)



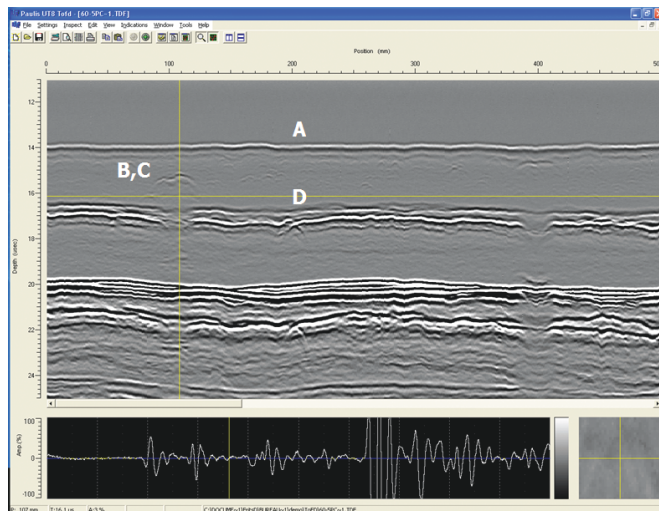
(b)

Figure 1.1: Pulse echo and tandem arrangements using phased array probes (a) and a typical strip chart data display as used in AUT inspection (b). The vertically oriented strips represent ultrasonic signals received from different areas of interest within the weld.

The ToFD technique, developed in the seventies (Charlesworth & Temple 2001), is nowadays widely accepted and used in both new construction and in-service applications. ToFD mainly uses compressional waves and it gains its sizing accuracy from signals resulting from tip diffractions (Ravenscroft et al. 1991). A typical ToFD arrangement is depicted in Figure 1.2a, where a pair of probes (transmitter and receiver) are held at a fixed separation distance from a weld centerline. Based on differences between travel times along different sound paths, accurate defect positioning and sizing can be achieved. Signals collected by such a configuration are stacked together in the so-called B-scan presentation as shown in the example of Figure 1.2b.



(a)



(b)

Figure 1.2: ToFD probe arrangement with relevant signals (a) and an example of data display in B-scan presentation (b). Labels A, B, C, and D correspond to lateral wave, upper tip diffraction, lower tip diffraction, and back-wall echo, respectively.

In medical imaging, the PA technique is successfully implemented and widely used for diagnostics (Wells 2000). In this technique, sectorial scans are commonly performed by steering the angle, focal depth and index point of ultrasonic beams using phased array probes (Figure 1.3a). Benefiting from the flexibility of ultrasonic arrays and visualization possibilities, inspection of objects in NDT becomes feasible and more attractive (Olympus 2004), especially in cases of limited accessibility. A PA sectorial scan contains reflection and/or diffraction signals, which can be used for detection and sizing purposes. In Figure 1.3b, an example of a PA sectorial scan data is displayed.

1.2.2 Imaging techniques

Thanks to advances in computers and array technology, new imaging approaches, such as the total focusing method (TFM), the sampling phased array (SPA) and the inverse wave field extrapolation (IWEX), have shown a great potential for defect detection and sizing, using well-developed reconstruction algorithms (Holmes et al. 2005, Pörtzgen et al. 2007,

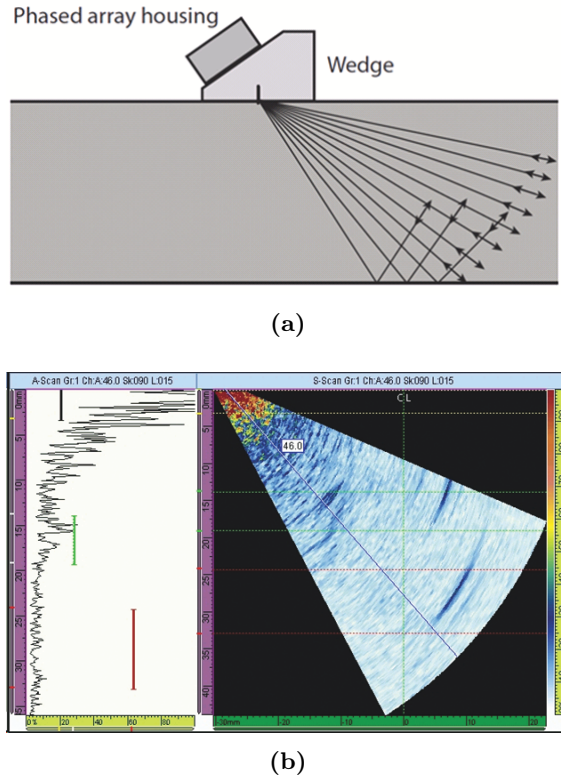


Figure 1.3: Schematic of a PA probe arrangement (a) and an example of data display in sectorial scan presentation (b). By sweeping the ultrasonic beam, a weld volume can be inspected.

Verkooijen & Boulavinov 2005, Hörchens et al. 2013). For instance, in IWEX an actual image can be obtained rather than a plot of the collected signals as in the case of the conventional approach, including the PA sectorial scan. Recently, IWEX technology has been implemented for girth weld inspection, as the next generation of AUT imaging-based inspection. In this technique, measurements are performed by firing one single element and receiving with all elements (Figure 1.4a). By repeating the same experiment for all source elements, a data set can be gathered and further processed using the IWEX algorithm (Pörtzgen 2007). For an array with N elements, a data set of N^2 traces is obtained. A typical example of an IWEX data image is displayed in Figure 1.4b, where a weld geometry and an embedded vertically oriented artificial defect are imaged. It

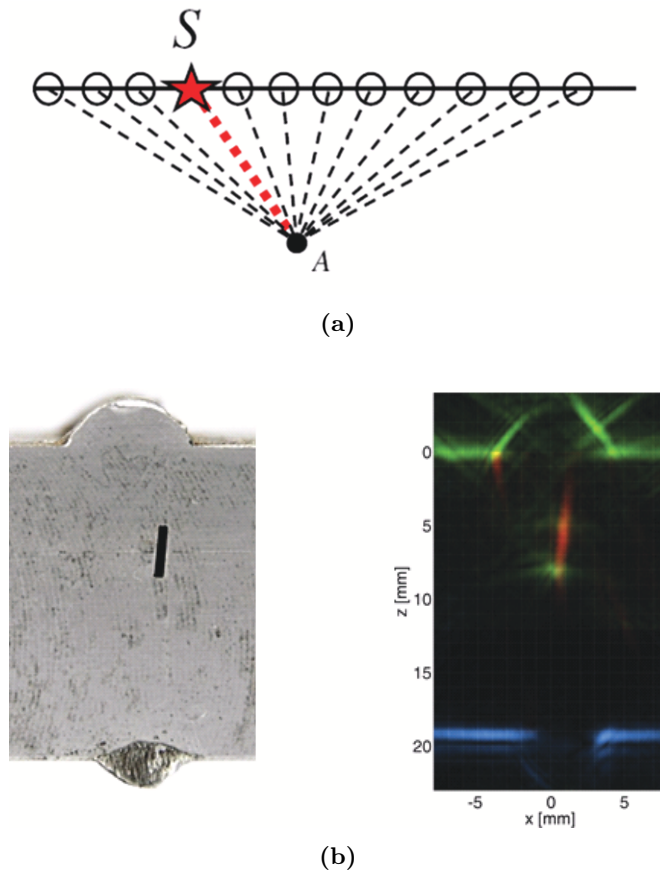


Figure 1.4: IWEX principle (a) and a macro photograph with an actual image of an artificial embedded defect (b). S stands for a source element and A represents an imaging point in the volume (Gisolf & Verschuur 2011). In this configuration, one array element is used as a source and all array elements as receivers. This procedure is repeated for all source-receiver combinations.

should be noticed that IWEX data contains reflection and diffraction signals arising from discontinuities and material boundaries, for of all source-receiver combinations.

1.3 Non-linear acoustics

For many decades, non-linear acoustics has been studied and applied in different fields, such as material characterization, medical imaging, acoustic microscopy, and non-destructive testing (Zheng et al. 2000). In this approach, non-linear effects resulting from the interaction of ultrasonic waves with the object under inspection are exploited. In medical diagnostics, for instance, harmonics arising from the wave propagation in the medium are recorded and used for the so-called harmonic imaging. Nowadays, this technique is widely used in medical imaging, since it provides major improvements of the image quality, when compared to conventional techniques (Shapiro et al. 1998, Bouakaz & de Jong 2003). For material characterization and evaluation, non-linear acoustics has proven to be a sensitive method for material damages (Zheng et al. 2000, Abeelee et al. 2000). In this case, the elastic constants of higher orders related to the inspected material can be determined and, therefore, used as a measure of the integrity of the material structure. In NDT applications, a defect with a contacting interface shows non-linear features when interacting with an intense acoustic wave, and behaves as a source of harmonics (Buck et al. 1978, Richardson 1979, Solodov 1994, Solodov 1998, Biwa et al. 2004, Biwa et al. 2006).

Even though, several studies have been conducted on (simulated) cracked specimens, imaging using harmonics is not yet mature enough for NDT applications. On the one hand, this is due to the complexity of the interaction mechanism between crack asperities in the field of high amplitude ultrasound and on the other hand, this is due to the difficulty of performing accurate non-linear measurements on real defects. Furthermore, the integration process of the acquisition system required for field measurements needs to focus on the development of ultrasonic probes, hardware and electronic components.

1.4 Fatigue of materials

When materials undergo cyclic loading, fatigue mechanisms become active, which can lead to crack initiation and crack growth and, therefore, possible failure of structural components (Ritchie 1999, Mughrabi 2002). To understand fatigue mechanisms and failure of metallic structures, extensive research and numerous experiments have been carried out over the last decades (Schijve 2001, Suresh 2003). As a result, a valuable database on fatigue has become available to engineers, to improve the design process and the durability of engineering components. As described by Schijve (2001), fatigue life of materials is mainly divided into two periods: crack initiation and crack growth. It is very essential to differentiate between the two stages, since several conditions, such as surface roughness, can affect the crack initiation and the crack growth in a different way.

1.4.1 Crack initiation and growth

Understanding crack initiation and crack growth in metals is very essential for the design life of structural components. For both crack stages, different prediction models have been developed over the last years, by practical experiments as well as by computer modeling (Schijve 2001, Suresh 2003). Prior to crack initiation, repetitive cyclic loading affects material grain boundaries and leads to dislocation movement of crystallographic planes along preferred slip lines (Figure 1.5). These lines form the so-called persistent slip bands (PSBs), along which crack growth takes place and where the plastic displacement is concentrated (Brown 2000).

1.4.2 Fracture modes and crack closure

In fracture mechanics, three basic modes are known (Suresh 2003, Fischer-Cripps 2007). Figure 1.6 schematically illustrates these modes with the corresponding crack surface displacement. Mode I represents the tensile opening, by which crack faces get separated normal to the crack plane, while modes II and III are the shear sliding modes in which crack faces are sheared in-plane and anti-plane, respectively. Depending on the fracture mode, crack asperities may make contact at certain regions along the crack length (Figure 1.7), leading to partial (or full) crack closure. However, a perfect crack closure is not expected, since the crack asperities do not entirely fit together of the opposing boundaries when even a compressive load is applied (Schijve 2001).

1.5 Limitations of the current inspection approach

Despite new technological developments in NDT, inspection of assets operating under severe conditions and undergoing a cyclic load, e.g., steel catenary risers (SCRs), is still challenging due to the nature of cracks that might start during the fatigue process of these assets. As a result of compressive stress surrounding cracked areas in a fatigued material, bridging between crack asperities may occur. Consequently, a crack of this type may become acoustically transparent, the so-called closed crack, and will act as a

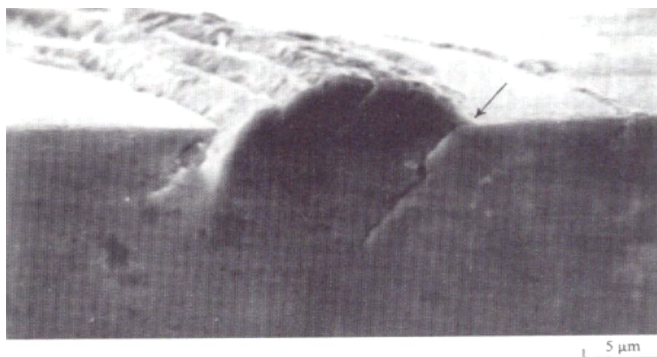


Figure 1.5: Example of crack initiation and PSB planes (Suresh 2003).

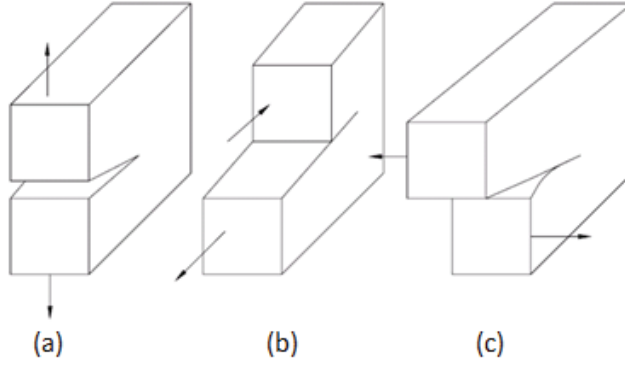


Figure 1.6: Basic modes known in fracture mechanics: Tensile opening or mode I (a), in-plane shear or mode II (b), and anti-plane shear or mode III (c) (Suresh 2003).

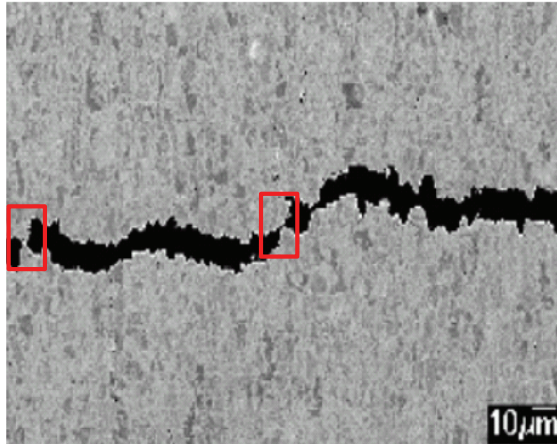


Figure 1.7: Partial crack closure where local contact between crack asperities is highlighted in red boxes (Suresh 2003).

transmitting layer for incident waves. Consequently, the inspection performance of the current NDT approach is negatively affected. To face this challenge, various NDT techniques can be applied, and the generated data can be combined giving more insight into crack response and behavior. Even though these techniques are combined, difficulties in terms of detection and sizing of such cracks still remain.

1.6 Thesis objective and outline

The main objective of this thesis is to explore and exploit the non-linear nature of acoustically transparent cracks, to improve detection and sizing accuracy of such cracks. For this purpose, appropriate measurements on stacked steel blocks and on a fatigue crack were carried out. Furthermore, a theoretical formulation is developed explaining the experimental findings in terms of crack closure, harmonic generation, and crack detection. All the results presented in this thesis are generated by compressional waves.

In Chapter 2, the principles of van der Waals interaction forces between atoms are recalled and then further extended to macroscopic objects. Based on this formulation, a stress-displacement formula describing the interaction between crack asperities is derived and the corresponding dynamic elasticity across the crack interface is formulated. To numerically model the wave propagation at a closed crack, an adaptive mass-spring lattice model, in which lumped masses are interconnected through vertical and diagonal springs, is developed. In this scheme, the elasticity of a cracked area as derived from the van der Waals formula is dynamically driven by the opening and closing of the crack. The effect of this dynamic elasticity occurs on the cell grid level containing the crack and can be detected by using a transmitter/receiver element on one side of the cracked cell unit and a transmitter element on the other side of the same cell unit. The relationship between crack opening and applied excitation amplitude is the key element for modeling crack closure and harmonic generation.

In Chapter 3, measurements of mechanical vibrations of a free surface caused by an ultrasonic probe are presented. The outcome of these measurements is used as an input for the source excitation in the mass-spring lattice scheme. Furthermore, numerical results on crack closure and harmonic generation at defined crack openings are presented. To investigate the crack response at various crack openings and excitation amplitudes, two crack shapes with different openings were modeled. The corresponding results are compared with the experimental results presented in Chapter 4.

In Chapter 4, we start with experiments on crack closure by pressing two steel blocks together in a load testing machine, simulating an artificial crack interface. In this setup, several ultrasonic probes were used to monitor reflection and transmission through the crack interface when applying a compressive load. Furthermore, harmonic measurements were conducted and the corresponding results are presented in terms of amplitude evolution of harmonics as a function of the applied load and excitation amplitudes. The next challenge was to extend our experiments to a real crack. To this end, a dedicated test specimen was loaded in the same testing machine and fatigued using the three-point bending method. Due to the complexity of the intended experiments, precautionary measures were taken regarding block design, crack initiation, probe housing, etc... Us-

ing a motor-driven mechanism, the crack was scanned, and different trace signals along the crack length were collected and Fourier transformed. Results on harmonic generation and their strength are given for various load values and excitation amplitudes. Finally, a comparison is made between theoretical formulation and experiments in terms of crack closure, harmonic generation, and detection.

In Chapter 5, we summarize all observations made in Chapters 2, 3, and 4. Furthermore, conclusions and recommendations for future work are given.

Chapter 2

Theoretical formulation

In this chapter, the basics of interaction between atoms and particles are recalled. The well-known van der Waals interaction forces are explained and the associated stress-displacement curve is given. Extending this approach to macroscopic objects, interaction between crack asperities will be derived. Using this formulation, crack closure and harmonic generation are numerically modeled by implementing a dynamic elasticity formula into a mass-spring lattice model.

2.1 Contact between solids

2.1.1 Introduction to atomic bonds

From a macroscopic point of view, materials may be represented as a continuum. Nevertheless, when zooming in on the material structure, solids consists of atoms which are stacked along well-defined atomic planes forming the basic building unit of crystallographic arrangements. These atoms are linked by atomic bonds, which determine the strength of solids. Commonly, as described by Maugis (1999), bonds between atoms are categorized as strong, or weak interactions. The ionic, covalent and metallic bonds belong to the first category, whereas the hydrogen bond and the van der Waals forces form the second category.

2.1.2 Van der Waals forces

Parsegian (2006) and Maugis (1999) extensively presented the van der Waals forces between neutral molecules, as a function of their separation distance r . These forces may arise from three types of dipole-dipole interactions, which were described in the Keesom theory (1921), the Debye theory (1920) and the London theory (1930). According to these theories, the potential energy between interacting dipoles is inversely dependent on their separation distance as $1/r^6$. Since this interaction energy tends towards infinity when r approaches zero, this term is balanced by adding a repulsive term, which can be explained by quantum mechanics (Griffiths 2004). Following this approach, atoms/molecules are attracted over long distances and repelled over short

distances. This interaction mechanism can be described by the Lennard-Jones potential using one of the most common empirical equations:

$$U(r) = 4U_0 \left[\left(\frac{a}{r} \right)^{12} - \left(\frac{a}{r} \right)^6 \right], \quad (2.1)$$

where U_0 is the minimum potential energy, a is the interatomic distance at which the potential energy is zero, and r is the separation distance between two atoms. Figure 2.1 graphically illustrates the potential energy given in Eq. 2.1, and the corresponding van der Waals interaction force ($-dU/dr$) between two atoms. In the absence of other forces (Fischer-Cripps 2000), atoms tend to reach the equilibrium position ($r = 1.12a$), at which the attractive term (power twelfth) and the repulsive term (power six) in Eq. 2.1 are equal. When applying an external force, and depending on the type of the atomic bond, the balance between these two terms will be affected. For instance, to slightly displace an atom near its equilibrium position, an increased pulling force is required (Figure 2.1b). By further pulling the atom away from the equilibrium position, the maximum force can be reached, which represents the strength of the atomic bond. To break the atomic bond, at least this maximum value is needed. Far from this maximum value, less and less force is required to keep the atom away from the initial position. Beyond a distance of $2.5a$, the van der Waals interaction dramatically decreases and tends to zero, which shows the short-range nature of these interaction forces between two atoms. To extend the van der Waals interaction to macroscopic objects, contributions of all atoms should be taken into account, which makes this interaction rather long-ranged. By integration of the van der Waals interaction force and assuming that the solid is

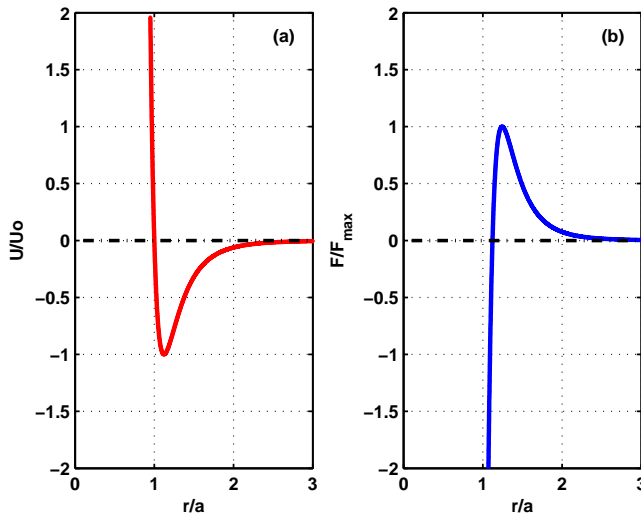


Figure 2.1: Lennard-Jones potential (a) and van der Waals force (b) between two atoms as a function of the interatomic distance r . Repulsive forces are short-ranged, while attractive forces are long-ranged.

a continuum, the van der Waals stress (force per unit area) between two half-spaces separated by a distance z can be obtained (Maugis 1999, Appendix B):

$$\sigma(z) = \frac{A}{6\pi z_0^3} \left[\left(\frac{z_0}{z} \right)^3 - \left(\frac{z_0}{z} \right)^9 \right], \quad (2.2)$$

where A is the Hamaker constant ($\approx 10^{-19}$ J for most metals), z_0 ($\approx 2 \cdot 10^{-10}$ m) is the equilibrium distance, and z is the separation distance between two half-spaces. Eq. 2.2 is graphically represented in Figure 2.2. Similarly to atom-atom interaction, the stress-displacement curve can be divided into two regions, repulsive and attractive. It can be observed that near the equilibrium position z_0 , the stress is nearly proportional to displacement. This corresponds to the elasticity of a solid for which Hooke's law applies and, therefore, the elasticity modulus E can be deduced. The second section of the stress-displacement curve ($z > z_m$), however, exhibits a non-linear behavior and corresponds to adhesion forces between the two half-spaces. It should be noticed that the slope in this region is less steep compared to the one observed in the atom-atom interaction (Figure 2.1b). This explains the long-ranged nature of interaction between large objects.

2.1.3 Contact models

Different models on contact between solids have been developed over a long period of time. The first theory on contact mechanics was developed by Hertz in 1882, who derived the radius of a contact between a sphere and an elastic half-space as a function of the load and elasticity of both interacting surfaces (Maugis 1999, Fischer-Cripps

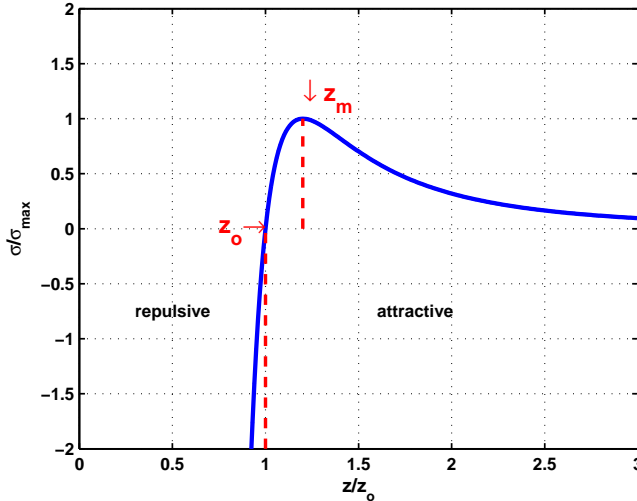


Figure 2.2: *van der Waals stress interaction between two half-spaces, z_0 and z_m represent the equilibrium and the maximum stress positions, respectively.*

2007). In his theory, the attractive forces of van der Waals as previously described, were neglected. In 1971, Johnson, Kendall and Roberts (JKR) developed a new theory based on the Hertzian contact, but accounting for the short-range interactions in the contact area, while neglecting the long-range interactions outside the contact area. In 1975, Derjaguin, Muller and Toporov (DMT) proposed a different theory, in which the van der Waals forces outside the contact area were considered, while the contact profile was assumed to be Hertzian. Following these theories, Maugis developed in 1992 a model, which bridges the JKR and DMT models as they are applicable for soft and hard solids and, therefore, describing the limits of the contact behavior between solids (Maugis 1991, Grierson et al. 2005).

2.2 Non-linear signature of a contacting interface

As previously mentioned, due to crack closure phenomenon, reliable detection and sizing of closed cracks, using conventional UT, is a challenge. More information on crack properties and a better probability of detection may be obtained by exploiting non-linear effects generated by the crack motion when interacting with ultrasonic waves. The key element in this approach is to excite the crack at one frequency with high ultrasonic amplitudes and extract harmonics that are possibly generated at the crack interface. It is expected that these generated harmonics are found in the reflected, as well as in the transmitted wave field.

Commonly, non-linear effects are associated with the distortion of the wave amplitude as it travels through the medium, resulting in the generation of harmonics. Such a behavior is a characteristic of material non-linearity, which deviates from the linear Hooke's law. For an ideal solid, this non-linear response is very low as the acoustic pressure acting on atoms is very small compared to the inter-atomic forces (Bruneau & Potel 2012). For imperfect solids, however, the non-linear response of the cracked area to an intense acoustical field is predominant, as the relative displacement of atoms in this weakly region is larger. Therefore, the corresponding stress-strain relationship shows an asymmetrical behavior, resulting in an asymmetrical stiffness across the crack interface. This is a characteristic of the so-called contact acoustic non-linearity (CAN), which may have different mechanisms allowing for the generation of harmonics at a contacting interface (Korshak et al. 2002, Solodov 2010).

First experimental studies on harmonic generation at a flat unbonded interface, when interacting with ultrasonic wave were performed by Buck et al. (1978). Related to this publication, Richardson (1979) theoretically formulated the equations describing this non-linear behavior. Further experimental investigations on contact boundaries were reported by Solodov (1994, 1998). The non-linear effects observed in these experiments were explained in Solodov (1998, 2010) and Solodov et al. (2002) as a result of the CAN phenomenon, in terms of asymmetrical stiffness across the interface and the Hertzian contact mechanism. A predictive approach using a spring contact model was used by Drinkwater et al. (1996), in which the stiffness variations of a partially contacting interface are predicted as a function of an applied pressure. Following Richardson's analysis, Biwa et al. (2004, 2006) and Kim et al. (2009) used a non-linear interface model, where the interfacial stiffness is given as a power function of the nominal contact pressure. As a

result, the non-linear parameters of the reflected and transmitted waves are derived from this interfacial stiffness. Inspired by atomic force microscopy (AFM) analysis, Yamanaka et al. (2004) introduced the Lennard-Jones potential to explain subharmonic generation at partially closed cracks. Recently, Yamanaka et al. (2011) proposed a two-dimensional dumped double node (DDN) model reproducing subharmonic generation and revealed some essential features observed in previous experiments conducted by Sasaki et al. (2005) and Ohara et al. (2006).

In the majority of the studies cited above and elsewhere, the non-linear response caused by the interaction of ultrasonic waves with a contacting interface, is predicted by various non-linear interface models and described as a change of a stiffness across the contacting interface. This is the starting point for the dynamic elasticity model proposed in this thesis. The model takes advantage from the fact that a defective crystallographic structure shows a change in elasticity when atomic bonds break and, therefore, leading to a weakly bonded interface. The elasticity of such an area is derived from the van der Waals stress-strain relationship between two half-spaces. A major advantage of this approach is that this elasticity is directly linked to material properties and can be dynamically updated as the opening between crack asperities changes.

2.3 Numerical modeling

Many different numerical approaches have been developed for modeling and analyzing wave propagation, including the finite element method (FEM), boundary element method (BEM), and finite difference method (FD). Commonly, the FD schemes are widely used in elastic wave analysis. In seismology, Virieux (1984, 1986) successfully implemented the two-dimensional FD staggered grid scheme to calculate stress and velocity at different nodes. The same numerical approach has been applied in the field of ultrasonics for modeling and improving ultrasonic techniques and procedures. Similar to FD, Harumi (1986) proposed the mass-spring lattice model (MSLM), in which lumped masses (inertia) are interconnected through springs (material elasticity). Based on Harumi's scheme, Yim & Choi (2000) developed a tool package for simulation and visualization of ultrasonic waves. Although the proposed MSLM method is comparable to the FD method in terms of discretization steps, it has, however, specific advantages compared to a typical FD scheme, especially when dealing with dynamic problems and handling material boundaries and free surfaces (Yim & Sohn 2000).

2.3.1 Mass-spring lattice model

From a physical perspective and referring to the advantages of using mass points and springs, the MSLM method is the most appropriate approach to be adopted here for the implementation of the dynamic elasticity model and for the analysis and illustration of crack closure behavior and harmonic generation.

The elastic wave equation governing the wave motion in a two-dimensional plane with a horizontal coordinate x and a vertical coordinate z pointing downward is given by (Virieux 1986, Harumi 1986):

$$\begin{aligned}\rho \frac{\partial^2 u}{\partial t^2} &= (\lambda + 2\mu) \frac{\partial^2 u}{\partial x^2} + (\lambda + \mu) \frac{\partial^2 v}{\partial x \partial z} + \mu \frac{\partial^2 u}{\partial z^2}, \\ \rho \frac{\partial^2 v}{\partial t^2} &= (\lambda + 2\mu) \frac{\partial^2 v}{\partial z^2} + (\lambda + \mu) \frac{\partial^2 u}{\partial x \partial z} + \mu \frac{\partial^2 v}{\partial x^2},\end{aligned}\quad (2.3)$$

where ρ is the mass density, λ and μ are Lamé constants, and u and v are particle displacements in x - and z -direction, respectively.

To discretize Eq. 2.3 in the x - z plane, the MSLM approach can be applied. In this model, the medium is assumed to be isotropic and can be represented by a lattice configuration containing linear and rotational springs connecting mass particles in a cell arrangement (Figure 2.3). For the sake of simplicity, only mass particles connected to the center mass located at point (i, j) are shown. According to this cell configuration and using the central FD approximation to first, second and mixed derivatives, displacements u and v at point (i, j) can be written in terms of relative displacements of the eight neighboring mass particles as (Yim & Sohn 2000):

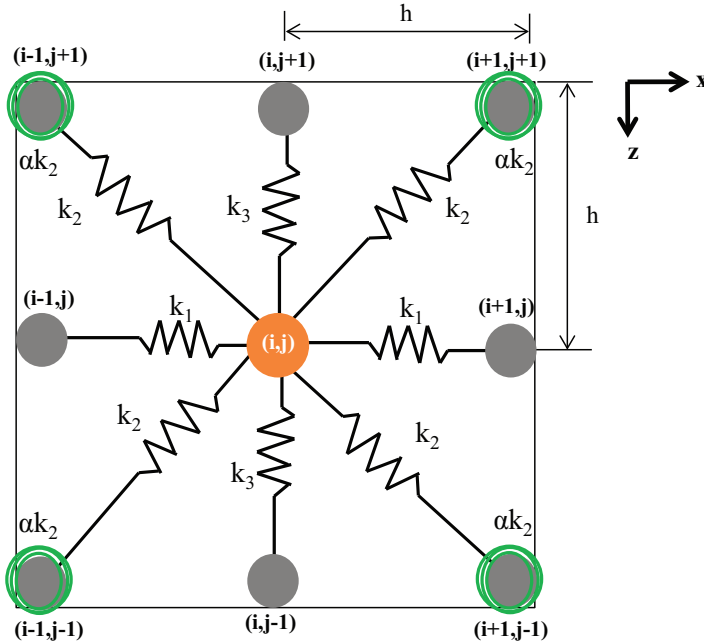


Figure 2.3: Schematic of a cell element representing the two-dimensional MSLM model: k_1, k_2, k_3 represent linear springs and αk_2 is a rotational spring connected to k_2 .

$$\begin{aligned}
\rho \frac{(u_{i,j}^{k+1} + u_{i,j}^{k-1} - 2u_{i,j}^k)}{(\Delta t)^2} &= k_1 \frac{(u_{i+1,j}^k + u_{i-1,j}^k - 2u_{i,j}^k)}{h^2} \\
&+ k_2 \frac{(u_{i+1,j+1}^k + u_{i+1,j-1}^k + u_{i-1,j+1}^k + u_{i-1,j-1}^k - 4u_{i,j}^k)}{2h^2} \\
&+ k_2 \beta \frac{(u_{i+1,j+1}^k + u_{i+1,j-1}^k + u_{i-1,j+1}^k + u_{i-1,j-1}^k - 4u_{i,j}^k)}{2h^2} \\
&+ k_2 \frac{(v_{i+1,j+1}^k - v_{i+1,j-1}^k - v_{i-1,j+1}^k + v_{i-1,j-1}^k)}{2h^2} \\
&+ k_2 \beta \frac{(v_{i+1,j+1}^k - v_{i+1,j-1}^k - v_{i-1,j+1}^k + v_{i-1,j-1}^k)}{2h^2},
\end{aligned} \tag{2.4}$$

$$\begin{aligned}
\rho \frac{(v_{i,j}^{k+1} + v_{i,j}^{k-1} - 2v_{i,j}^k)}{(\Delta t)^2} &= k_3 \frac{(v_{i+1,j}^k + v_{i-1,j}^k - 2v_{i,j}^k)}{h^2} \\
&+ k_2 \frac{(v_{i+1,j+1}^k + v_{i+1,j-1}^k + v_{i-1,j+1}^k + v_{i-1,j-1}^k - 4v_{i,j}^k)}{2h^2} \\
&+ k_2 \beta \frac{(v_{i+1,j+1}^k + v_{i+1,j-1}^k + v_{i-1,j+1}^k + v_{i-1,j-1}^k - 4v_{i,j}^k)}{2h^2} \\
&+ k_2 \frac{(u_{i+1,j+1}^k - u_{i+1,j-1}^k - u_{i-1,j+1}^k + u_{i-1,j-1}^k)}{2h^2} \\
&+ k_2 \beta \frac{(u_{i+1,j+1}^k - u_{i+1,j-1}^k - u_{i-1,j+1}^k + u_{i-1,j-1}^k)}{2h^2},
\end{aligned} \tag{2.5}$$

where h , Δt and ρ represent the grid spacing, time step and the mass density of the medium, respectively. $u_{i,j}^k$ and $v_{i,j}^k$ denote the mass particle displacements in the x - and z -directions at point (i, j) and time $k \Delta t$. Spring constants k_1 , k_2 , k_3 , β and α (Figure 2.3) represent the material elasticity and are related to Lamé constants by:

$$k_1 = k_3 = \lambda + \mu, \quad k_2 = \frac{\lambda + 3\mu}{4}, \quad \beta = \frac{\mu - \lambda}{\lambda + 3\mu}, \quad \alpha = 2h^2 \left(\frac{\mu - \lambda}{\lambda + 3\mu} \right). \tag{2.6}$$

In Eqs. (2.4) and (2.5), displacements at a later time $(k+1) \Delta t$ are computed explicitly from displacements at an earlier time $(k-1) \Delta t$ and $k \Delta t$. In this scheme, boundary conditions are solved using the boundary function formulated in Reynolds (1978). The stability condition of the proposed scheme is maintained by meeting the von Neumann requirement, in which the ratio $(\Delta t/h)$ should not exceed the critical value given by (Harumi 1986, Yim & Sohn 2000):

$$(\Delta t/h)_{critical} = \frac{1}{\sqrt{\frac{\lambda + 2\mu}{\rho}}}. \tag{2.7}$$

In all performed calculations, the ratio $(\Delta t/h)$ is approximately $8.33 \cdot 10^{-5} [sec/m]$, which is less than the critical value $1.68 \cdot 10^{-4} [sec/m]$ calculated from Eq. (2.7).

2.3.2 Implementation of van der Waals in an MSLM scheme

Although crack asperities are not parallel, the interaction model between two half-spaces, as outlined in Section 2.1.2, can be applied to approximate the interaction between two crack faces. As previously mentioned, the medium can be modeled using the MSLM scheme, in which the elasticity of each cell element is simply represented by spring constants k_1 , k_2 and k_3 . However, when introducing a closed crack into the grid model, the effective elasticity of the cell element containing the crack may change depending on the extension and contraction of this cell element and, hence, on the opening and closing state of the crack. Following this approach, and assuming that the crack opens and closes in the z -direction only (Figure 2.4), a dynamic elasticity of this element can be introduced and approximated by serially combining the material spring k_3 and the crack spring k_{crack} as:

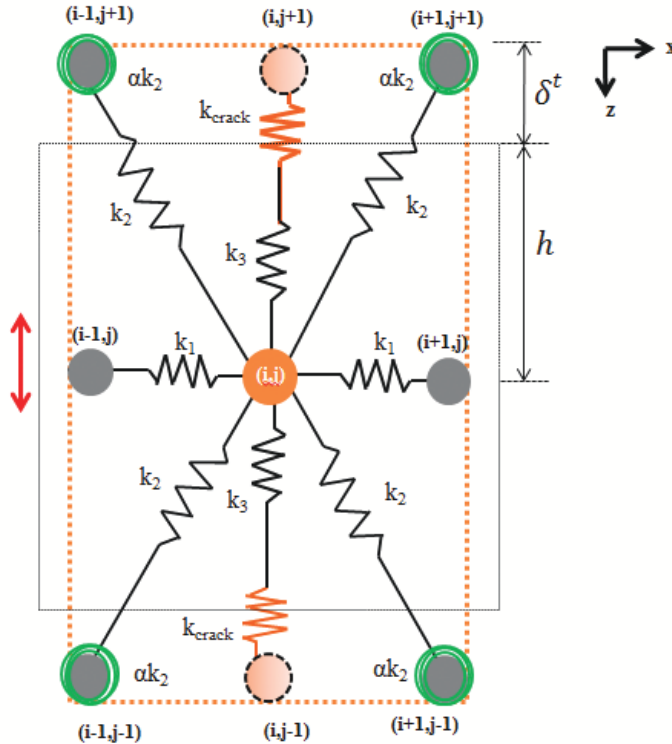


Figure 2.4: Adapted 2D-MSLM cell element, k_{crack} denotes the crack spring along the z -direction. Due to cracking of the cell element, mass particles are moved away from their equilibrium positions leading to the extension of this element. δ^t denotes the crack opening displacement at time t .

$$k_{dynamic} = \left(\frac{1}{k_3} + \frac{1}{k_{crack}} \right)^{-1}. \quad (2.8)$$

Using Eq. (2.2) for the interaction stress between crack asperities, the related elasticity of the crack spring k_{crack} can be derived. Since the repulsive term (power nine) in the van der Waals interaction model is inherent in the MSLM model, the elasticity of the crack spring can be derived from Eq. (2.2) by dividing the attractive stress term ($A/6\pi\delta^3$) in the van der Waals equation by the strain factor (δ/h) induced by a dynamic crack opening displacement δ :

$$k_{crack}(\delta) = \left(\frac{Ah}{6\pi\delta^4} \right), \quad (2.9)$$

where δ at time t denoted by δ^t can be computed from the initial crack opening δ_0 , crack opening displacement δ^{t-1} at time $t-1$, and crack spring elasticity k_{crack}^{t-1} at time $t-1$ as:

$$\delta^t = \delta_0 + \left(\frac{k_3}{k_3 + k_{crack}^{t-1}} \right) \cdot \delta^{t-1}. \quad (2.10)$$

According to Eq. (2.9), the crack elasticity is highly non-linear and inversely proportional to the dynamic crack opening displacement as $1/\delta^4$, for which a typical dynamic characteristic is illustrated in Figure 2.5. In a closed state, mass particles are relatively close to each other and, hence, the crack acts as a stiff spring, while in an open state, the crack elasticity drops and it acts, therefore, as a weak spring. Consequently, variations in the effective spring stiffness of the cracked cell element lead to a non-linear behavior of the dynamic elasticity when a force is acting on the medium.

By substitution of Eq. (2.9) into Eq. (2.8) for the dynamic elasticity of the cracked cell element, we obtain:

$$k_{dynamic} = \left(\frac{1}{k_3} + \frac{6\pi\delta^4}{Ah} \right)^{-1}. \quad (2.11)$$

After replacing k_3 by the expression for $k_{dynamic}$ in the discretized version of the vertical displacement (Eq. 2.5), the response of the cracked cell element in reflection and transmission modes can be calculated as the crack opening changes. For small values of δ , the cracked cell element will behave as a transmitting layer, while at a larger δ value it will reflect strongly, because the mismatch between crack and medium stiffness is considerable. By adopting this approach, the response of a closed crack is directly seen on a grid cell level, which leads to an efficient modeling when small crack openings are used.

The steps required for updating the dynamic elasticity of the cracked cell element are schematically shown in Figure 2.6. In this iterative scheme, the initial cell opening displacement δ^{t_0} is computed from the vertical displacements at grid levels (j) and ($j-1$) of the cracked cell element at time $t = t_0$ as:

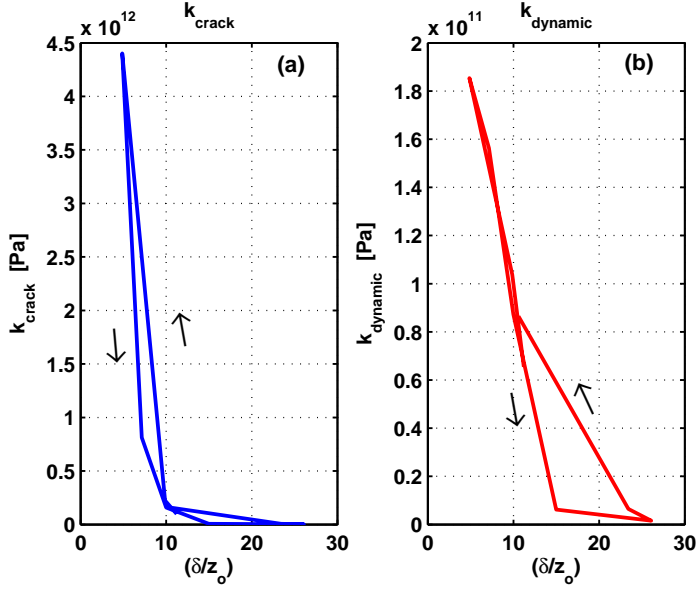


Figure 2.5: Example of a dynamic characteristic of the crack spring k_{crack} (a), and the resulting $k_{dynamic}$ (b) as a function of a dynamic crack opening δ . A hysteresis behavior can be seen as the crack area opens and closes dynamically.

$$\delta^{t_0} = (v_{j,i}^{t_0} - v_{j-1,i}^{t_0}). \quad (2.12)$$

By inserting Eq. (2.12) into Eq. (2.9), the initial crack spring elasticity $k_{crack}^{t_0}$ can be deduced, from which, the dynamic cell opening displacement δ^{t_1} at time t_1 can be computed as:

$$\delta^{t_1} = \delta_0 + \left(\frac{k_3}{k_3 + k_{crack}^{t_0}} \right) \cdot (v_{j,i}^{t_0} - v_{j-1,i}^{t_0}). \quad (2.13)$$

To update the crack spring elasticity $k_{crack}^{t_1}$ at time t_1 , the value of δ^{t_1} computed from Eq. (2.13) is inserted again into Eq. (2.9), and the resulted value is subsequently injected into Eq. (2.11), leading to a dynamic update of the cracked cell elasticity. For the next time steps, the same procedure is followed and the process is iterated as long as the extension and contraction of the cracked cell element occur.

The major advantage of this adaptive scheme is the simplicity of computing the dynamic elasticity according to Eq. (2.9), without considering additional parameters describing the cracked cell element. All parameters involved in this equation are related to material properties, except δ , which represents the crack opening displacement in terms of the extension and contraction of the cracked cell element. Furthermore, the way by which the

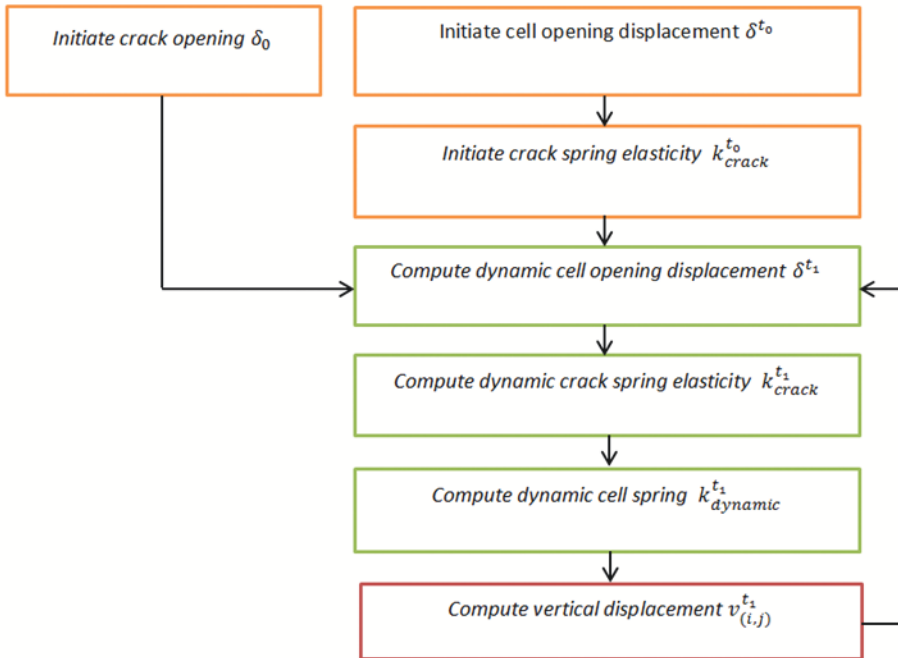


Figure 2.6: Updating procedure of the dynamic elasticity $k_{dynamic}$ showing the first iteration scheme.

crack is represented in a cell element allows for using the same discretization parameters (grid spacing and time) as outside the cracked cell element. From a computational point of view, this approach is very advantageous and less expensive for this application.

Chapter 3

Numerical results

In this chapter, measurements of mechanical vibrations of a free surface caused by a 4 MHz compressional wave probe are presented. The outcome of these measurements is used as an input for the source excitation in the mass-spring lattice scheme. Furthermore, numerical results on crack closure and harmonic generation at defined crack openings are presented. To investigate the crack response at various crack openings and excitation amplitudes, two crack shapes with different openings were modeled.

3.1 Material displacement

As outlined in Section 2.3.1, displacements in the medium are computed using the discretized version of the wave equation. By means of the MSLM scheme, the magnitudes of these displacements are derived from the amplitude of the excitation source. Prior to modeling, measurements of mechanical vibrations in terms of material displacement were performed in order to use realistic values of the excitation amplitude in the MSLM scheme. For this purpose, a steel block was excited by a 4 MHz compressional wave probe on one side, whereas the resulting displacement was measured on the other side using a laser vibrometer (Figure 3.1). In this setup, various excitation voltages were applied, while material displacements at a distance of 100 mm from the probe surface were measured. For instance, at 200 Vpp and 1200 Vpp peak-to-peak voltage, material displacements of approximately 6 nm and 40 nm were recorded at the ROI region, respectively.

3.2 Crack transparency and harmonic generation

To simulate acoustical crack transparency, the MSLM scheme with the van der Waals formulation incorporated, as explained in Section 2.3.2 has been applied, by changing the excitation amplitude in relation to the initial value of the crack opening. In these simulations, all excitation amplitudes, noted as a_z , and initial crack openings, noted as δ_0 , are given as a function of the equilibrium distance z_0 . As previously explained, the dynamic elasticity of the spring within the cracked cell element is updated as a function

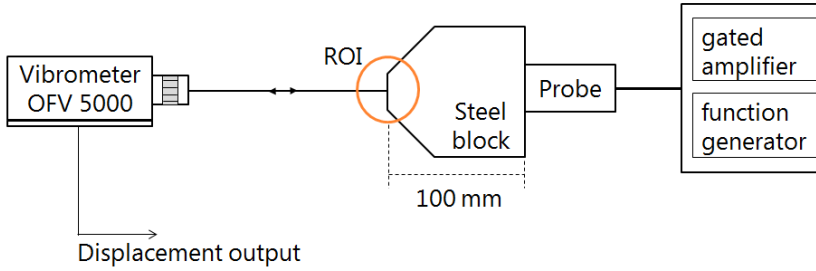


Figure 3.1: Schematic diagram of material displacement measurements including the laser vibrometer OFV-5000. The circled area represents the region of interest (ROI), at which material displacements were measured by exciting the steel block with a 4 MHz compressional probe. The right part of this setup, excluding laser vibrometer, will be a part of the intended experimental setup for crack closure and harmonics detection.

of the crack opening displacement δ . Depending on the extension and contraction of the cracked cell element, the value of the dynamic elasticity changes and, hence, a mismatch between the medium stiffness (k_3) and the dynamic stiffness of the cracked area ($k_{dynamic}$) occurs. The response of the cracked area in terms of reflection and transmission is caused by this stiffness mismatch. To demonstrate this phenomenon, Figure 3.2 illustrates the response of a cracked cell element at four excitation amplitudes of $5z_0$ to $20z_0$, in steps of $5z_0$, for an initial crack opening of $5z_0$. It is clear that the crack transparency is more observed for excitation amplitudes $5z_0$ and $10z_0$, for which the incident wave is almost transmitted through the cracked cell element. However, by increasing the input amplitude to $15z_0$ and $20z_0$, at a fixed initial crack opening, the crack partially opens, which leads to reflection of ultrasonic waves. This suggests the possibility to detect partially closed cracks in reflection mode by using an appropriate ratio between the input amplitude and the crack opening.

To assess the non-linear nature of reflected and transmitted waveforms resulting from the extension and contraction of a cracked cell element, reference simulations from a region free of cracks were required. To this end, multiple scan shots were performed starting from an uncracked cell element towards a cracked cell element. This was achieved by moving the source-receiver arrangement in steps of 1 mm along the x-direction as illustrated in Figure 3.3. In this configuration, the cracked cell element is situated between a transmitter/receiver probe (labeled T/R) intended for excitation and receiving reflected waves, and a receiver probe (labeled R) for collecting transmitted waves. In this setup, the source excitation is modeled as a local material displacement with an excitation amplitude of $a_z = 20z_0$ generating a sinusoidal wave of 10 cycles with a fundamental frequency of 4 MHz for a crack opening $\delta_0 = 5z_0$.

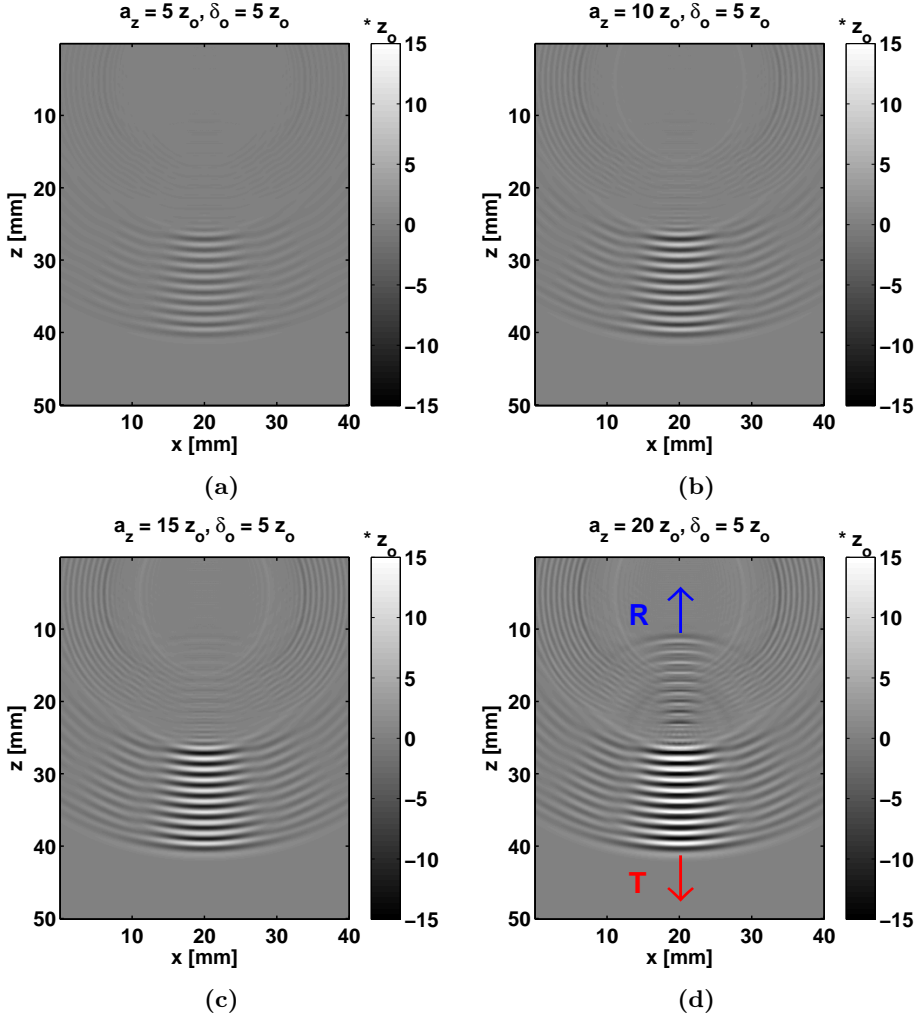


Figure 3.2: Simulated responses of a partially closed crack given as a function of vertical displacement v at various excitation amplitudes, $a_z = 5 z_o$ (a), $a_z = 10 z_o$ (b), $a_z = 15 z_o$ (c) and $a_z = 20 z_o$ (d) for a fixed initial crack opening $\delta_o = 5 z_o$. Labels R and T stand for reflection and transmission, respectively.

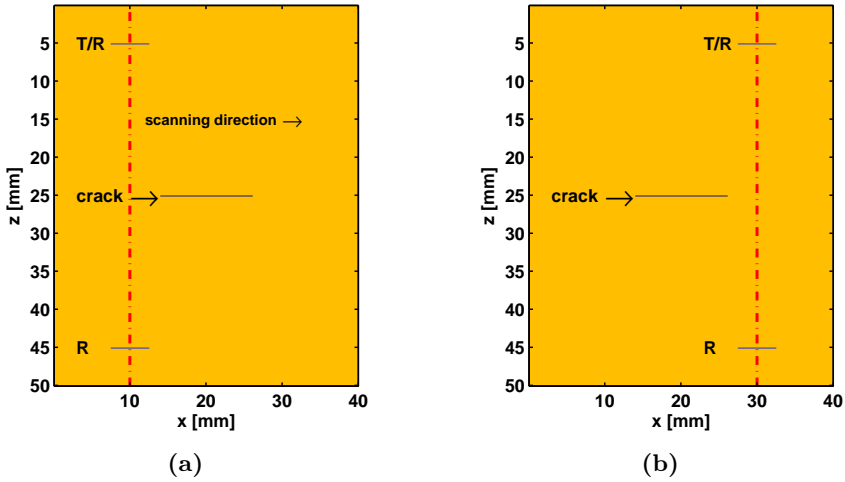


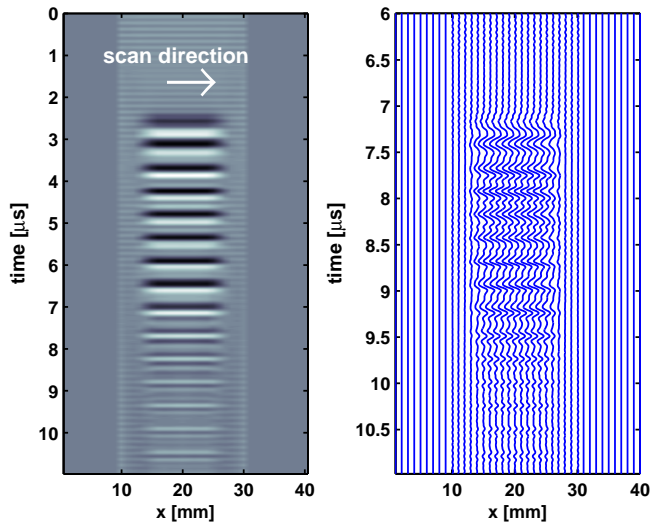
Figure 3.3: Simulation setup for scanning towards and along the cracked cell element centered at $x = 20$ mm along the x -direction. Scan starts at $x = 10$ mm (a) and ends at $x = 30$ mm (b). T/R represents the excitation source (probe) that transmits and receives signals, while R represents the receiving probe. The two probes are moved towards the crack area simultaneously with a step of 1 mm. Red dotted lines at $x = 10$ mm and $x = 30$ mm represent the scanning region in which reflected and transmitted data is collected.

To compare between traces in regions with and without a crack, the recorded signals in reflection and transmission modes were stacked together and displayed in the B-scan representation as shown in Figures 3.4a and 3.4b, respectively. In these figures, traces collected at the uncracked region (between 10 mm - 13 mm and 27 mm - 30 mm) are considered as reference traces. In the case of reflection, it can be observed that the waveform of various traces exhibit an amplitude distortion of the signal amplitude, while in the case of transmission data it is less visible. This may suggest the presence of non-linear components in these signal traces. In order to investigate the presence of harmonics, all signal traces, for both reflection and transmission modes, were Fourier transformed and are shown in Figures 3.5 and 3.6. Clearly, in both modes the fundamental frequency as well as its higher harmonics (second and third) are present.

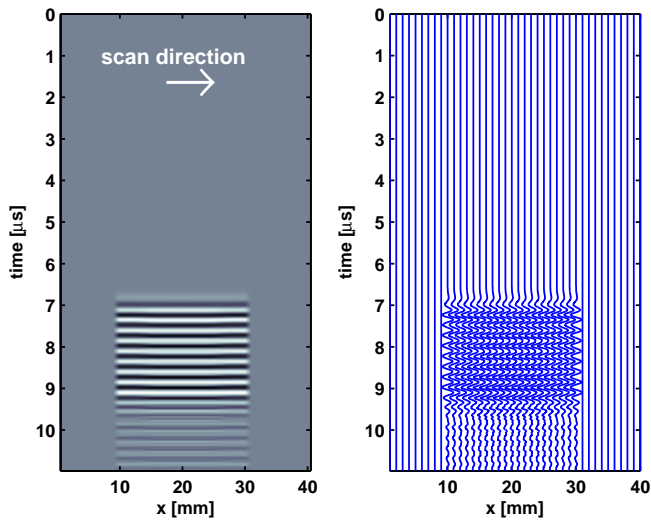
Looking at the amplitude ratio (A_2/A_1) between the second harmonic and the fundamental frequency, differences can be seen when comparing the two modes. In the case of reflection, this ratio yields 3 dB only, whereas in the transmission mode, it reaches 18 dB. For this specific crack opening and input amplitude, the second harmonic is more pronounced in the reflection mode than in the transmission mode. To investigate harmonic generation at different crack openings, the excitation amplitude was fixed at $20 z_0$, while the initial crack opening was set at $5 z_0$, $10 z_0$ and $15 z_0$. Figures 3.7 to 3.10 show the frequency content corresponding to the reflected and transmitted waves for these crack openings. As expected, by changing the crack opening, reflection and transmission of ultrasonic waves are affected. For instance, second harmonic generation almost

vanishes at crack opening $15z_0$. In this case, the crack face driven by the excitation amplitude is weakly pushed towards the repulsive region as previously illustrated in the stress-displacement curve (towards z_m , Figure 2.2), which results in a weakly non-linear vibration of the crack interface. However, by increasing the excitation amplitude, e.g., up to $30z_0$, the crack opening displacement will decrease leading to a strong vibration of the crack interface and δ , therefore, allowing for the recovery of harmonics.

To quantify and compare harmonic generation at these crack openings, magnitudes of the fundamental and second harmonic in both modes were extracted and plotted in Figure 3.11. Clearly, it can be seen that by extending the crack opening in the case of reflection, the magnitude of the fundamental frequency increases, whereas the amplitude of the second harmonic decreases dramatically. In the case of transmission, however, a slight change in both magnitudes can be observed. This observation confirms that second harmonic generation and its strength strongly depends on the ratio between crack opening and excitation amplitude.



(a)



(b)

Figure 3.4: Simulated reflected (a) and transmitted (b) data collected between positions $x = 10$ mm and $x = 30$ mm at excitation amplitude $a_z = 20 z_0$ with 10 cycles for an initial crack opening $\delta_0 = 5 z_0$, displayed in B-scan representation.

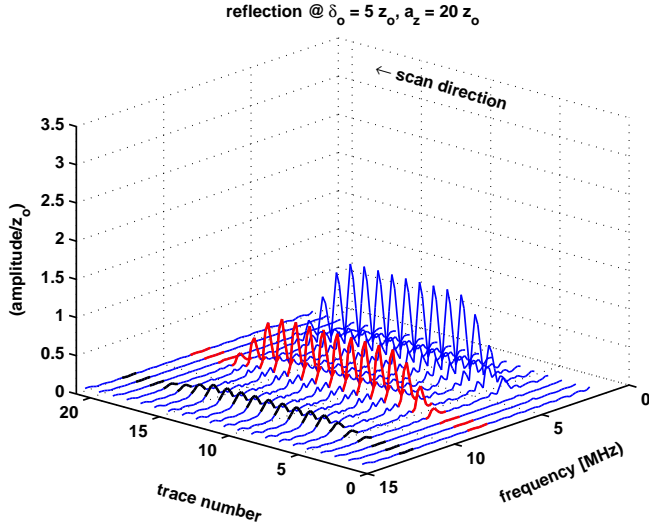


Figure 3.5: Frequency spectra related to reflected waveforms collected between positions $x = 10$ mm and $x = 30$ mm at excitation amplitude $a_z = 20 z_0$ with 10 cycles for an initial crack opening $\delta_0 = 5 z_0$.

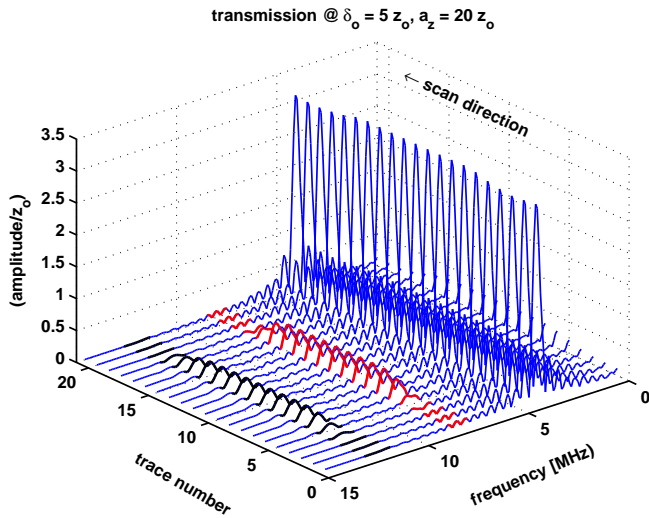


Figure 3.6: Frequency spectra related to transmitted waveforms collected between positions $x = 10$ mm and $x = 30$ mm at excitation amplitude $a_z = 20 z_0$ with 10 cycles for an initial crack opening $\delta_0 = 5 z_0$.

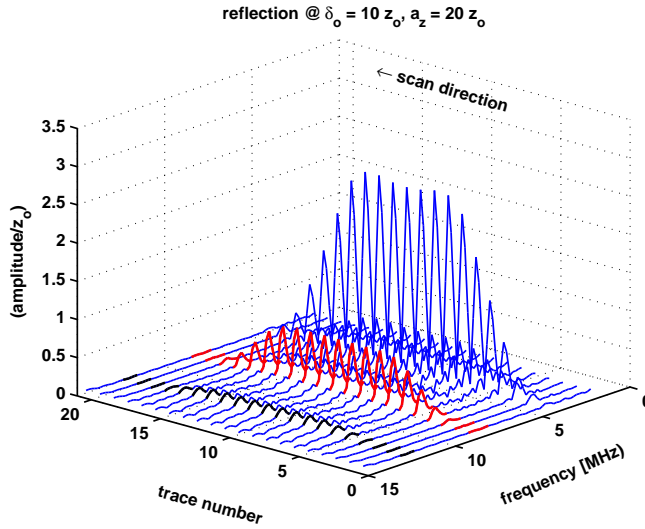


Figure 3.7: Frequency spectra related to reflected waveforms collected between positions $x = 10$ mm and $x = 30$ mm at excitation amplitude $a_z = 20 z_0$ with 10 cycles for an initial crack opening $\delta_0 = 10 z_0$.

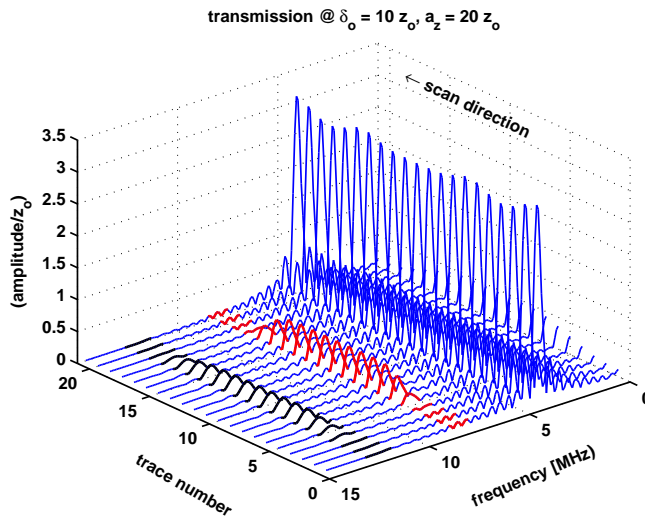


Figure 3.8: Frequency spectra related to transmitted waveforms collected between positions $x = 10$ mm and $x = 30$ mm at excitation amplitude $a_z = 20 z_0$ with 10 cycles for an initial crack opening $\delta_0 = 10 z_0$.

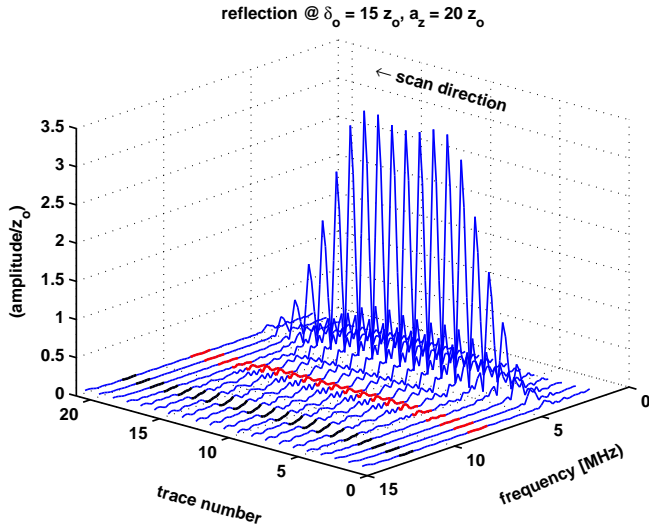


Figure 3.9: Frequency spectra related to reflected waveforms collected between positions $x = 10$ mm and $x = 30$ mm at excitation amplitude $a_z = 20 z_0$ with 10 cycles for an initial crack opening $\delta_0 = 15 z_0$.

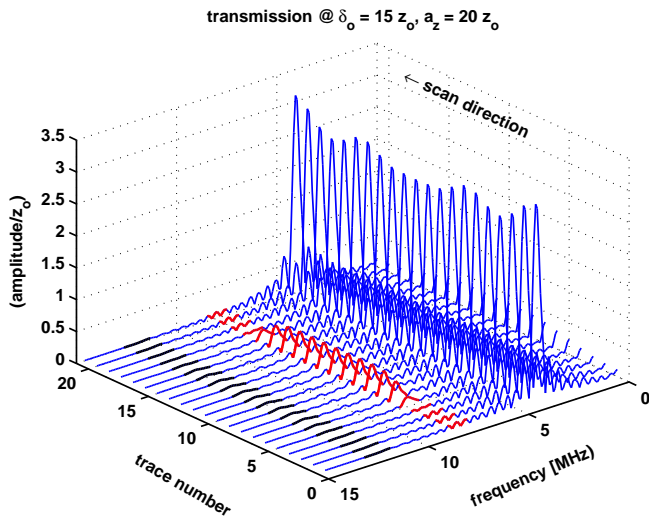


Figure 3.10: Frequency spectra related to transmitted waveforms collected between positions $x = 10$ mm and $x = 30$ mm at excitation amplitude $a_z = 20 z_0$ with 10 cycles for an initial crack opening $\delta_0 = 15 z_0$.

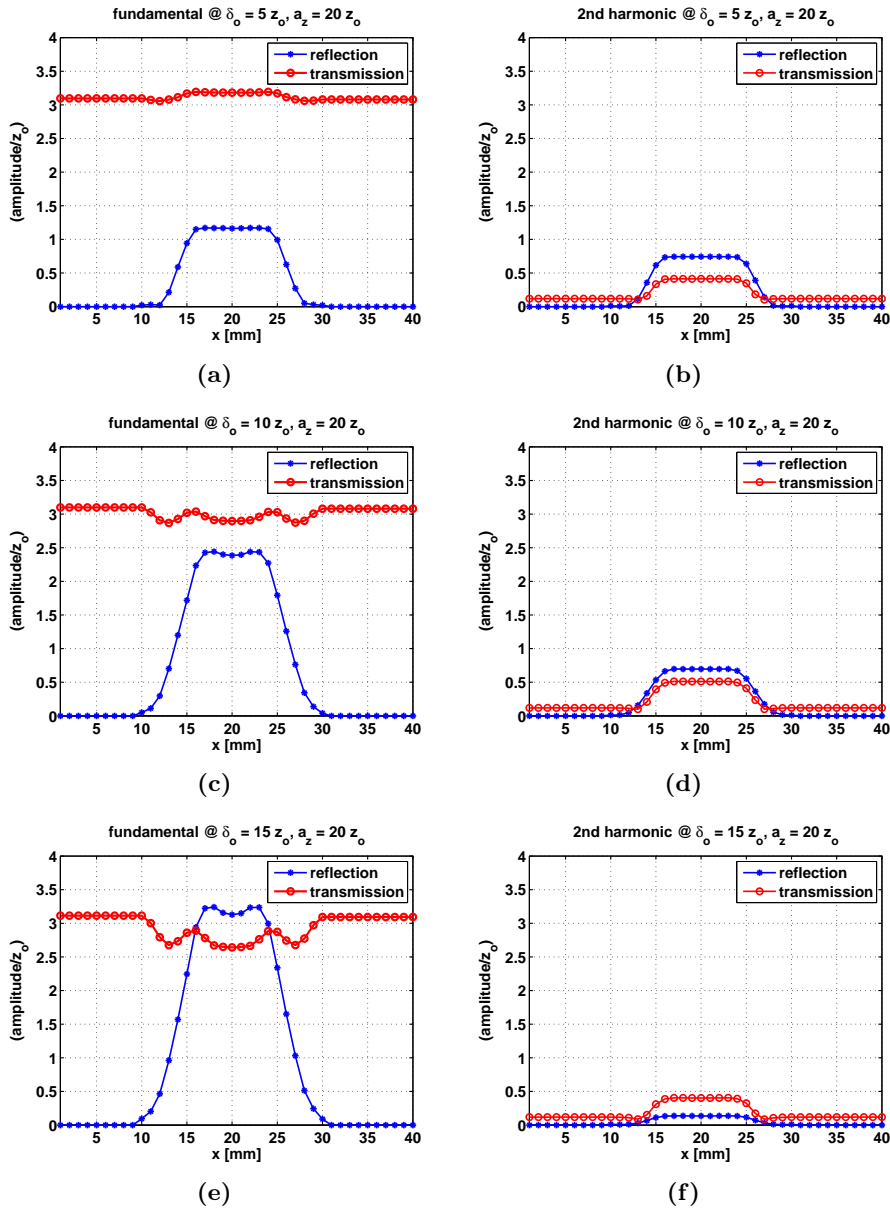


Figure 3.11: Magnitudes of the fundamental (a,c,e) and second harmonic (b,d,f) in reflection and transmission modes of different traces at a fixed excitation amplitude $a_z = 20 z_0$ and different crack openings $\delta_0 = 5 z_0$ (a,b), $\delta_0 = 10 z_0$ (c,d) and $\delta_0 = 15 z_0$ (e,f).

To extend our investigation on harmonic generation as a function of input amplitude in relation to a given irregular crack opening shape, we consider a partially closed crack of 16 mm in length consisting of equal segments with successive openings $10 z_0$, $5 z_0$, $15 z_0$ starting at position $x = 12$ mm and ending at position $x = 28$ mm using the same grid size and model of Figure 3.3. For these crack openings, the corresponding center-lines are located at positions 15 mm, 20 mm and 25 mm along the x-direction, respectively. The simulated crack was insonified at different excitation amplitudes, from $5 z_0$ to $20 z_0$ in steps of $5 z_0$, by using the same scanning procedure as explained in the preceding section.

Following the same way of data presentation and analysis, signal traces at different positions along the x-direction were collected and Fourier transformed. Figures 3.12 to 3.19 show the frequency content of reflected and transmitted waves at input amplitudes $5 z_0$, $10 z_0$, $15 z_0$ and $20 z_0$, respectively. It can be seen that the crack is partially transmitting for all applied excitation amplitudes. Furthermore, it can be confirmed that the second harmonic generations depends on the crack opening, i.e., contact area between crack asperities, in combination with the applied excitation amplitude.

To further illustrate the existence of non-linearity resulting from crack interface motion at different excitation amplitudes, magnitude information related to the fundamental and second harmonic was extracted from the spectral data and plotted in Figure 3.20 for both reflection and transmission modes. For instance, at excitation amplitude $5 z_0$, the magnitude of the reflected fundamental at position 20 mm is almost zero (Figure 3.20a). This suggests that at this position, the simulated crack is fully transparent for incident waves, whereas at positions 15 mm and 25 mm, the crack still reflects some energy back to the source-receiver element. At the same excitation amplitude and crack shape, interaction of crack faces did not result in second harmonic generation (Figure 3.20b). By increasing the excitation amplitude from $5 z_0$ to $15 z_0$, the magnitude of the reflected fundamental at positions 15 mm and 25 mm increases by approximately 11 dB and 10 dB, respectively (Figure 3.20e). Meanwhile, at this specific excitation amplitude and crack opening, the second harmonic is generated in both reflection and transmission modes (Figure 3.20f). In the case of reflection, the second harmonic is only recorded at crack position 15 mm, while for the transmitted case, two maximum points are visible at 15 mm and 25 mm. By further increasing the input amplitude, the reflected and transmitted fundamentals rise further (Figures 3.20e and 3.20g).

Looking at Figures 3.20f and 3.20h, the magnitude of the second harmonic for both modes increases. Interestingly, at excitation amplitude $20 z_0$, the simulated crack exhibits a strong second harmonic generation at crack position 20 mm in reflection mode. Exactly at this position, which corresponds to crack segment $5 z_0$, the reflected fundamental curve (Figure 3.20g) shows a minimum. In contrast, at crack position 25 mm (crack segment $15 z_0$), the reflected second harmonic curve shows a minimum, while the reflected fundamental curve exhibits a maximum. Consequently, by combining the fundamental and second harmonic information, it is clear that both curves are complementing each others. This redundancy of information allows for a better screening of crack transparency and leads to a significant improvement of the detection of partially closed cracks .

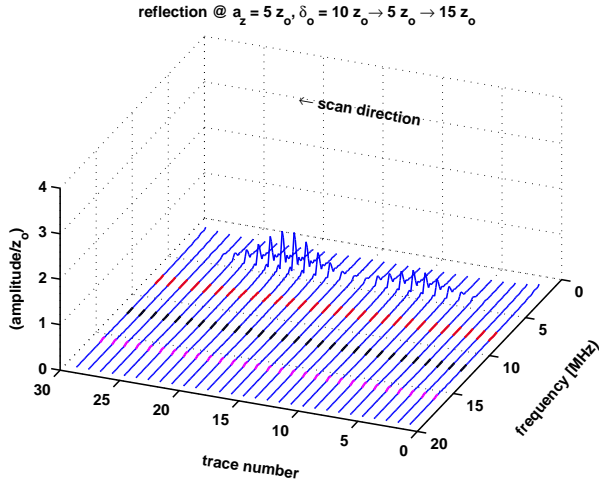


Figure 3.12: Frequency spectra related to reflected waveforms collected between positions $x = 6$ mm and $x = 34$ mm at excitation amplitude $a_z = 5 z_0$ with 10 cycles for a partially closed crack with successive openings $\delta_0 = 10 z_0, \delta_0 = 5 z_0, \delta_0 = 15 z_0$.

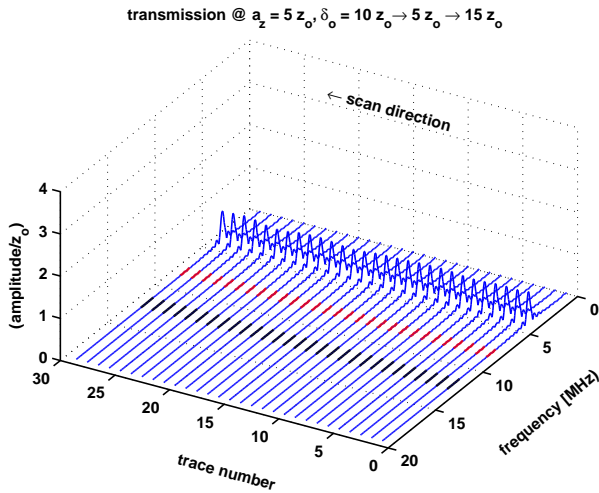


Figure 3.13: Frequency spectra related to transmitted waveforms collected between positions $x = 6$ mm and $x = 34$ mm at excitation amplitude $a_z = 5 z_0$ with 10 cycles for a partially closed crack with successive openings $\delta_0 = 10 z_0, \delta_0 = 5 z_0, \delta_0 = 15 z_0$.

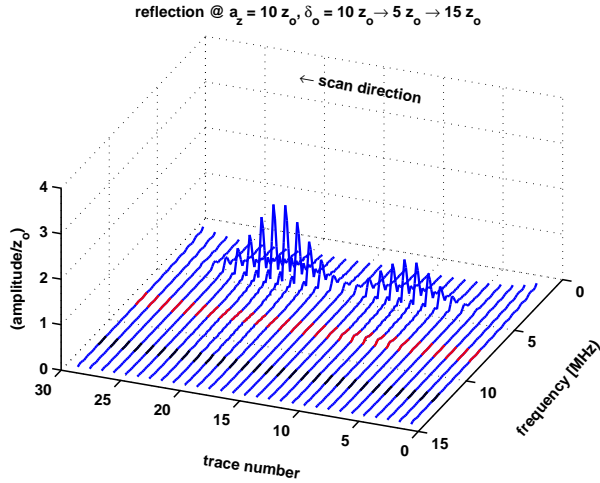


Figure 3.14: Frequency spectra related to reflected waveforms collected between positions $x = 6$ mm and $x = 34$ mm at excitation amplitude $a_z = 10 z_0$ with 10 cycles for a partially closed crack with successive openings $\delta_0 = 10 z_0, \delta_0 = 5 z_0, \delta_0 = 15 z_0$.

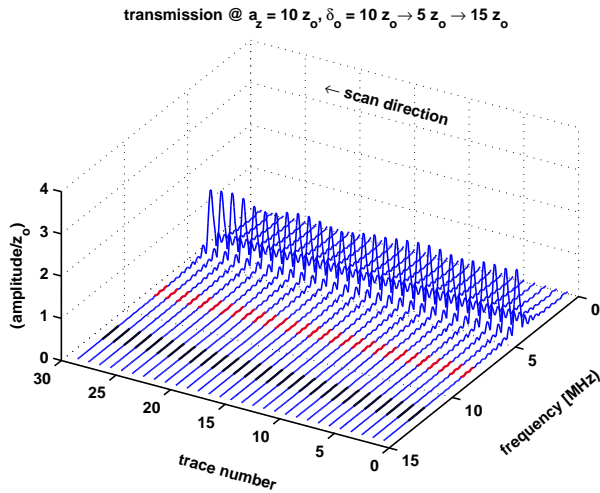


Figure 3.15: Frequency spectra related to transmitted waveforms collected between positions $x = 6$ mm and $x = 34$ mm at excitation amplitude $a_z = 10 z_0$ with 10 cycles for a partially closed crack with successive openings $\delta_0 = 10 z_0, \delta_0 = 5 z_0, \delta_0 = 15 z_0$.

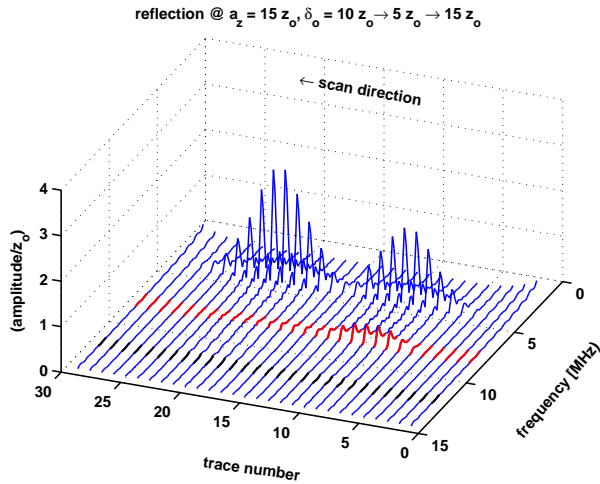


Figure 3.16: Frequency spectra related to reflected waveforms collected between positions $x = 6$ mm and $x = 34$ mm at excitation amplitude $a_z = 15 z_0$ with 10 cycles for a partially closed crack with successive openings $\delta_0 = 10 z_0, \delta_0 = 5 z_0, \delta_0 = 15 z_0$.

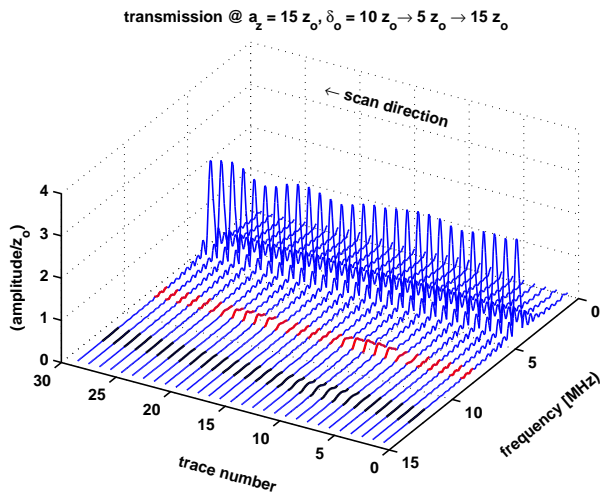


Figure 3.17: Frequency spectra related to transmitted waveforms collected between positions $x = 6$ mm and $x = 34$ mm at excitation amplitude $a_z = 15 z_0$ with 10 cycles for a partially closed crack with successive openings $\delta_0 = 10 z_0, \delta_0 = 5 z_0, \delta_0 = 15 z_0$.

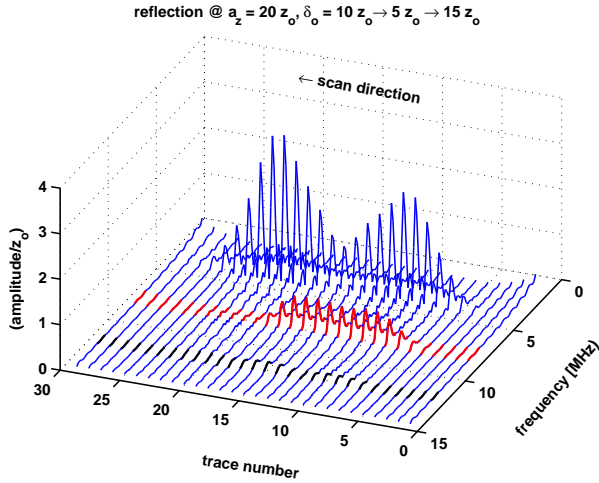


Figure 3.18: Frequency spectra related to reflected waveforms collected between positions $x = 6$ mm and $x = 34$ mm at excitation amplitude $a_z = 20 z_0$ with 10 cycles for a partially closed crack with successive openings $\delta_0 = 10 z_0, \delta_0 = 5 z_0, \delta_0 = 15 z_0$.

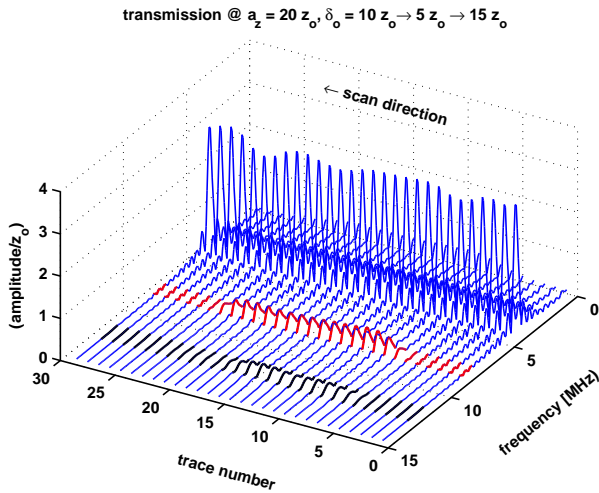


Figure 3.19: Frequency spectra related to transmitted waveforms collected between positions $x = 6$ mm and $x = 34$ mm at excitation amplitude $a_z = 20 z_0$ with 10 cycles for a partially closed crack with successive openings $\delta_0 = 10 z_0, \delta_0 = 5 z_0, \delta_0 = 15 z_0$.

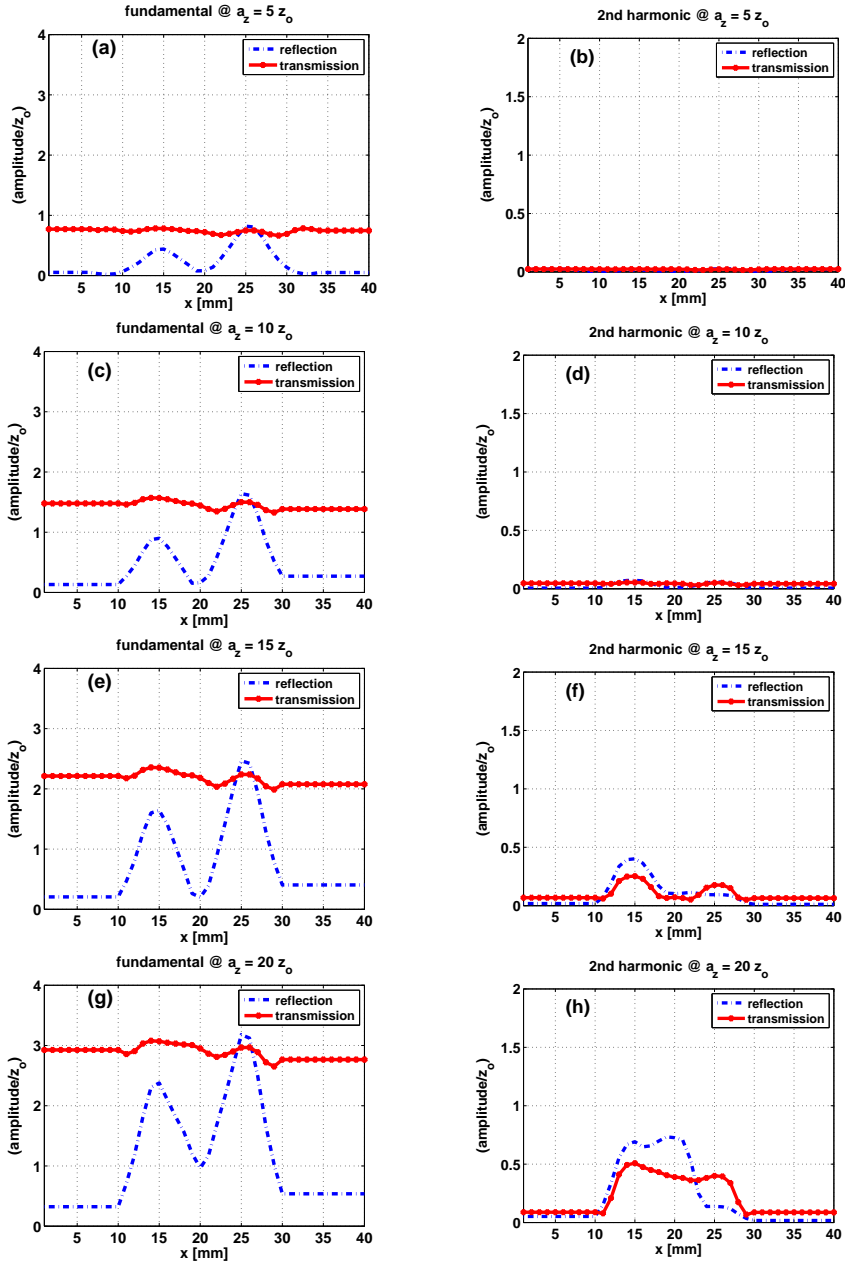


Figure 3.20: Magnitudes of the fundamental (a,c,e,g) and second harmonic (b,d,f,h) in reflection and transmission modes for a partially closed crack with successive openings $\delta_0 = 10 z_0$, $\delta_0 = 5 z_0$, $\delta_0 = 15 z_0$ at excitation amplitudes $a_z = 5 z_0$, $a_z = 10 z_0$, $a_z = 15 z_0$ and $a_z = 20 z_0$.

Chapter 4

Experiments

Crack closure, harmonic generation and detection are the key elements in this chapter. First, crack closure will be demonstrated by applying a load on two steel blocks simulating an artificial crack interface, and on a fatigued block containing a real crack. Secondly, harmonic generation and detection on both crack interfaces will be illustrated by using a dedicated setup consisting mainly of an arbitrary function generator, amplifier and specially designed dual frequency probes. Finally, the results are presented, and a comparison between theoretical formulation and experiments is made.

4.1 Artificial crack interface

4.1.1 Experimental setup

The experimental setup used to investigate the acoustical transparency of an artificial interface is shown in Figure 4.1a. In this setup, four steel blocks are stacked on top of each other, where the top and bottom blocks labeled as 1 and 4, were designed for the probe housing, whereas the artificial interface was simulated by a contact area of 50 x 50 mm between blocks labeled as 2 and 3. To avoid possible plastic deformation of this contact area at high compressive load values, the steel blocks were polished at the contacting planes allowing for a smooth contact interface. Prior to the measurements, the condition of the contact interface in terms of surface deformation was examined as a function of several loading and unloading cycles. To monitor acoustical transparency of the artificial interface, when applying a compressive load, a multi-channel acquisition system was used with eight ultrasonic channels for recording signals reflected back, and transmitted through, the artificial interface as illustrated in Figure 4.1b.

4.1.2 Interface closure

To investigate reflection and transmission of ultrasonic waves at the artificial interface, when applying a compressive load, compressional wave probes labeled $C1$ and $C2$ and shear wave probes labeled $S1$, $S2$, $S3$ and $S4$ were used (Table 4.1). The complete setup was loaded under an electro-hydraulic testing machine with a maximum force of

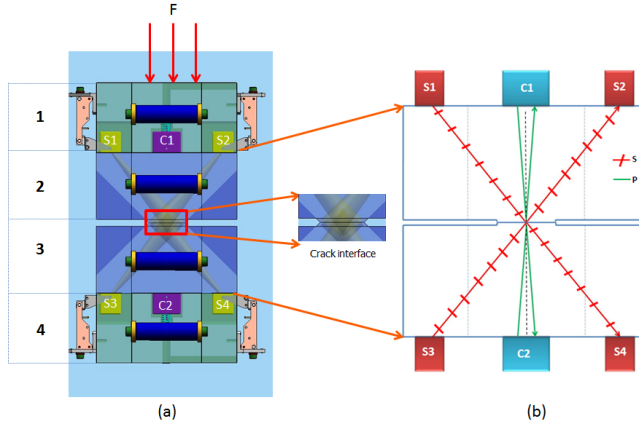


Figure 4.1: Schematic representation of stacked blocks including ultrasonic probes (a) and ultrasonic channels required for monitoring crack acoustical transparency as a function of the loading force (b). Compressional and shear wave probes are labeled as C and S, respectively. P stands for the compressional wave path and S for the shear wave path.

Table 4.1: Ultrasonic channels for monitoring acoustical transparency of the crack interface. Dimensions of the transmitting and receiving elements are given accordingly.

Wave type	Reflection channel/Probe dimensions	Transmission channel
Compression	$C1-C1/(16\text{mm} \times 24\text{mm} - 12\text{mm} \times 16\text{mm})$	–
	$C2-C2/(16\text{mm} \times 24\text{mm} - 12\text{mm} \times 16\text{mm})$	–
	–	$C1-C2$
	–	$C2-C1$
Shear	$S1-S2/(18\text{mm} \times 18\text{mm} - 13\text{mm} \times 13\text{mm})$	–
	$S3-S4/(18\text{mm} \times 18\text{mm} - 13\text{mm} \times 13\text{mm})$	–
	–	$S1-S4$
	–	$S3-S2$

3500 kN. In the absence of a compressive load, only reflections from the artificial interface were recorded by the reflection channels. As the compressive load increases, the two blocks are pressed together and ultrasonic waves start propagating through the contact interface and transmissions signals are recorded. Figure 4.2 illustrates a typical example of recorded signals, the so-called A-scans, in reflection and transmission modes, as collected by the ultrasonic multi-channel acquisition system.

In Figures 4.3 and 4.4, amplitudes of reflected and transmitted signals are plotted against compressive load for compressional and shear waves, respectively. It can clearly be seen that the amplitude curves for both modes and wave types exhibit different slopes as the applied force increases. For instance, in the case of *compressional* waves and at an applied load of approximately 50 kN, the reflected signal gives an amplitude of

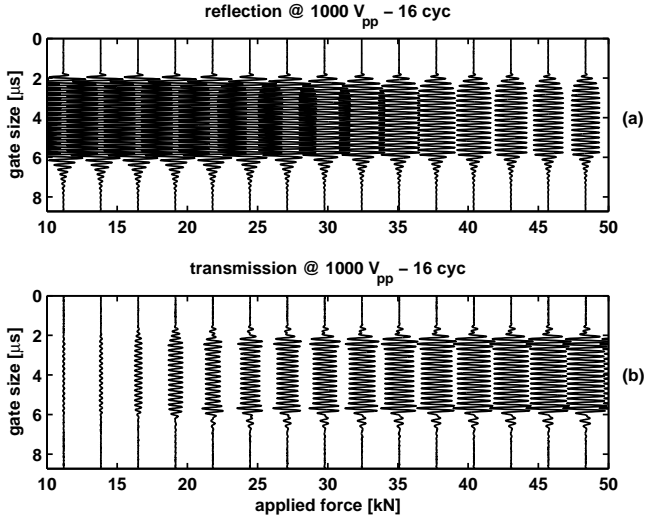


Figure 4.2: Typical example of signals, the so-called A-scans, recorded by the reflection channel C1-C1 (a) and the transmission channel C1-C2 (b). By increasing the compressive load, the amplitude of the reflected signals decreases, while the amplitude of the transmitted waves increases.

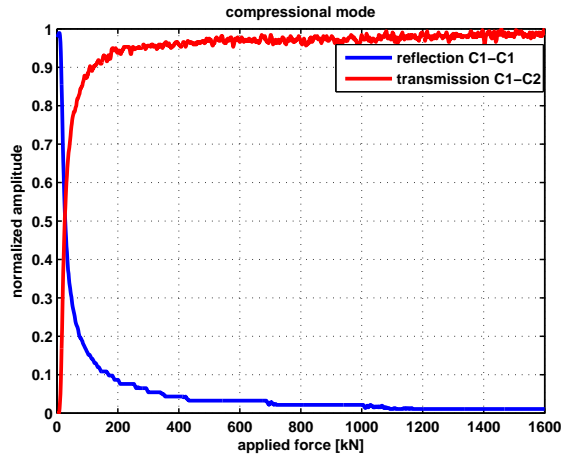


Figure 4.3: Normalized amplitudes of the reflected and transmitted waves at increased load, recorded by the compressional wave channels C1 - C1 and C1 - C2, respectively.

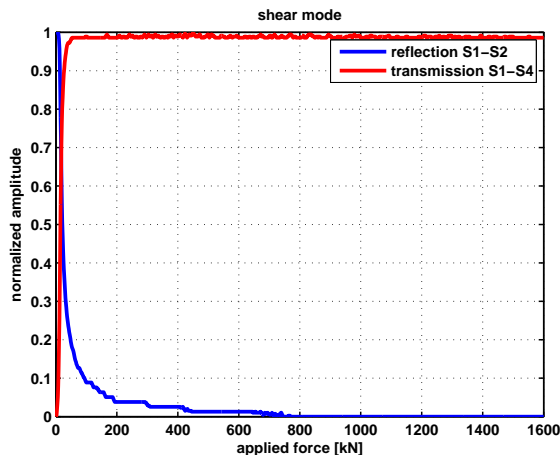


Figure 4.4: Normalized amplitudes of the reflected and transmitted waves at increased load, recorded by the shear wave channels $S1 - S2$ and $S1 - S4$, respectively.

28 % relative to the incident signal, while the transmitted one reaches 76 %. For *shear* waves, transmission through the artificial interface started at very low values of the applied loading force (< 5 kN) and approaches its maximum value of 98 % very quickly. Nevertheless, at the same force value, reflection is still visible with an amplitude of 28 %. This observation suggests that reflection and transmission at this load value, are not balanced in terms of energy. This may be explained by the fact that the crack asperities are mechanically coupled by the shear mode and are suitably aligned for the shear incidence allowing for an early saturation of the transmission mode. Obviously, when the load is further increased, the reflection and transmission values are balanced again as the crack asperities are fully pressed together and the reflection tends to zero.

4.1.3 Detection of harmonics

To examine the response of the artificial interface, when intense input amplitudes are applied, a setup for harmonic detection was designed. The same arrangement as shown in Figure 4.1, including probes, was re-used for these experiments. The previous ultrasonic multi-channel acquisition system is used for data collection, while signal generation and amplification are performed by an arbitrary wave generator (AWG) and a gated amplifier (Figure 4.5). It should be emphasized that the ultrasonic probes were specially designed for higher power excitation and harmonic detection. The compressional wave probes consist of two elements, incorporated in one housing, with the transmitting element exhibiting a narrowband spectrum with a center frequency of 4 MHz, and the receiving element having a wideband spectrum with a center frequency of 8 MHz. The bandwidths of both crystal elements were chosen in such a way that possible harmonics carried in the excitation spectrum are reduced, whereas harmonics that may result from the vibration of the crack interface are well recorded by the receiving element. The shear wave probes, however, are single angled elements, transmitting at 40° with 4 MHz center

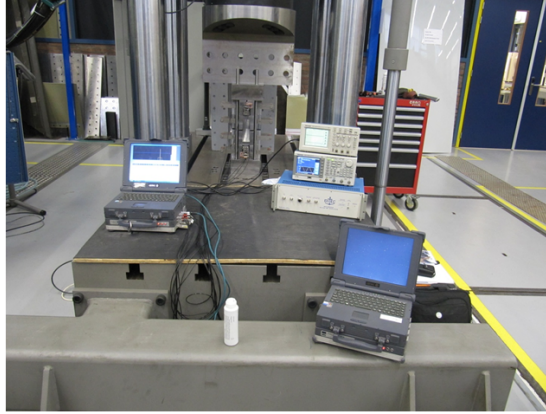


Figure 4.5: *Picture of the experimental setup, where the stacked steel blocks are loaded under the electro-hydraulic testing machine.*

frequency on one side, and receiving at the same angle with 8 MHz center frequency on the other side of the artificial interface.

In these measurements, the excitation voltages and the number of pulse cycles were varied from 200 V_{pp} up to 1200 V_{pp} and from 4 cycles up to 24 cycles, respectively. Following the previous measurement procedure, the steel blocks were compressively loaded until the reflected signal vanished completely. This was monitored from both sides of the artificial interface using the reflection and transmission channels. An example of data, in which a partial crack closure can be seen, is shown in Figure 4.6. Since the signal generator is a one-channel excitation system, compressional and shear wave experiments were carried out successively. Figure 4.7 shows the amplitude response of the artificial interface recorded by the reflection channel $C1 - C1$ at various excitation voltages and at 24 cycles. It can be seen that the amplitude decay is comparable for all excitation voltages and exhibits the same slope with increasing load up to a value of 1600 kN, at which a complete crack closure occurs.

To assess the nonlinear behavior of the interface motion under a compressive load, the excitation voltages and the number of pulse cycles of the incident wave packet were varied. It is well-known that harmonics might arise from the acquisition system, e.g., from the amplifier, when higher excitation voltages are used. To reduce this effect and avoid distortion of the input signal, precautionary measures related to signal amplification, attenuation and probe design were taken. Furthermore, the properties and sizes of the crystals were chosen in such a way that optimal transformation into sound wave energy could be achieved.

To reliably quantify harmonics generated by the acquisition system, a reference measurement without loading force was performed for which the dual probe was excited at various voltage levels and at various numbers of pulse cycles. In this way, a power spectra

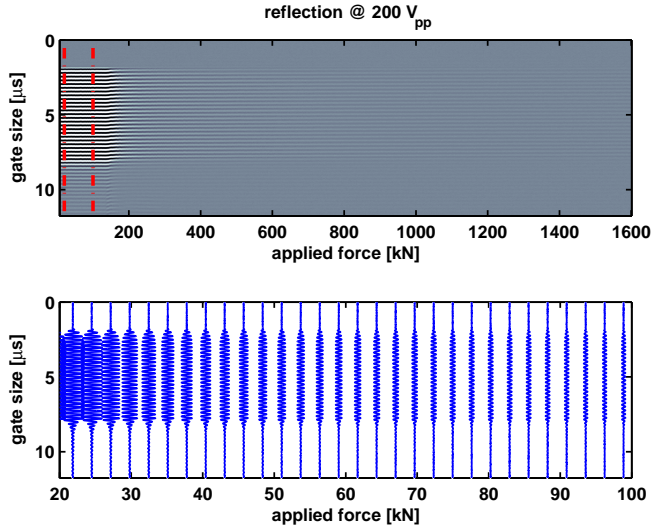


Figure 4.6: Typical amplitude responses of the crack interface in reflection mode as a function of increased load, at $200 V_{pp}$ excitation voltage and 24 pulse cycles. By increasing the load, the amplitude of the reflected signals decrease gradually.

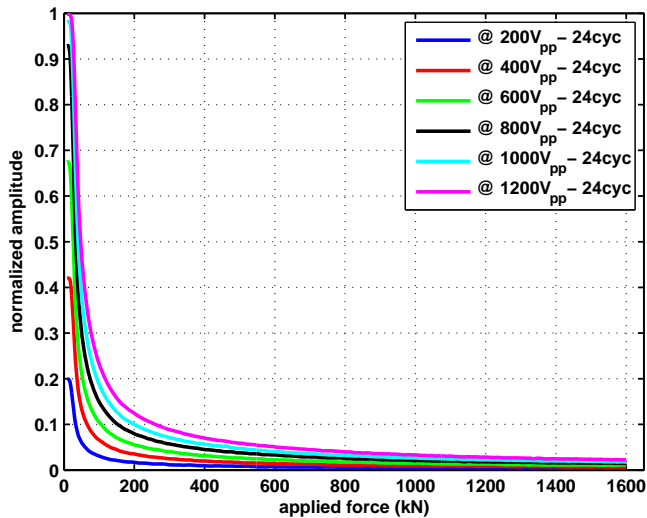


Figure 4.7: Normalized reflected amplitudes recorded by the dual compressional wave probe C1 - C1 at various excitation voltages (peak-to-peak values). Complete crack closure occurs at 1600 kN.

footprint of the acquisition system for each excitation voltage level was obtained. Figure 4.8 shows an example of the power spectrum of the acquisition system at 1200 Vpp excitation voltage with a sinusoidal wave of 24 cycles. For these input parameters, frequencies up to the fourth harmonic are clearly visible in the frequency spectrum. Due to the signal shape obtained at this excitation voltage, it can be seen that the fundamental (f) and its odd harmonics ($3f$ and $5f$) are dominant compared to its even harmonics ($2f$ and $4f$) in terms of amplitude responses.

As expected, the harmonics that may result from the interface motion due to high amplitude ultrasonic waves, are mixed with those introduced by the acquisition system. Before extracting the contribution of the artificial interface to the generated harmonics, let us first map the amplitudes of the fundamental frequency and its harmonics against the loading force. Figure 4.9a shows the power spectra and the corresponding amplitudes as a function of loading force at an excitation voltage of 1200 Vpp with a sinusoidal wave packet of 24 cycles. Clearly, both the fundamental frequency and its harmonics are influenced by the increased loading force. For example, by comparing power spectra of traces 30 (Figure 4.9b) and 350 (Figure 4.9c), it can be observed that the higher harmonics vanish, while the fundamental is more pronounced and that the second harmonic is still visible.

To extract the contribution of the artificial interface to the harmonics generated, the magnitude of each spectrum trace at each force step was selected and normalized to the magnitude of the first trace. Figure 4.10 shows the magnitude variation of the fundamental frequency and its harmonics at a fixed excitation voltage and at various numbers of pulse cycles. It can be observed that the amplitudes of the fundamental, third and fourth harmonics decrease dramatically as the applied force reaches 30 kN (Figure 4.10 a,c,d). At the same load value, however, the amplitude of the second harmonic increases substantially, which may be explained by the non-linear contribution of the

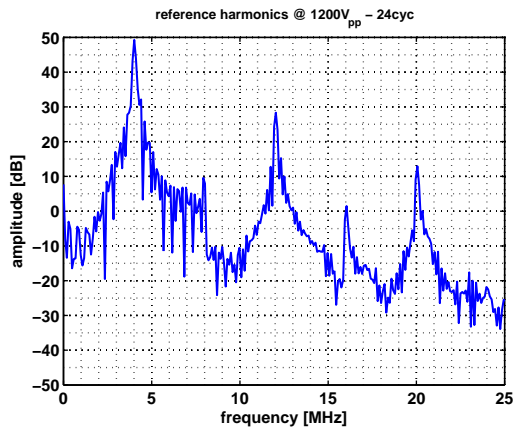


Figure 4.8: Harmonics generated at zero load by the acquisition system recorded by the reflection channel C1 – C1 at 1200 Vpp and 24 pulse cycles.

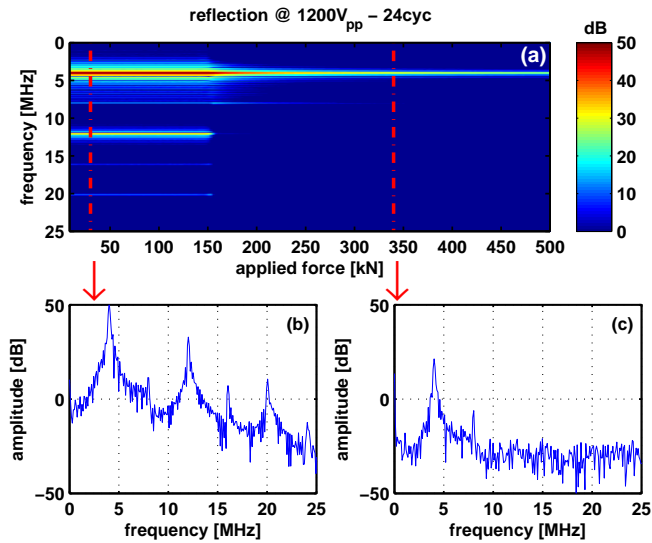


Figure 4.9: Power spectra of harmonics reflected at 1200 V_{pp} - 24 cycles as a function of loading force recorded by the reflection channel C1 – C1: Spectrum of trace 1 through trace 500 kN (a) and frequency spectrum of traces 30 kN (b) and 350 kN (c), respectively.

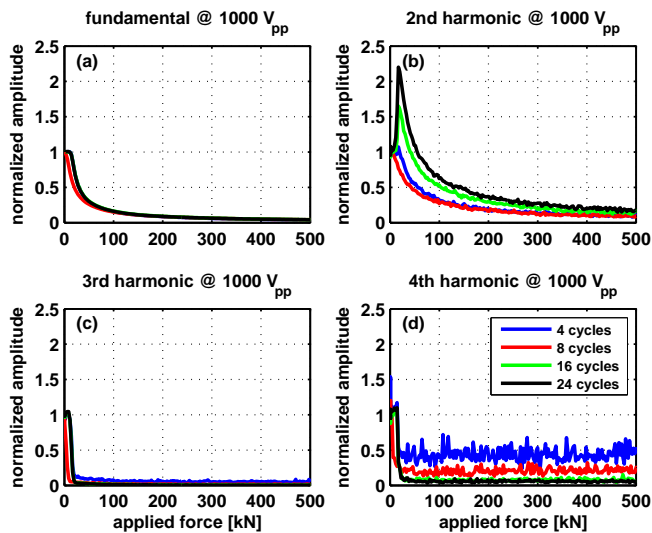


Figure 4.10: Normalized amplitudes of the fundamental frequency and its harmonics at increased load, 1000 V_{pp} excitation voltage, and at various number of pulse cycles: Fundamental frequency (a), second harmonic (b), third harmonic (c) and fourth harmonic (d).

crack interface to second harmonic generation. This observation is in a good agreement with the predictions of the numerical results illustrated in Figures 3.5 to 3.10 of Section 3.2. Obviously, a larger number of pulse cycles has much more effect on harmonic generation, as the crack planes are strongly pushed close to each other, resulting in a powerful vibration of the crack interface. It can also be observed that the third and fourth harmonics have an abrupt decay compared to the fundamental and the second harmonic, which decrease smoothly as the applied force increases.

4.2 Fatigue crack interface

4.2.1 Fatiguing of a test specimen

Fatiguing of a test specimen requires precautionary measures in terms of notch preparation, applied load (stress intensity) and crack growth. To confirm harmonic generation at a real fatigue crack and to verify the observations made in the previous experiments, a carbon steel block (400 x 200 x 200 mm) was fatigued using three-point bending method (Figure 4.11). To ensure a controlled crack initiation at one position, a sharp V-notch was introduced at the center of the block and extended along the width of the block (normal to the drawing plane). To avoid crack initiation in the vicinity of the notch, the corners of the slit area were finished with a radius. Furthermore, the block was equipped with two openings machined at 100 mm from the notch centerline, through which the probe holders slide up and down. It should be noticed that the block was designed in such away that the probe arrangement, as previously shown in Figure 4.1, is maintained for these experiments. A direct advantage of this design is to re-use the same probes and to benefit from the previously prepared acquisition files, data handling and analysis tools.

Prior to fatigue testing, the two probes *C1* and *C2* were mounted in the sliding holders and positioned in such way that the incident ultrasonic beam partly reflects on the tip of the notch and partly transmits in the pitch-catch mode using ultrasonic channels

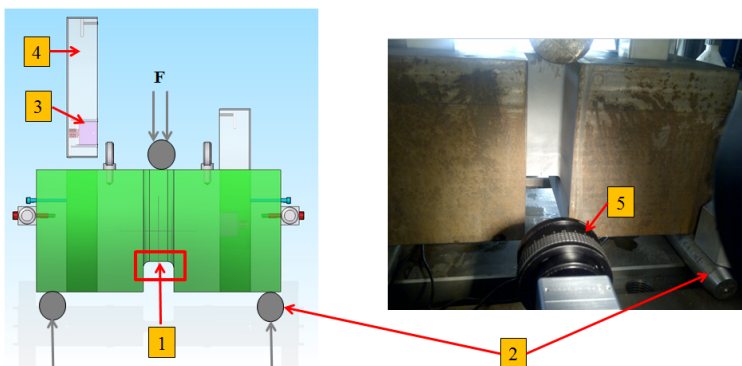


Figure 4.11: *Fatigued block of dimensions 400 x 200 x 200 mm (L x W x H) used in the experiments: numbers 1 through 5 indicate the notch, bending points, probe, probe holder, and camera, respectively. the force is applied from the top.*

$(C1-C1, C2-C2)$ and $(C1-C2, C2-C1)$, respectively. Due to this arrangement, crack initiation and growth were monitored as a function of the applied cyclic load. To accurately register crack initiation and growth, a two-dimensional optical tracking method, the so-called digital image correlation (DIC), was applied (Sutton et al. 2009). In this method, deformation of the object is tracked through changes in images (grey levels) at successive time steps, as shown in Figure 4.12. Based on correlation algorithms, strain is deduced from differences in displacement between a deformed subset at time t_1 and a reference subset at time t_0 .

During fatiguing tests, the block was initially loaded at 290 kN with a testing frequency of 10 Hz. Once the crack was initiated (at about $9 \cdot 10^4$ cycles), snapshots of the crack, at intervals of 10^4 cycles, were made. By monitoring the speed of crack propagation, the applied load was gradually adapted and reduced down to 180 kN for the remainder of the fatiguing test (approximately $7 \cdot 10^5$ cycles), ultimately resulting in a crack length of 53 mm. Figure 4.13 depicts a section of the initiated crack with a typical DIC image. In this image, the red color code corresponds to regions with high strain values, whereas the blue-violet color code represents regions of minimum strain values. Near the crack tip, a greenish area is visible, which represents the plastic region resulting from high stress concentration near the tip (Choi 1998).

4.2.2 Crack closure and harmonic generation

After completion of the fatigue tests, the steel block was turned over as shown in Figure 4.14 in order to apply a load as in the case of the artificial interface. To realize crack closure and investigate reflection and transmission at crack asperities under compressive load, the same procedure explained in section 4.1.2 was followed here. Figure 4.14 schematically illustrates the probe configuration used for the measurement of crack closure. In this setup, and at zero load, the probe arrangement was fixed at a position, at which reflection from the crack area showed a maximum. As soon as the load was applied, ultrasonic waves start to propagate through the crack interface. Figure 4.15 de-

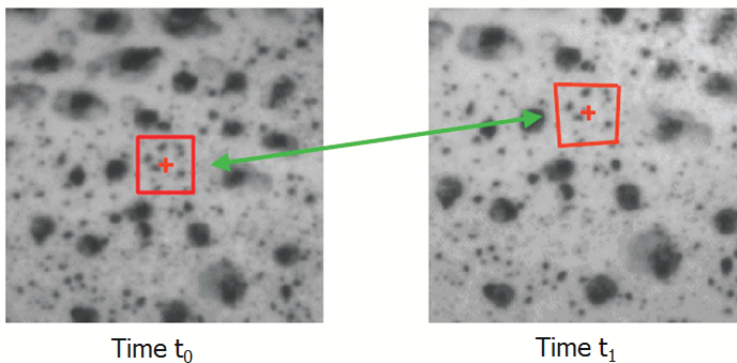


Figure 4.12: DIC method based on point-tracking of local neighborhoods: reference image at time t_0 (left), deformed image at time t_1 (right) (Sutton et al. 2009).

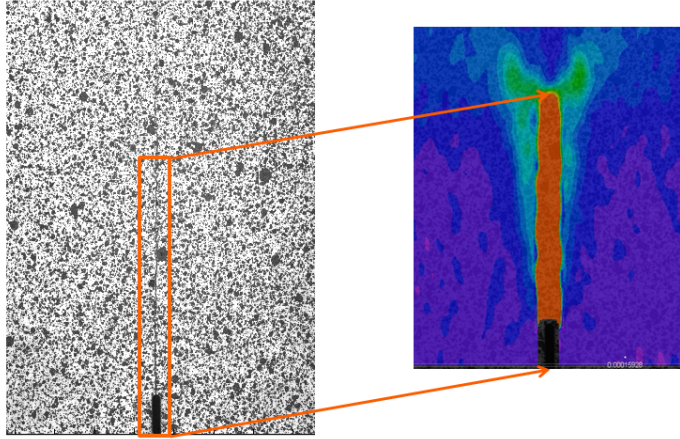


Figure 4.13: Fatigue crack with the corresponding DIC image. The red and blue-violet color codes correspond to high strain and low strain regions, respectively. The greenish area represents the plastic zone near the crack tip.

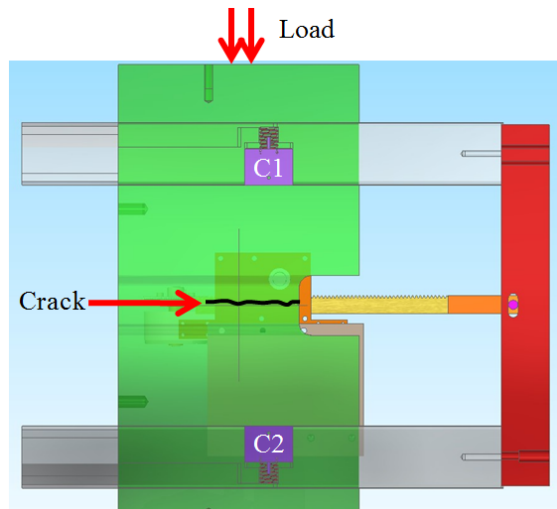
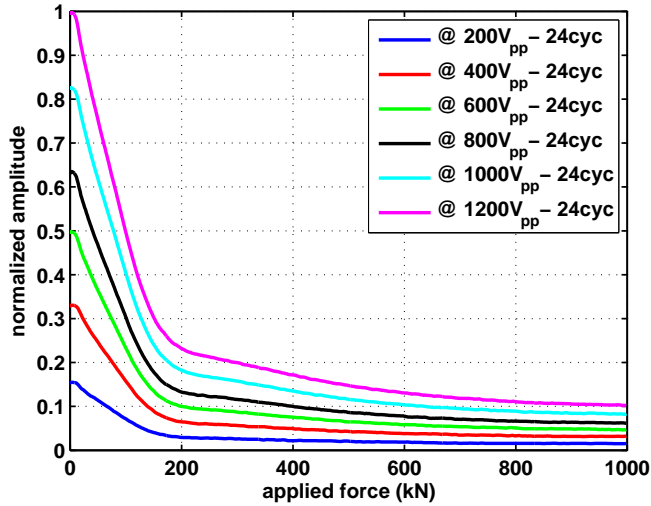


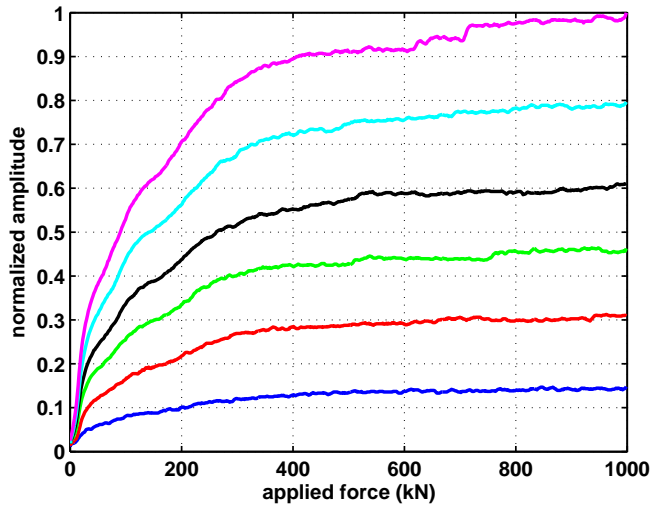
Figure 4.14: Front view along the the crack plane of the experimental setup used for crack closure. The probe arrangement is mounted at a fixed distance allowing for backward and forward movement.

picts reflection and transmission amplitudes as a function of the applied load at different input voltages and at a fixed number of pulse cycles. To avoid major deformation of the crack interface and roughly maintain the crack morphology, the maximum load was kept at 1000 kN which was much lower than in the case of the artificial interface. Comparing the reflected amplitudes of the crack interface (Figure 4.15a) and the artificial interface (Figure 4.7), a slight difference can be observed in amplitude decay and in the slope of the curves. For instance, at 1200 V_{pp}, the relative reflection amplitude of the real interface is 23 %, while the artificial interface reflects 12 % only. Obviously, this is due to differences in the real area of contact achieved in both cases at the same compressive load.

To evaluate harmonic generation at the fatigue crack interface, Figures 4.16 to 4.19 show the magnitude evolution of the fundamental frequency and its harmonics at increased load for both reflection and transmission channels, respectively. It can be observed that amplitudes of the fundamental frequency and the second harmonic of the reflected signals decrease by increasing load. Looking closer at both curves, the decay mechanism of the second harmonic is slightly different compared to that of the fundamental frequency. For instance, at approximately 200 kN, the amplitude of the fundamental frequency decreased by 13 dB, while the amplitude of the second harmonic shows a decrease of 6 dB only. In the case of transmission, however, the slope of the second harmonic curve shows two inflections points at approximately 138 kN and 276 kN. This change in slope sign might be linked to crack closure and the level of non-linearity exhibited by this crack interface.



(a)



(b)

Figure 4.15: Normalized reflected (a) and transmitted (b) amplitudes of the fundamental frequency at increased excitation voltages and increased load, recorded by channels C1 – C1 and C1 – C2 on a real fatigue crack, respectively.

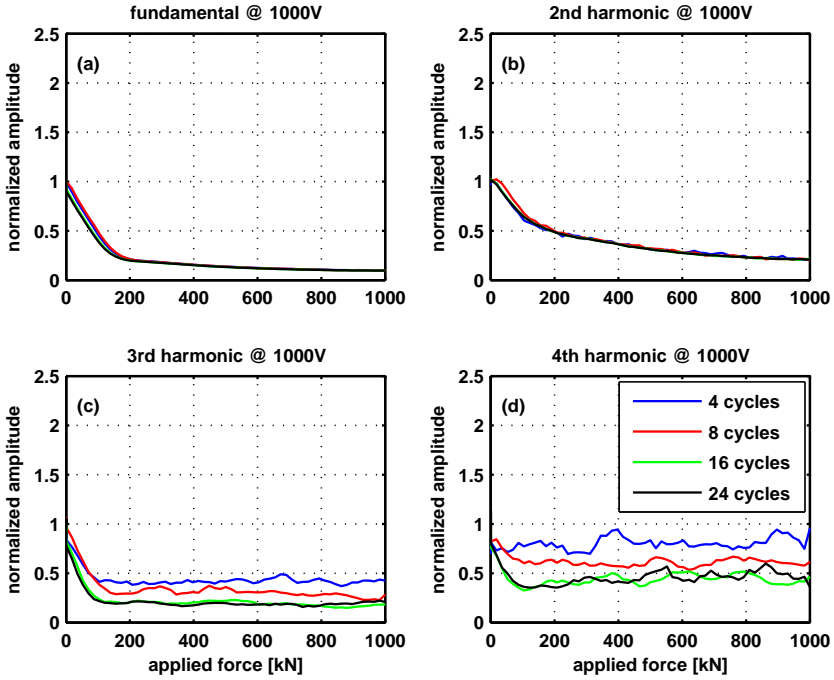


Figure 4.16: Normalized amplitudes of the reflected fundamental frequency and its harmonics at increased load, 1000 V_{pp} excitation voltage, and at various numbers of pulse cycles: fundamental frequency (a), second harmonic (b), third harmonic (c), and fourth harmonic (d).

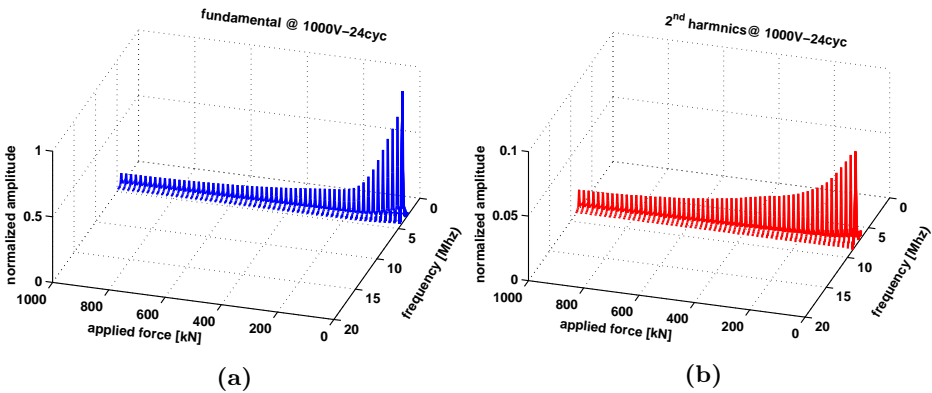


Figure 4.17: 3D-illustration of normalized amplitudes of the fundamental frequency (a) and second harmonic (b) in reflection mode collected by the reflection channel C1 – C1.

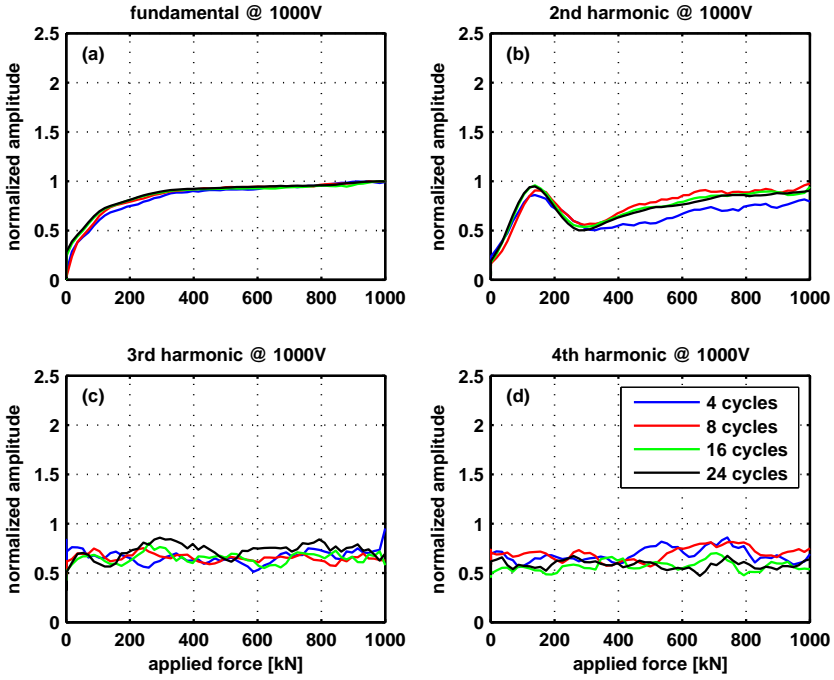


Figure 4.18: Normalized amplitudes of the transmitted fundamental and its harmonics at increased, 1000 Vpp excitation voltage and at various numbers of pulse cycles: fundamental frequency (a); second harmonic (b), third harmonic (c), and fourth harmonic (d).

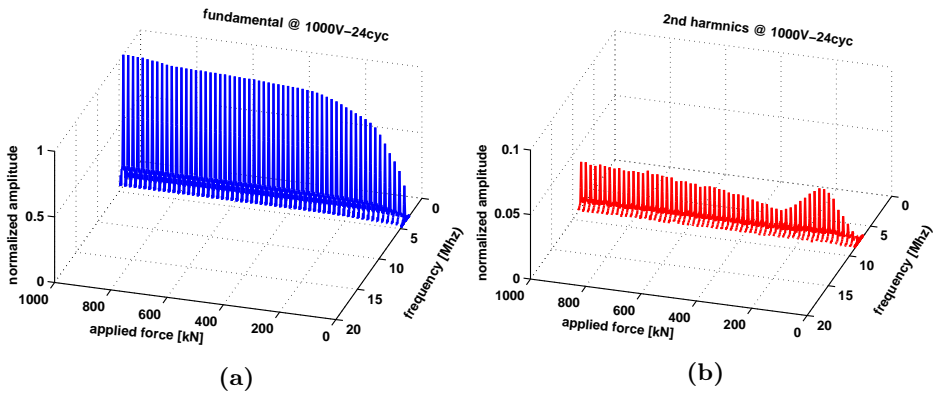


Figure 4.19: 3D-illustration of normalized amplitudes of the fundamental frequency (a) and second harmonic (b) in transmission mode recorded by the transmission channel C1 – C2.

4.2.3 Harmonic detection along the crack length

To get more insight into crack closure and harmonic generation at different crack positions, a scanning mechanism was required. For this purpose, a motor-driven probe system was designed. The probes were spring-loaded, thereby allowing for a reliable probe contact with the test specimen and a constant ultrasonic coupling. Therefore, consistency of the measurements during forward and backward movement of the probes was maintained. To record the scanning position, a pulse encoder was attached to the probe arrangement. Figure 4.20 shows a three-dimensional design and a photograph of the the experimental setup including the fatigued block and the scanning configuration used for these experiments.

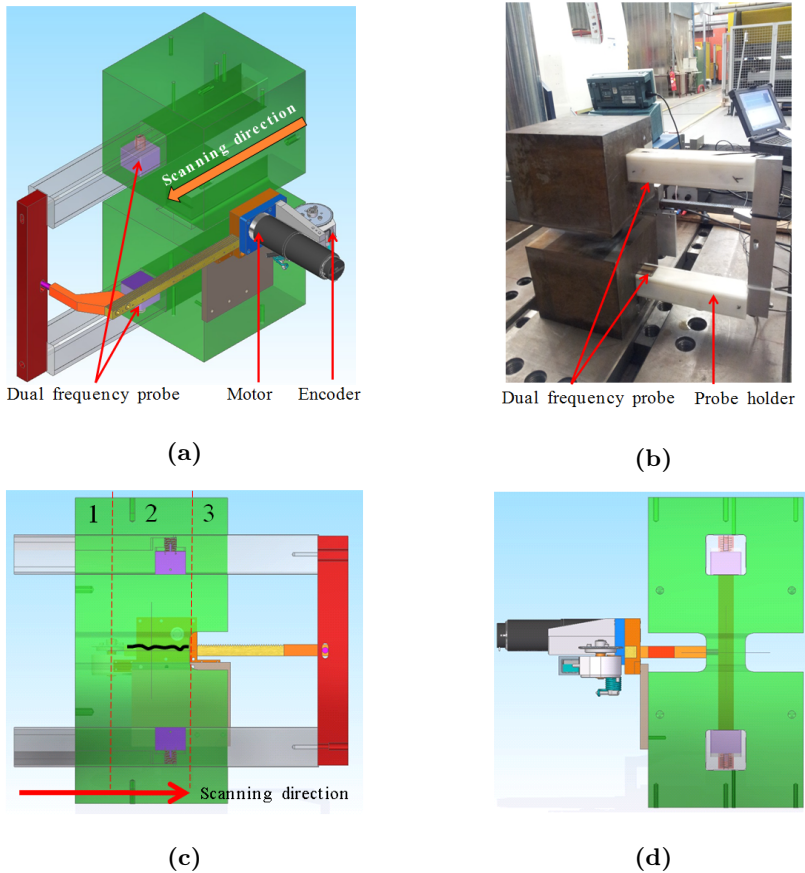


Figure 4.20: Setup for crack closure and harmonic detection measurements: Schematic illustration of the setup (a), fatigued block with corresponding scanning probe system (b), front view (c), and top view (d) of the scanning configuration \parallel and \perp to the crack plane, respectively.

In Figure 4.20c, three sections are defined being uncracked (1), cracked (2) and block-end (3). By scanning from region (1) towards region (3), different data sets related to these regions were collected in both reflection and transmission modes. To reduce the amount of data, the number of pulse carriers was set at 24 cycles, whereas the voltage was varied from 200 Vpp to 1200 Vpp in steps of 200 Vpp. Furthermore, the load was varied from 0 kN to 100 kN in steps of 10 kN. A typical example of reflected and transmitted data collected at 200 Vpp and 1200 Vpp in the absence of load is depicted in Figure 4.21. In this example, data corresponding to each region as defined above, is nicely visualized by stacking different signal traces (A-scans) along the scanning direction. It can be noted that even in the absence of a load, transmission through the crack interface strongly

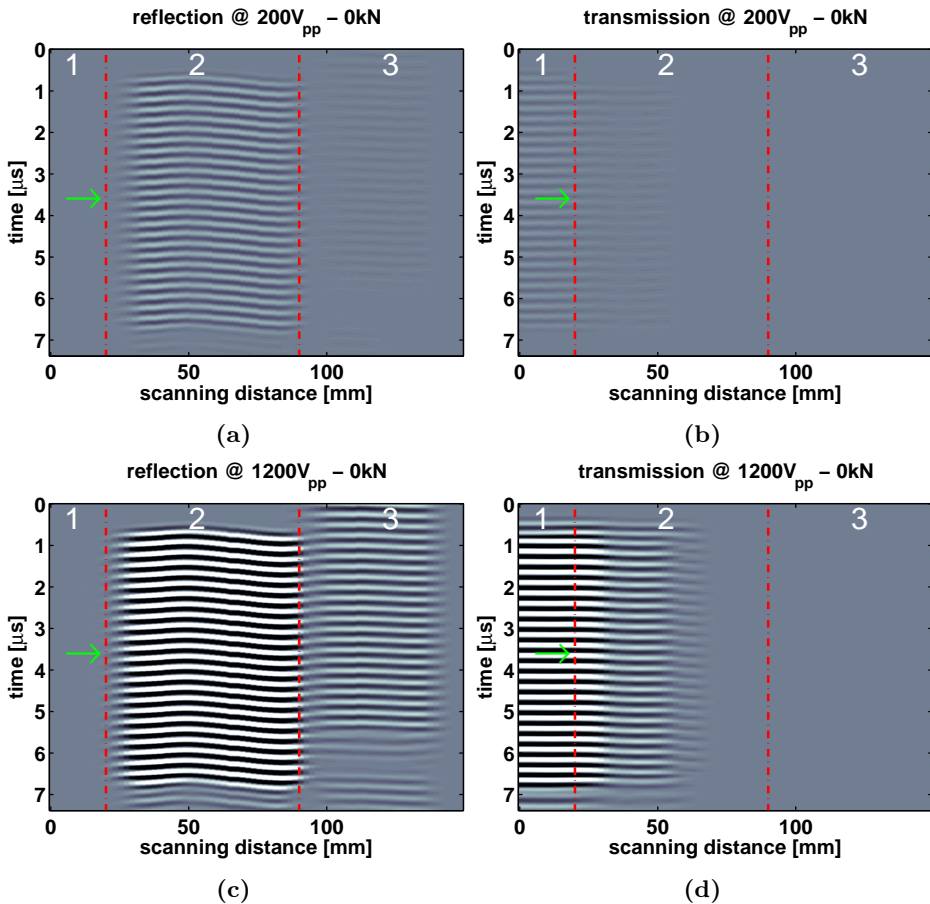


Figure 4.21: Typical B-scan presentation of data collected by reflection channel (a,c) and transmission channel (b,d) at 200 Vpp, 1200 Vpp and zero load, respectively. Numbers 1, 2 and 3 correspond to ultrasonic data collected at the uncracked, cracked and block-end regions, respectively.

increases when raising the excitation voltage to 1200 Vpp.

To closely assess the crack response at different loads and excitation voltages, frequency analysis of each signal trace in reflection and transmission modes is needed. For the sake of simplicity, let us compare the crack response at three different loads for a fixed input voltage and a fixed number of pulse cycles as illustrated in Figure 4.22. For this specific crack position (signal trace), applied load and excitation voltage, it can be seen that the shape and the amplitude of the reflected waveform remain the same when the load is increased from 0 kN to 50 kN, while the transmitted waveform distorts noticeably at 10 kN, and the related amplitude changes as well. By looking at the frequency content of the transmitted signals and by comparing harmonic magnitudes, a remarkable increase of approximately 9 dB of the second harmonic magnitude can be observed at 10 kN, whereas at the same load value the magnitude of the fundamental frequency decreases by about 12 dB. In contrast, by further increasing the load to 50 kN, the magnitude of the fundamental increases by approximately 20 dB and the amplitude of the second harmonic decreases again by about 4 dB. This can be explained by the fact that at each load value, a different crack shape might be realized and, therefore, different crack responses are expected.

To explore harmonic generation at different crack positions as a function of crack closure, the load was applied with steps of 10 kN, while scanning along the crack length at each load step. Prior to scanning, a reference measurement was performed, in which the load was removed and the crack was scanned at different excitation voltages for a fixed number of pulse cycles. Figures 4.23 and 4.24 show the crack response at zero load with its spectrum content at 1200 Vpp in reflection and transmission modes along the crack length, respectively. Obviously, at this excitation voltage and even though the load was removed, ultrasonic waves were transmitted through the crack interface, especially near the crack tip. This observation can simply be verified by comparing, for instance, signal amplitudes of traces 30 and 40 in both modes. Hence, by following the scanning direction, the crack interface reflects more and transmits less towards signal trace 40 as displayed in Figures 4.23a and 4.24a. This illustrates the effect that the crack response strongly depends on the crack position and, hence, on local crack closure. Furthermore, it is visible that the second harmonic is generated along this crack section with different magnitudes.

As previously mentioned, by applying a load, it is assumed that new contact areas between crack asperities are introduced. Therefore, different crack responses to ultrasonic waves are expected. This can be demonstrated on the same traces as in the case of the reference measurements, by applying the load step-wise and scanning along the crack length at each step. As an example, in Figures 4.25 and 4.26, the collected signal traces with related frequency spectra for both reflection and transmission modes at 10 kN are depicted. Regarding the reflected waveforms and the corresponding spectral content, it is hard to see any difference in terms of wave shape and amplitude of the harmonics for these traces. In contrast, the ultrasonic response transmitted through the crack interface exhibits remarkable features, when looking at the waveform (Figure 4.26a) and its magnitude (Figure 4.26b). In this case, the ultrasonic signals are completely distorted. This is related to the generation of the non-linear components introduced by partially closed

areas along the crack length. Furthermore, the magnitude of the fundamental frequency decreases dramatically between signal traces 35 and 40, whereas the magnitude of the second harmonic increases and is more pronounced.

It should be emphasized that the observations made on crack responses in the previous example are generally valid for this setting and for these parameters only. This is because of the fact that at different load values, the crack asperities might be differently aligned, thereby leading to a possible shift of the contact area when the load is varied. As a result, different crack responses are expected along the crack length.

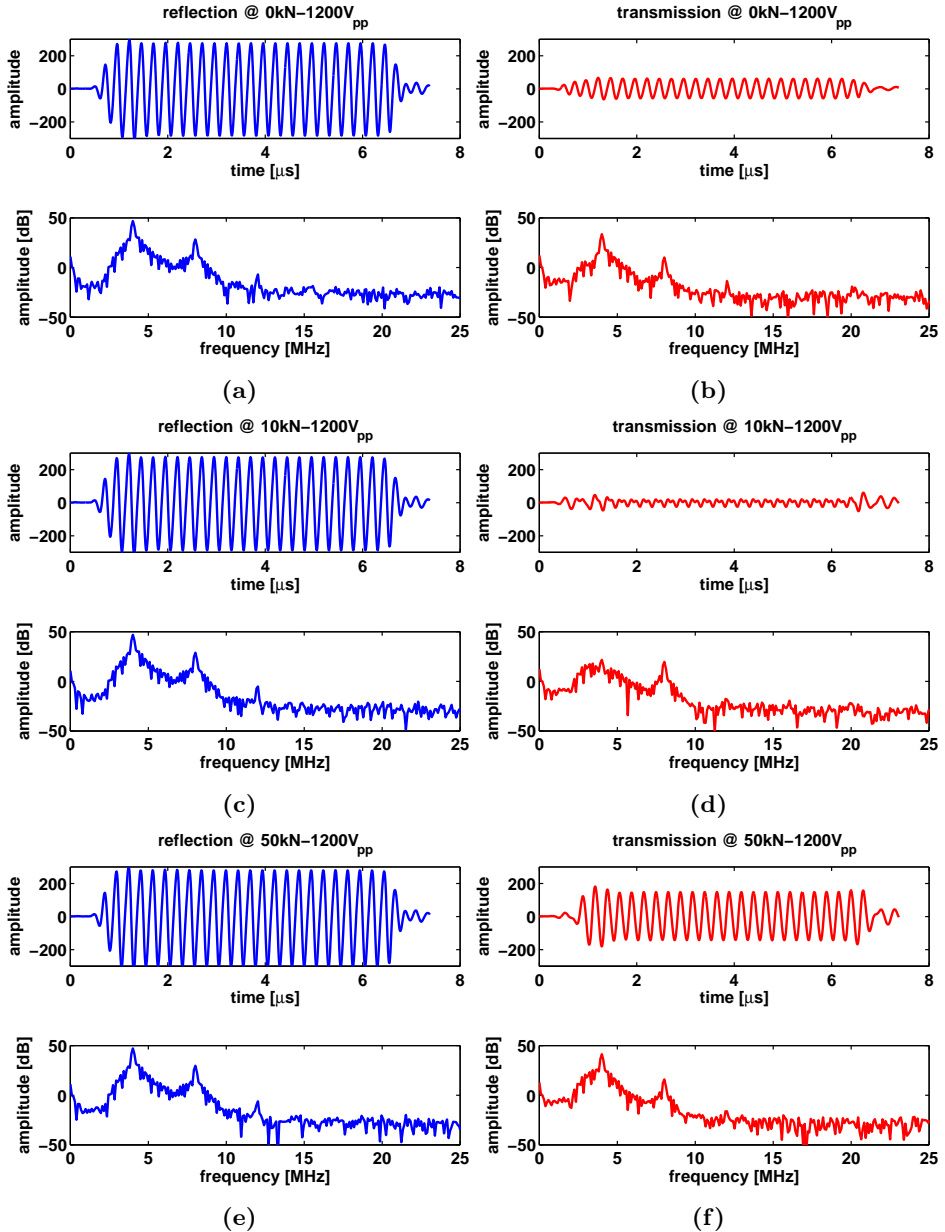


Figure 4.22: Waveforms of signal trace 40 with the corresponding frequency content at 1200 V_{pp} and 24 cycles. Reflection (a,c,e) and transmission modes (b,d,f) at 0 kN, 10 kN and 50 kN, respectively. For comparison purposes, the same scale is used for all magnitudes.

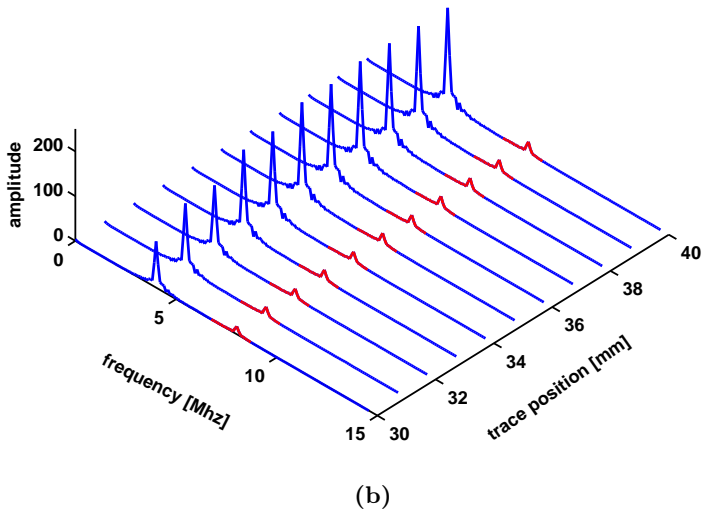
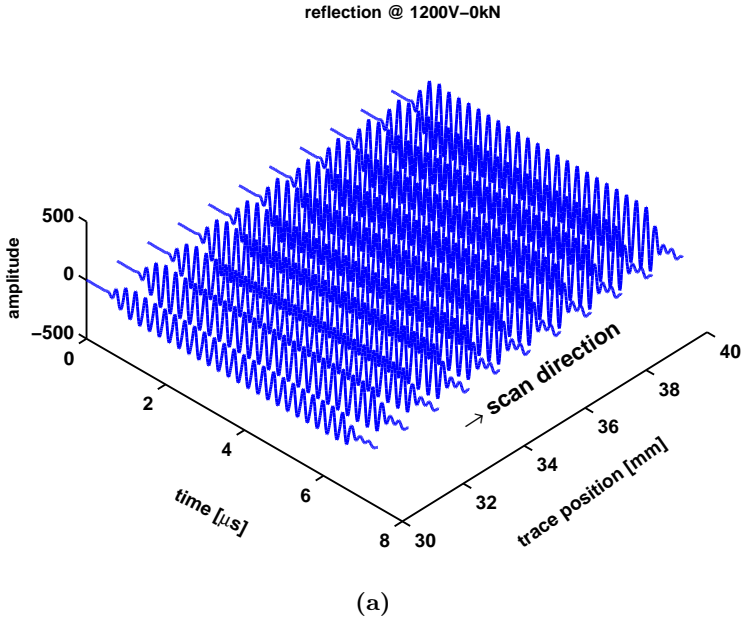


Figure 4.23: Reference waveforms measured by the reflection channel $C1 - C1$ at zero load between traces 30 and 40 (a) with the related frequency spectra (b) at 1200 Vpp and 24 cycles.

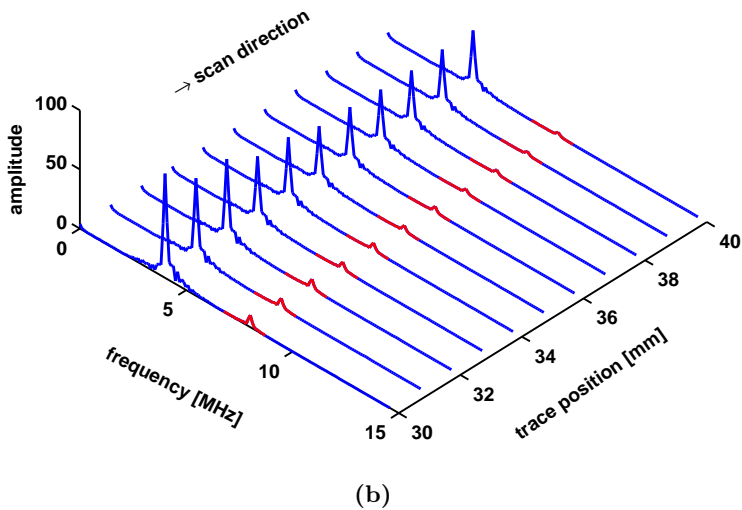
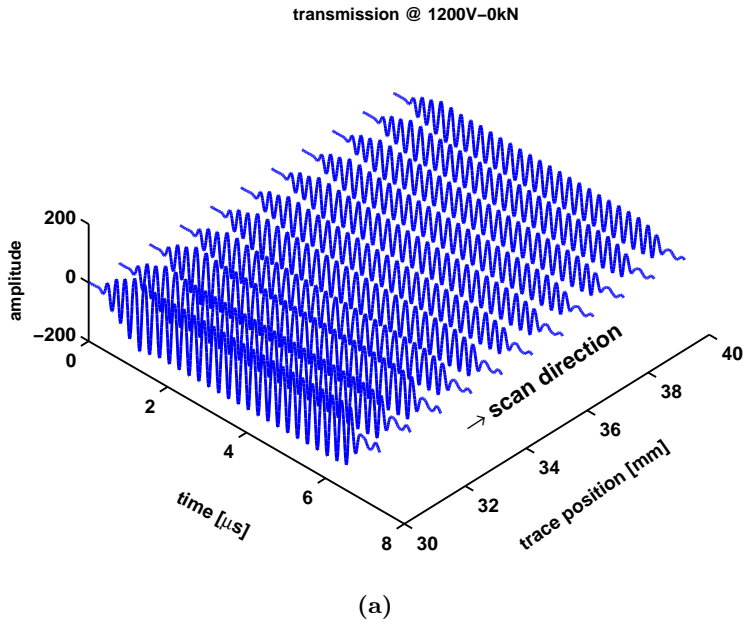
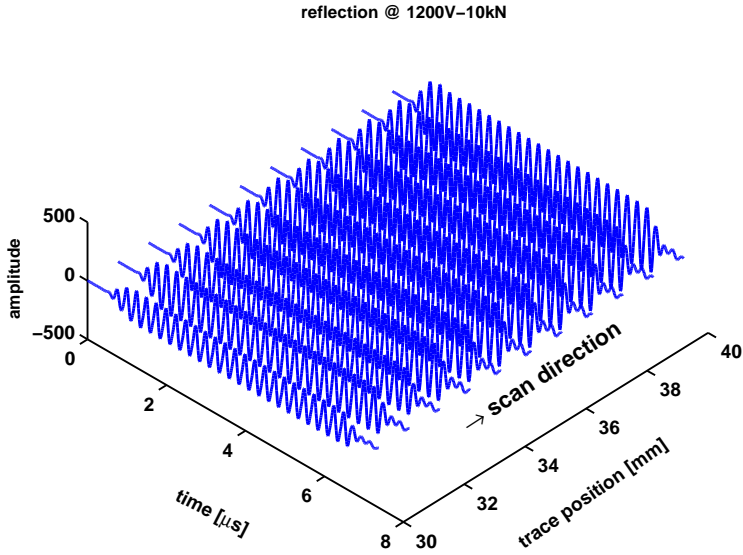
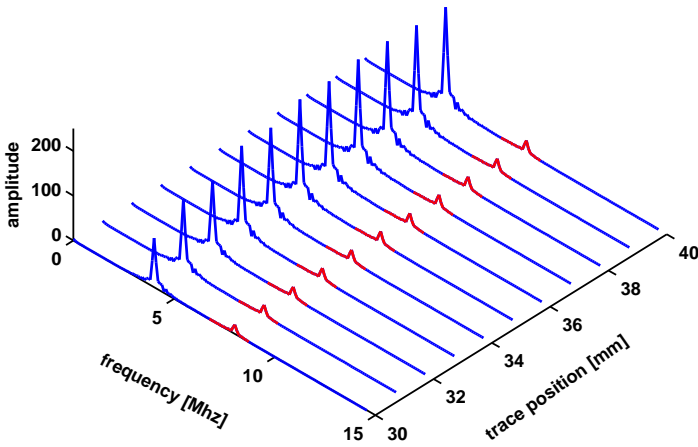


Figure 4.24: Reference waveforms measured by the transmission channel $C1 - C2$ at zero load between traces 30 and 40 (a) with the related frequency spectra (b) at 1200 V_{pp} and 24 cycles.



(a)



(b)

Figure 4.25: Waveforms measured by the reflection channel C1 – C1 at 10 kN between traces 30 and 40 (a) with the related frequency spectra (b) at 1200 V_{pp} and 24 cycles.

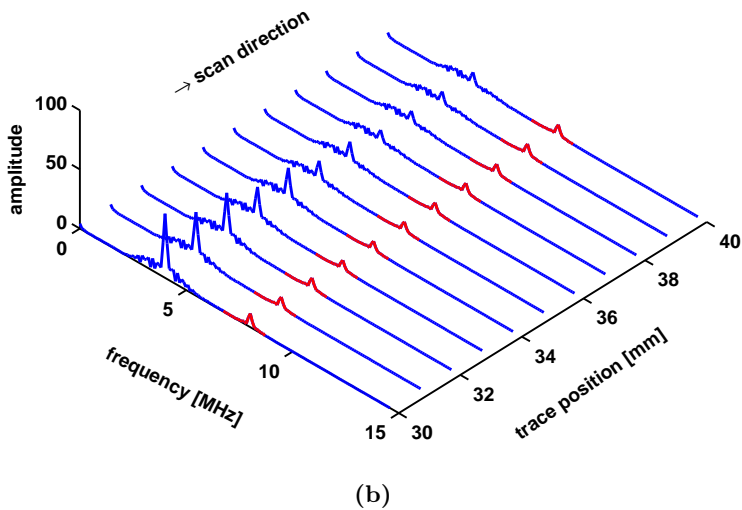
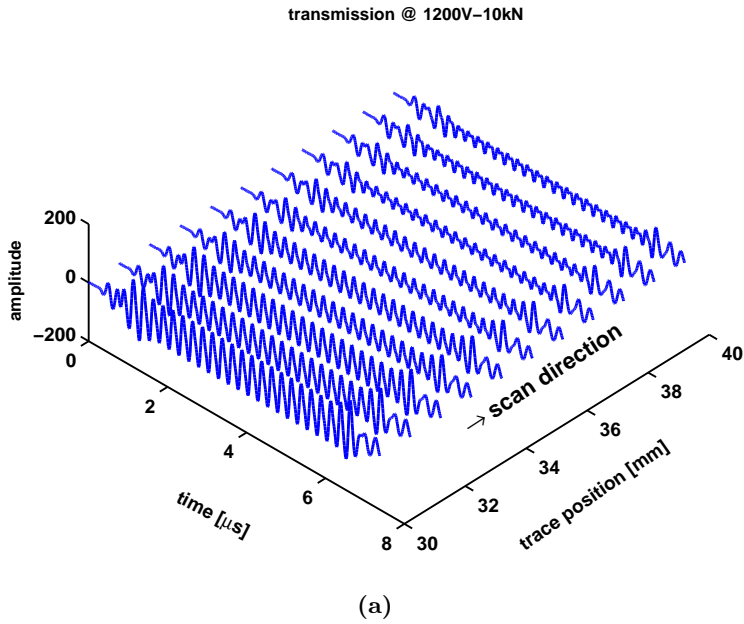


Figure 4.26: Waveforms measured by the transmission channel $C1 - C2$ at 10 kN between traces 30 and 40 (a) with the related frequency spectra (b) at 1200 V_{pp} and 24 cycles.

To extend our analysis of the crack response when the load is applied in combination with the use of different excitation amplitudes, a thorough analysis of harmonics (fundamental frequency and second harmonic) is required. To this end, the magnitudes of the fundamental frequency and the second harmonic of the reflected and transmitted waves at each crack position were selected and normalized to the amplitudes of the harmonics extracted from signal trace 20 (reference trace for reflection) and signal trace 1 (reference trace for transmission), respectively. In this manner, an easier comparison between magnitudes of harmonics, along the crack length, can be made. Figures 4.27 and 4.28 present the magnitude evolution of the reflected and transmitted harmonics at 1200 Vpp input voltage when the load is applied from 10 kN to 50 kN in steps of 10 kN.

As illustrated in these figures, the cracked area is located between position 20 mm and 90 mm. Within this area, the crack response strongly depends on the applied load. For instance, in the case of *reflection*, the crack region between 20 mm and 50 mm is more influenced by increasing load, especially when looking at the magnitude of the fundamental

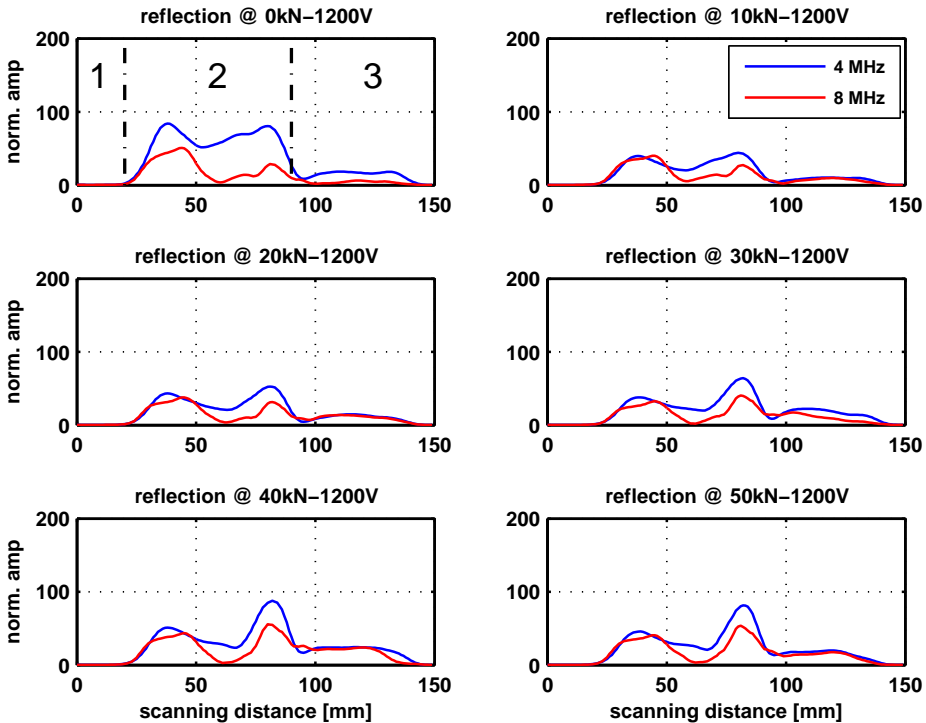


Figure 4.27: Normalized amplitudes of reflected harmonics of various traces at 1200 Vpp - 24 cycles at increased load. All magnitudes are normalized to the amplitude corresponding to the first trace containing the crack tip response (trace 20). Region between the dashed lines represents the cracked area.

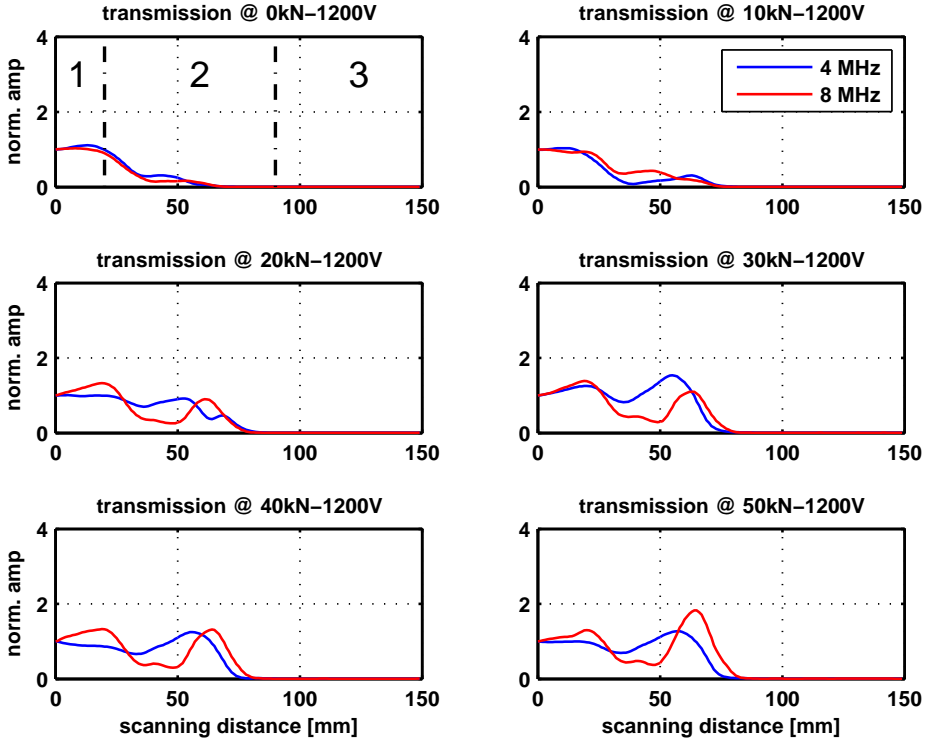


Figure 4.28: Normalized magnitudes of transmitted harmonics of different traces at 1200 V_{pp} - 24 cycles against increased load. All magnitudes are normalized to the amplitude corresponding to trace 1 regarded as a reference. Region between the dashed lines represents the cracked area

frequency. For instance, by applying a load of 10 kN, the magnitude of the fundamental frequency of signal trace 38 decreases by approximately 6 dB, while the magnitude of the second harmonic drops by about 2 dB only. However, by further increasing the load, new contact areas between crack asperities may be introduced along the crack length and, hence, the magnitude of the harmonics changes again. This observation can be illustrated, e.g., at signal trace 82, where the magnitudes of the fundamental and the second harmonic increase by approximately 6 dB when raising the load from 10 kN to 50 kN.

In the case of *transmission*, however, it can be seen that other areas along the crack length are more influenced than in the case of reflection. For instance, at 10 kN the magnitude of the second harmonic increases between position 30 mm and 50 mm, while at 50 kN it increases between position 50 mm and 70 mm. As previously mentioned, this suggests that crack asperities make contact at different locations along the crack length when different loads are applied.

To illustrate the redundancy of information extracted from harmonics analysis, let us plot the harmonics separately in reflection and transmission modes at a fixed input voltage and for three different load values (Figure 4.29). Generally, it can be shown that at different load values (different crack shapes), magnitudes of the fundamental and second harmonic in reflection and transmission modes are influenced accordingly. A remarkable feature can be seen at 50 kN for crack position 65 mm, where both the *transmitted* fundamental and second harmonic show a major increase, while in reflection mode, the corresponding amplitudes remain the same. For instance, at this crack position the magnitude of the *transmitted* second harmonic increases by approximately 28 dB.

To observe the influence of increasing input amplitude on the magnitude of harmonics for a fixed load value and for a given crack shape, the excitation voltage was varied from 200 V_{pp} to 1200 V_{pp} as shown in Figures 4.30 and 4.31. Again, it should be emphasized that at different load steps, a different effective contact area between crack asperities might be realized. Consequently, a reliable comparison between input voltages should be made at a fixed load value. In this example and for comparison purposes, magnitude data of the fundamental frequency and second harmonic are plotted side by side, along the crack length, in reflection and transmission modes.

Obviously, it can be seen that for a fixed load value with a variable excitation voltage, magnitudes of the fundamental and second harmonic in both modes increase accordingly to a change in excitation amplitude. However, at a variable load value and a fixed excitation voltage, the amount of reflection and transmission strongly depends on the realized crack shape. This information can easily be extracted from these figures by looking, for example, at amplitudes of harmonics corresponding to 1200 V_{pp} for different load values. At this voltage, the amplitude of the reflected harmonics increases from 0 kN to 50 kN and drops again when the load is set at 100 kN. By further increasing the load (1000 kN), these amplitudes decrease around crack position 38 mm by 12 dB and 8 dB for the fundamental and second harmonic, respectively. At the same load value, the amplitudes of the transmitted fundamental and second harmonic stabilize and show a comparable value along the crack length.

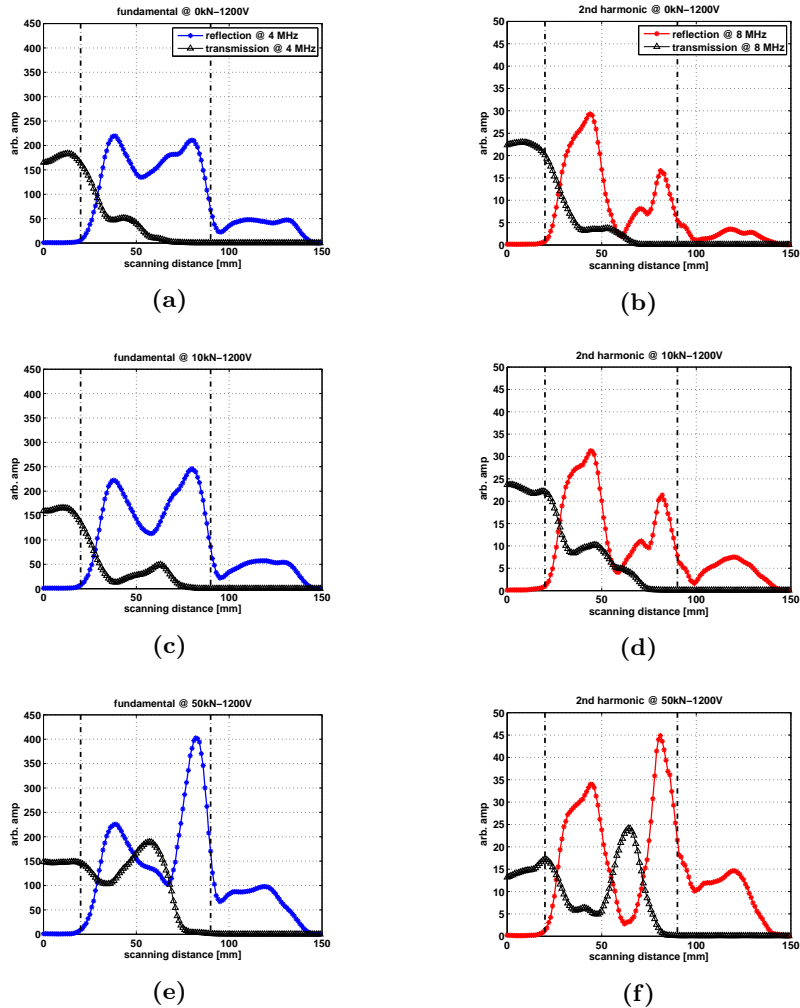


Figure 4.29: Reflected and transmitted amplitudes of the fundamental frequency (a,c,e) and second harmonic (b,d,f) at 0kN, 10kN and 50kN, respectively. Region between the dashed lines represents the cracked area.

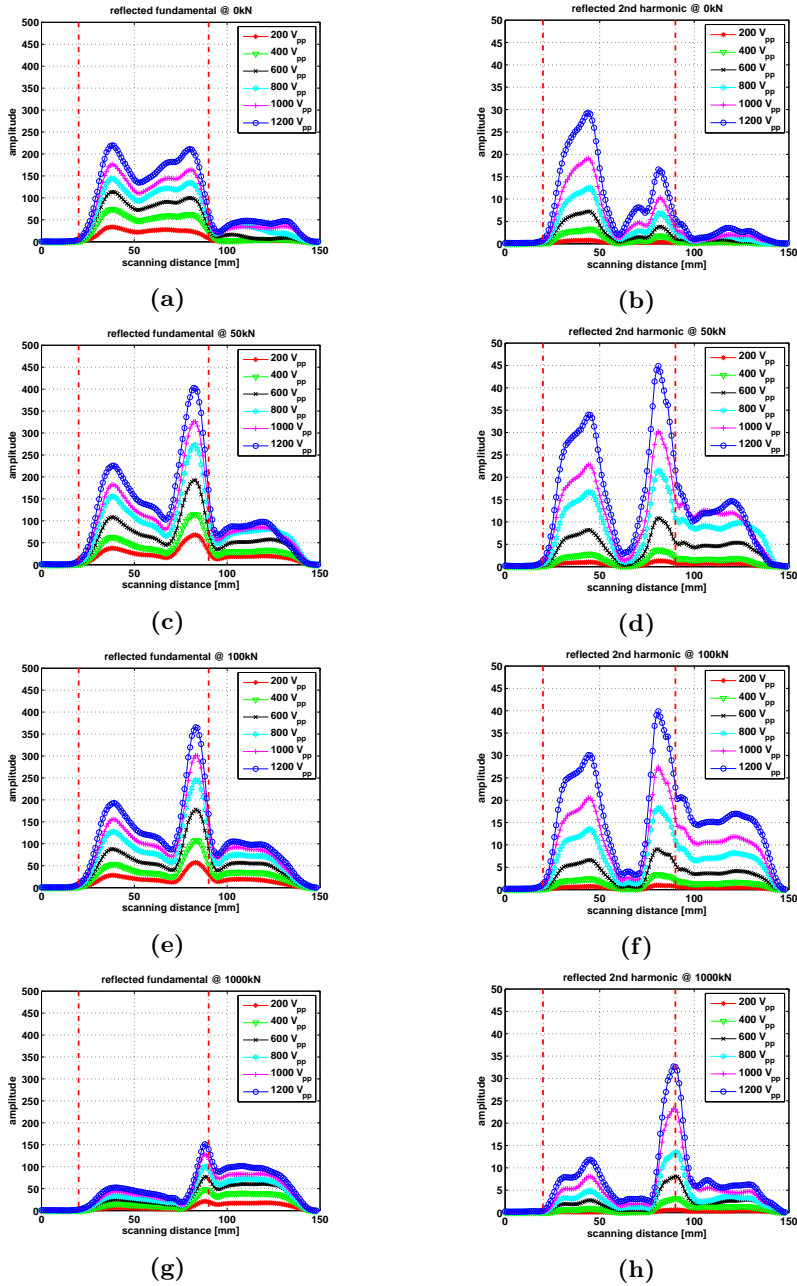


Figure 4.30: Reflected magnitudes of the fundamental frequency and second harmonic at increased excitation voltages and for different load values. Region between the dashed lines represents the cracked area.

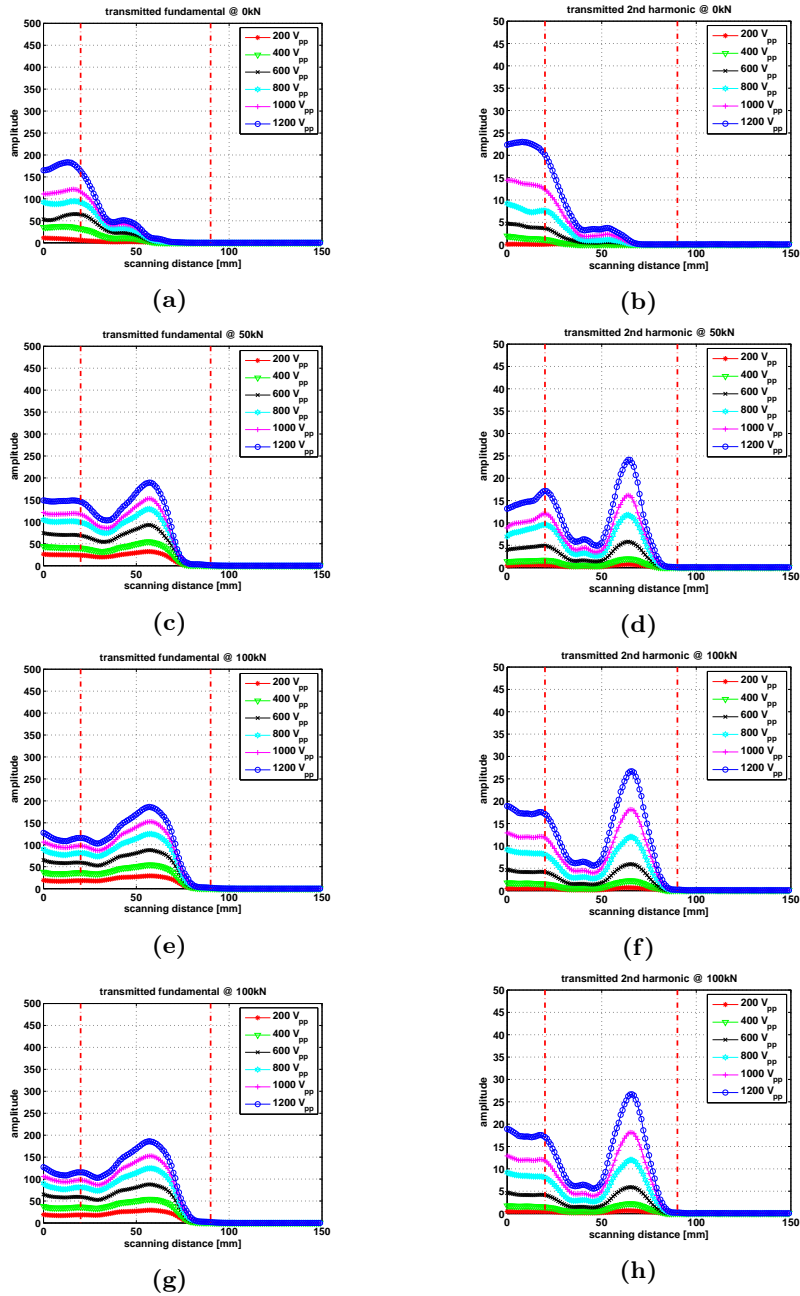


Figure 4.31: Transmitted magnitudes of the fundamental frequency and second harmonic at increased input voltages and for different load values. Region between the dashed lines represents the cracked area.

4.3 Comparison with theoretical formulation

In this section, an overall comparison between the proposed theoretical formulation and the experimental observations will be made in terms of crack transparency as well as harmonic generation and detection. As outlined in section 4.2, the crack was initiated through fatiguing at a distance of 100 mm from the probe scanning surface. It was shown that the material displacement, at this distance from the probe, is in the order of 6 nm for an excitation voltage of 200 Vpp, and in the order of 40 nm for an excitation voltage of 1200 Vpp. Based on this range of values, realistic excitation amplitudes were utilized in the mass-spring lattice scheme. To reduce the time required for computation, a small grid model of size 50 mm x 40 mm was chosen, in which the crack was positioned at 20 mm from the excitation source. Consequently, at such a short distance, lower input amplitudes ranging from 1 nm to 4 nm were sufficient to generate harmonics at a simulated closed crack. Although realistic excitation amplitudes were used in the mass-spring lattice scheme, a detailed comparison between modeling and experiments remains difficult. Nevertheless, features and crack behavior seen in the experiments were successfully simulated using the proposed scheme.

4.3.1 Crack closure

It has been confirmed that by increasing the compressive load, both the artificial interface and the fatigue crack interface become acoustically transparent to incident waves (Figures 4.7 and 4.15). Obviously, the crack closure was influenced by applying the load. This was monitored by means of reflection and transmission channels at either side of the crack interface. This crack behavior was simulated by applying the dynamic elasticity model derived in Chapter 2 to a cracked cell element in the mass-spring lattice scheme allowing for a real-time update of the effective stiffness as the crack opens and closes. It was clear that at a given crack opening in relation to a certain excitation amplitude, acoustical transparency occurs, at which reflection approaches its minimum and the transmission amplitude reaches its maximum (Figure 3.2).

4.3.2 Harmonic generation

When a crack is partially or fully closed, and depending on the contact area between crack asperities, harmonics may be generated when appropriate excitation amplitudes are applied. Apart from the input frequency, the strength of harmonics depends on the relationship between the crack opening and the applied excitation voltage. Figures 4.32 and 4.33 visualize this effect for both the simulated and the real case, in reflection mode. It should be noticed that a change in applied load means a change in contact area between crack asperities and, hence, the realization of a new crack shape. In this example, we are dealing with two different crack shapes, because the fatigue crack is loaded at two different values: 20 kN and 50 kN. Clearly, the crack shape realized at 50 kN shows a significant amplitude variation of the fundamental and second harmonic between traces 70 and 80 compared to the crack realized at 20 kN. The same observation can be made for the simulated case between traces 15 and 25 when changing the crack opening from $\delta_o = 10 z_o - 5 z_o - 15 z_o$ to $\delta_o = 10 z_o - 5 z_o - 10 z_o$. The two examples show a comparable behavior of the partially closed crack in terms of harmonic generation and amplitude variations of the fundamental and second harmonic.

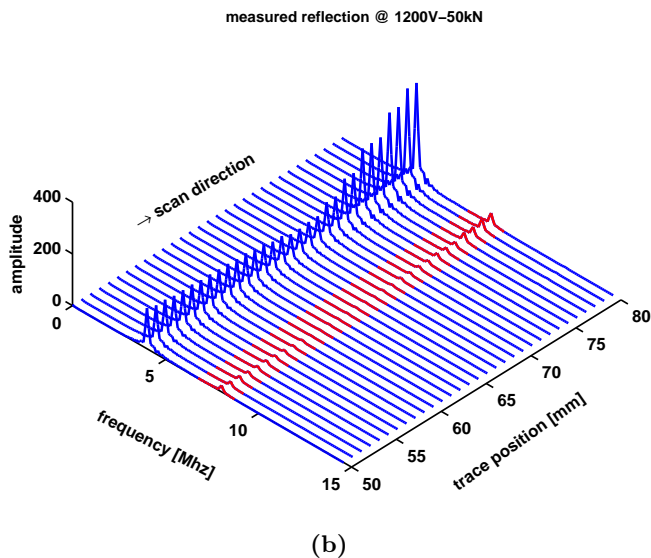
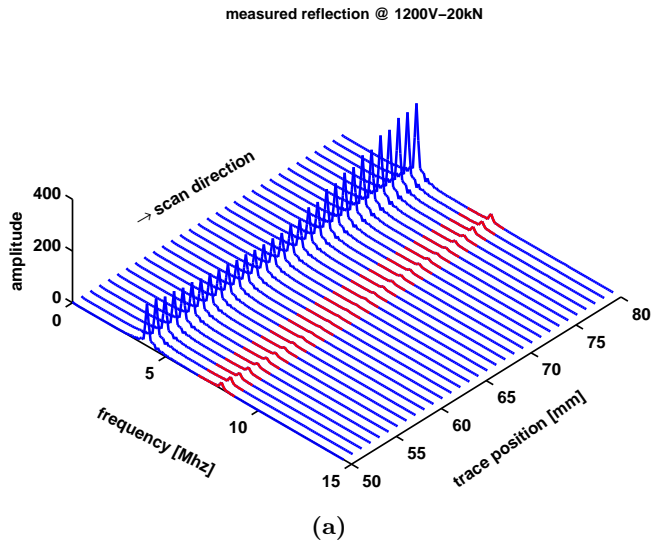
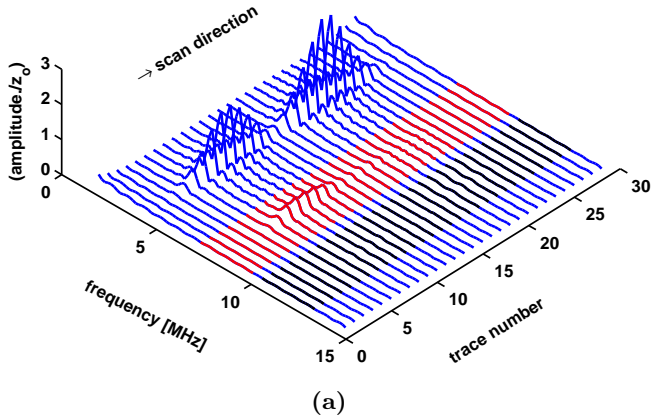


Figure 4.32: Frequency spectra of the reflected waveforms collected between positions $x = 50$ mm and $x = 80$ mm at 1200 V_{pp} for 20 kN (a) and 50 kN (b) load.

simulated reflection @ $a_z = 15 z_o, \delta_o = 10 z_o \rightarrow 5 z_o \rightarrow 15 z_o$



simulated reflection @ $a_z = 15 z_o, \delta_o = 10 z_o \rightarrow 5 z_o \rightarrow 10 z_o$

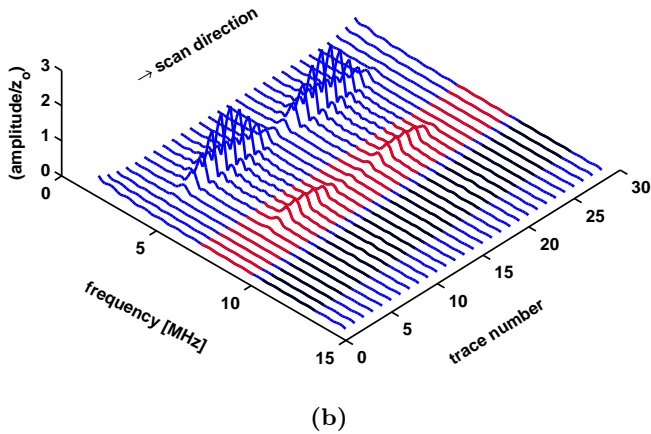


Figure 4.33: Frequency spectra of the reflected waveforms collected between positions $x = 10 \text{ mm}$ and $x = 30 \text{ mm}$ at the excitation amplitude $a_z = 20 z_o$ with 10 cycles for a crack shape opening $\delta_o = 10 z_o - 5 z_o - 15 z_o$ (a) and $\delta_o = 10 z_o - 5 z_o - 10 z_o$ (b).

To theoretically reproduce and quantify the crack response as observed in the experiments of Figure 4.30, the initial crack response can be updated and forward modeled by changing the initial crack opening with respect to the excitation amplitude. The resulted response is then compared to the real crack response, and the differences are used to update the crack opening again in an iterative way until the simulated crack response closely matches the real crack response. This way of updating and comparing the two data sets describes an inversion process. By using this approach, it is expected to get more insight in crack behavior, leading to an enhanced detection and sizing of closed cracks. A major drawback of this approach is the computational time required for updating and comparing the simulated and the real data.

Before applying the above mentioned procedure, a direct calibration of the excitation voltage to an excitation amplitude in the mass-spring lattice scheme, is required. Using displacement measurements presented in Section 3.1, a calibration simulation has been performed, in which the displacement at the crack location (100 mm) was monitored by changing the excitation amplitude until the same displacement value as measured by the laser vibrometer was obtained. For instance, a 200 Vpp excitation voltage corresponds to 12 nm excitation amplitude in the mass-spring lattice scheme. This calibration procedure is a good way of linking the excitation voltages to displacement amplitudes in the mass-spring lattice scheme. Due to the extensive computational time required for modeling a crack at large distances, results from the crack response at 25 mm outlined in Section 3.2 were re-used and updated for a crack location of 100 mm by single amplitude checks along three different crack positions.

To illustrate this approach by an example, the amplitude responses of the crack realized at 20 kN for three different excitation voltages (200 Vpp, 400 Vpp and 600 Vpp) were selected and used as input for the update procedure. In this case, an initial crack response was generated by a guessed crack shape, and subsequently updated and compared, after one iteration, to the measured crack response. Magnitudes of the reflected fundamental and second harmonic resulted from this step are displayed side by side in Figure 4.34 for both the simulated and the real crack. For both cases, it can be seen that the amplitude evolution and the range of magnitudes for both frequencies exhibit a comparable amplitude response showing two maxima and a minimum value along the crack length. This example shows a good agreement between the experimental and the numerical results, allowing for a reliable interpretation and comparison between the data.

Despite the good agreement achieved in this example, some differences are still present, when looking at the shape of the amplitude curves and comparing the strength of the reflected fundamental and second harmonic in the simulated and real case. The differences shown here, are not unexpected and can be explained by some numerical and measurements issues. First, the mass-spring lattice scheme developed for this purpose is a two-dimensional model and the excitation source embedded in the scheme is a line source, whereas the probe used in the experiments has a square shape. Second, a full computation of the crack response at 100 mm is required at all crack positions as performed in the case of crack location 25 mm. Third, more iterations are required for a better guess of the crack parameters in relation to the applied excitation amplitudes.

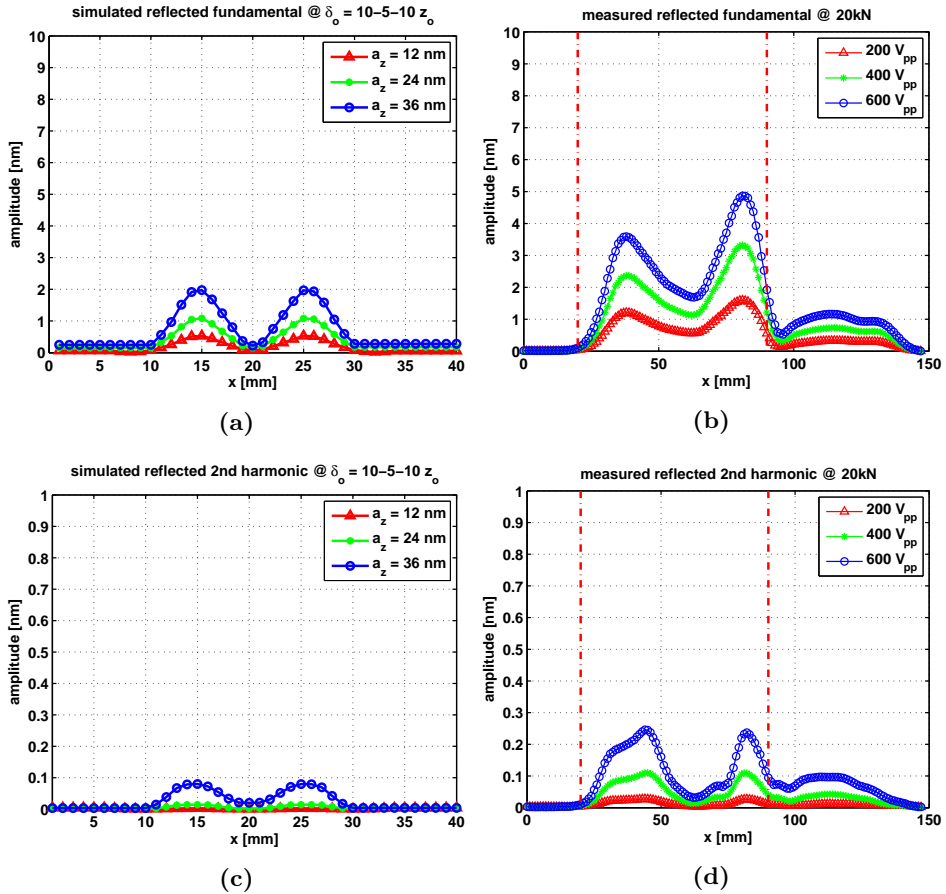


Figure 4.34: Simulated and measured magnitudes of the reflected fundamental and second harmonic of a partially closed crack at various excitation amplitudes: simulated crack with successive openings $10 z_o, 5 z_o, 10 z_o$ (a,c), and a real fatigue crack at 20 kN (b,d). 200 V_{pp} corresponds to 12 nm in the mass-spring lattice scheme. It should be emphasized that crack positions in both cases are different, since the crack length is not the same.

It should be emphasized that the approach presented here is a powerful method for modeling of the crack response, and it is expected to give new insights in the crack behavior and to enhance detection and sizing of closed cracks. As mentioned before, this approach is very expensive in terms of computational time and requires large scale parallel computing and the use an efficient scheme for updating and comparing the modeled and the measured data.

Chapter 5

Conclusions and recommendations

In this thesis, crack closure and harmonic generation have been demonstrated theoretically and experimentally. A dedicated mass-spring lattice model has been developed in which the elasticity of a partially or fully closed crack is dynamically computed and updated according to the opening and closing of the cracked cell element. Relevant features of a crack response observed in the experiments were also simulated with the developed algorithm. In this chapter, conclusions on crack closure and harmonic generation are presented. Furthermore, recommendations on steps towards acoustical imaging using harmonic generation are made.

5.1 Conclusions

Fatigue cracks showing an acoustically transparent behavior belong to a challenging category of defects. A good understanding of the crack closure phenomenon is required to develop appropriate algorithms that explain the observed effects theoretically. We successfully modeled the crack closure and harmonic generation by implementing a dynamic elasticity model, derived from the van der Waals interaction forces, into the mass-spring lattice model. A good agreement has been achieved between the theoretical predictions and the performed experiments, in terms of crack closure, harmonic generation and detection of such cracks.

In the experiments, crack closure was achieved by applying a compressive load on two steel blocks simulating an artificial crack interface, as well as on a real fatigue crack. By varying the load, we have seen that crack asperities might be realigned introducing different contact areas at different load values. This effect has clearly been verified by measuring reflection and transmission when fixing the excitation voltage and varying the load. The severity of acoustical transparency was measured by comparing magnitudes of reflection and transmission waves through the crack interface. Furthermore, it was confirmed that the detection of closed cracks can be improved by increasing the excita-

tion amplitude.

When dealing with high excitation amplitudes, precautionary measures should be taken in order to perform reliable measurements on harmonic generation. As verified in Chapter 4, harmonics may arise from the acquisition system. These harmonics can be reduced by using well-designed high voltage probes, signal attenuators, signal amplification, etc... For analysis purposes, data related to uncracked regions can be used as a reference and compared to the data collected from a real crack.

The non-linear nature of crack motion observed in the experiments has been confirmed by the dynamic elasticity model. Harmonics were observed in both reflection and transmission modes. Depending on the extension and contraction of the cracked cell element, and due to the variations in the effective spring stiffness, harmonics are generated. It has also been shown that the input frequency and the ratio between crack opening and the strength of the excitation source are essential parameters for achieving crack closure and harmonic generation.

Information gained from harmonic generation is very valuable for the detection of closed cracks. Furthermore, combining fundamental and second harmonic data is a key element to enhance detection and sizing of closed cracks. This is the first step towards harmonic imaging, by which closed cracks can be imaged using second harmonic generation.

5.2 Recommendations

This research topic was initiated to tackle the issue of acoustical transparency of fatigue cracks, since the existing technology does not meet the inspection requirements dictated by the industry. From this perspective, feedback from NDT experts and industrial partners was continuously considered throughout the experiments performed during this research period. Findings and results related to this research topic are intended to be implemented in the near future to serve NDT with new technology enhancing detection and sizing of such cracks.

All the results presented in this thesis on harmonic generation are produced with two compressional dual frequency probes placed on either side of the crack interface. This probe configuration allows for a direct insonification of the crack resulting in reflection and transmission when a load is applied. Beside the compressional mode, shear waves measurements in pitch-catch configuration were performed. However, these measurements were limited to a fixed crack position due to the available space to move the associated probe arrangement along the fatigued specimen. This shortcoming was the reason for omitting the results in this thesis. For this purpose, a dedicated scanning mechanism for shear wave probes is required.

For our experiments, dedicated high power excitation probes were designed. However, to efficiently increase the corresponding energy output, material composition and crystal backing of the transmitting element should be investigated. Furthermore, various frequencies can be generated and tested. A potential alternative is to design a probe with a sweep frequency functionality, supporting excitation with high amplitudes. It is

expected that by sweeping with a range of frequencies, more valuable data on the crack response can be gathered and, hence, detection and sizing of acoustically transparent cracks can be improved.

Further investigations on harmonic generation can be made by performing indirect insonification of the crack exploiting the tandem approach. In this configuration, ultrasonic waves will be reflected and/or diffracted by the crack following a different sound path back to the receiver or vice versa. Direct and indirect insonification including all combinations of wave modes will give more insight into crack response and behavior with regard to ultrasonic waves. For comparison purposes, the experiments can be complemented by implementing the tandem configuration into the mass-spring lattice model.

In Chapter 4, we demonstrated that harmonics may arise from the acquisition system and, therefore, misleading in the interpretation of the results. It is hard to fully avoid generation of these high frequency components when high voltages are applied. However, using dedicated signal attenuators and well-designed filters may reduce these harmonics significantly. It is recommended that prior to experiments, a power spectrum signature of the acquisition system can be generated and then used as a reference when inspecting closed cracks.

Since harmonic components are present in the data related to a closed crack, imaging of such a crack may become feasible when exploiting second harmonic generation. As explained in Chapter 1, imaging techniques, such as IWEX, require an ultrasonic array consisting of small piezoelectric elements used as sources and receivers by firing each element and receiving with all elements sequentially. However, from a hardware perspective, the existing ultrasonic arrays and the acquisition systems are not yet well-developed for harmonic experiments. In order to apply harmonic imaging using the IWEX algorithm, a three-step approach can be followed. The first step would be to use a conventional probe as a high voltage source with frequency f moving along different scan positions and a receiving ultrasonic array of frequency $2f$ gathering the attenuated reflected and diffracted data. As soon as array technology and hardware advances for high voltage excitation have been realized, a step to two array probes can be made, where one array with frequency f is used as source and the other one with frequency $2f$ as receiver. The ultimate step would be to have a dual frequency array probe setup (in one housing or two array close to each other) handling two different frequencies and supporting high voltage excitation, simultaneously. This will allow us to use the IWEX approach as described in Pörtzgen (2007).

The proposed mass-spring lattice model scheme with incorporated van der Waals interaction, revealed essential features observed in the experiments on crack closure and harmonic generation. Further improvements of this algorithm are foreseen. For now, the dynamic elasticity is applied along the z-direction only. Considering the influence of crack opening and closing outside the vertical direction, a dynamic update of the elasticity of the diagonal stiffness k_2 and the rotational stiffness αk_2 might be required as in the case of the vertical stiffness k_3 . By adopting this approach, non-perpendicular incidence for both shear and compressional waves can be modeled as well. Furthermore, testing of different input amplitudes, frequencies, and number of signal cycles in combi-

nation with crack openings is recommended.

In practical circumstances, beside acoustical transparency, the shape and morphology of the crack are unknown. This fact limits the direct interpretability of the measured data. Using an iterative scheme based on the principle of inversion will allow for matching the simulated crack response to the real crack response, leading to a better understanding of crack behavior and, therefore, a better detection and sizing of such cracks. For complex crack shapes, e.g., branched closed cracks, full inversion may be required, which constitutes the ultimate step in imaging algorithms.

The research topic outlined in this thesis was limited to higher harmonics ($2f$) only. Nevertheless, investigation of possible subharmonic generation ($f/2$) at closed cracks is an interesting extension to investigate further improvements of the detection and sizing of acoustically transparent cracks. The same experiments followed for second harmonic generation can be repeated for the subharmonic case. Previous recommendations made for harmonic imaging with IWEX can be applied to the subharmonic case as well.

Non-linear acoustics and especially second harmonic imaging is a promising technique for NDT applications. Although the current hardware implementation is not very advanced yet, the upcoming imaging techniques such as IWEX rely on more advanced acquisition electronics and data handling, which will present new opportunities to meet the new imaging requirements. Another issue that remains and will play a role in the future is the acceptance of non-linear imaging technologies by the industry and by the codes and standards bodies regulating the application of new technologies in the world on nondestructive testing.

Appendix A

Symbols and abbreviations

A.1 Symbols

The following symbols and abbreviations are used throughout the thesis.

symbol	description
a	interatomic distance
a_z	input amplitude
dV	element volume
f	frequency
h	grid spacing
i	grid point location i
j	grid point at location j
k_1	spring constant
k_2	spring constant
k_3	spring constant
k_{crack}^t	crack spring elasticity at time t
k_{crack}^{t-1}	crack spring elasticity at time $t - 1$
k_{crack}	crack spring elasticity
$k_{dynamic}$	dynamic spring elasticity of cracked cell element
n	number of atoms per unit volume
r	separation distance
z_0	equilibrium distance
z	separation distance
u	displacement in x-direction
$u_{i,j}^k$	particle displacement in x -direction at point (i,j) and time $k\Delta t$
v	displacement in z -direction

$v_{i,j}^k$	particle displacement in z -direction at point (i,j) and time $k\Delta t$
A	Hammaker constant
A_1	amplitude fundamental
A_2	amplitude second harmonic
C	London constant
F_{MP}	interaction force between a molecule and half-space
F_{PP}	interaction force between two half-spaces
C_i	compressional probe, $i = 1, 2$
H	height steel block
L	length steel block
S_i	shear wave probe, $i = 1, 2$
U	Lennard-Jones potential
U_0	minimum potential energy
V_{pp}	peak-to-peak voltage
W	width steel block
Δt	time step
αk_2	rotational spring constant
β	spring constant
δ_o	initial crack opening
δ^{t_0}	crack opening displacement at time $t = 0$
δ^{t_1}	crack opening displacement at time $t = \Delta t$
δ^t	crack opening displacement at time t
δ^{t-1}	crack opening displacement at time $t - 1$
δ	crack opening
λ	Lamé constant
μ	Lamé constant
σ	van der Waals stress
ρ	mass density

A.2 Abbreviations

symbol	description
AFM	atomic force microscopy
AUT	automated ultrasonic testing
AWG	arbitrary wave generator
BEM	boundary element method
CAN	contact acoustic non-linearity
DIC	digital image correlation
DDN	dumped double node

DMT	Derjaguin, Muller, Toporov
FD	finite difference
FEM	finite element method
MSLM	mass-spring lattice model
N	number of array elements
NDT	nondestructive testing
IWEX	inverse wave field extrapolation
JKR	Johnson, Kendall and Robert
R	receiver
ROI	region of interest
RT	radiographic testing
PA	phased array
PE	pulse echo
SAFT	synthetic aperture focussing technique
SCR	steel catenary riser
SPA	sampling phased array
T	transmitter
T/R	transmitter/receiver
TFM	total focusing method
ToFD	time of flight diffraction
UT	ultrasonic testing

Appendix B

Derivation of van der Waals stress

To derive the the attraction force and the van der Waals stress interaction between two-half spaces separated by a distance z , Let us first compute the Lennard-Jones force by derivation of the Lennard-Jonnes potential given in equation 2.1:

$$F(r) = 4U_o \left[-12 \left(\frac{a^{12}}{r^{13}} \right) + 6 \left(\frac{a^6}{r^7} \right) \right]. \quad (\text{B.1})$$

Following the same calculation steps as outlined in Maugis (1999), the interaction force and the related stress between two half-spaces can be computed. First, let us derive the interaction force at a distance d between a molecule M and an infinite half-space having n atoms per unit volume (Figure B.1). The normal component of the Lennard-Jones force applied on M by a molecule P is:

$$F(r, \varphi) = 4U_o \left[-12 \left(\frac{a^{12}}{r^{13}} \right) + 6 \left(\frac{a^6}{r^7} \right) \right] \cos(\varphi). \quad (\text{B.2})$$

Substituting the distance r in equation (B.2) by $z/\cos(\varphi)$ yields:

$$F(z, \varphi) = 4U_o \left[-12 \left(\frac{a^{12} \cos^{14}(\varphi)}{z^{13}} \right) + 6 \left(\frac{a^6 \cos^8(\varphi)}{z^7} \right) \right]. \quad (\text{B.3})$$

The contribution from the element volume $dV = 2\pi z^2 \frac{\sin(\varphi)}{\cos^3(\varphi)} d\varphi dz$ is:

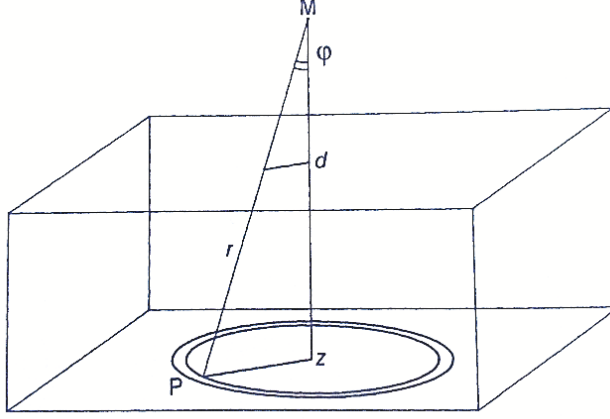


Figure B.1: Schematic of interaction between a molecule and half-space separated by a distance d (Maugis 1999).

$$F(z, \varphi)ndV = 4U_o \left[-12 \left(\frac{a^{12} \cos^{14}(\varphi)}{z^{13}} \right) + 6 \left(\frac{a^6 \cos^8(\varphi)}{z^7} \right) \right] \left(\frac{2\pi n z^2 \sin(\varphi)}{\cos^3(\varphi)} \right) d\varphi dz. \quad (\text{B.4})$$

$$F(z, \varphi)ndV = 8\pi n U_o \left[-12 \left(\frac{a^{12} \cos^{11}(\varphi)}{z^{11}} \right) + 6 \left(\frac{a^6 \cos^5(\varphi)}{z^5} \right) \right] \sin(\varphi) d\varphi dz. \quad (\text{B.5})$$

$$F(z, \varphi)ndV = \left[-96\pi n U_o a^{12} \left(\frac{dz}{z^{11}} \cos^{11}(\varphi) \sin(\varphi) d\varphi \right) + 48\pi n U_o a^6 \left(\frac{dz}{z^5} \cos^5(\varphi) \sin(\varphi) d\varphi \right) \right]. \quad (\text{B.6})$$

By integration, the interaction force between a molecule and a half-space is:

$$F_{MP}(d) = \left[-96\pi n U_o a^{12} \int_0^\infty \frac{dz}{z^{11}} dz \int_0^{\pi/2} \cos^{11}(\varphi) \sin(\varphi) d\varphi \right] + \left[48\pi n U_o a^6 \int_0^\infty \frac{dz}{z^5} dz \int_0^{\pi/2} \cos^5(\varphi) \sin(\varphi) d\varphi \right]. \quad (\text{B.7})$$

$$F_{MP}(d) = \left[\frac{-96\pi n U_o a^{12}}{110} \frac{1}{d^{10}} \right] + \left[\frac{48\pi n U_o a^6}{24} \frac{1}{d^4} \right]. \quad (\text{B.8})$$

Hence, the interaction force between two half-spaces separated by a distance d is:

$$F_{PP}(d) = \int_z^\infty \frac{-96\pi n U_o a^{12}}{110} \frac{1}{z^{10}} ndz + \int_z^\infty \frac{48\pi n U_o a^6}{24} \frac{1}{z^4} ndz. \quad (\text{B.9})$$

$$F_{PP}(d) = \frac{-96\pi n^2 U_o a^{12}}{110} \int_z^\infty \frac{1}{z^{10}} dz + \frac{48\pi n^2 U_o a^6}{24} \int_z^\infty \frac{1}{z^4} dz. \quad (\text{B.10})$$

$$F_{PP}(d) = \frac{-16\pi n^2 U_o a^{12}}{165} \frac{1}{d^9} + \frac{4\pi^2 n^2 U_o a^6}{6\pi} \frac{1}{d^3}. \quad (\text{B.11})$$

At separation distance z , equation B.11 can be rewritten as:

$$\sigma(z) = \frac{A}{6\pi z^3} - \frac{B}{z^9}, \quad (\text{B.12})$$

where $A = \pi^2 n^2 C$ is the Hamaker constant and C is the London constant (about 10^{-79} J m^6), and B can be deduced from $\sigma(z) = 0$ at the equilibrium distance z_o as:

$$\sigma(z) = \frac{A}{6\pi z_o^3} \left[\left(\frac{z_o}{z} \right)^3 - \left(\frac{z_o}{z} \right)^9 \right]. \quad (\text{B.13})$$

Appendix C

Magnitude of harmonics at various loads and fixed excitation voltages

C.1 Reflected harmonics

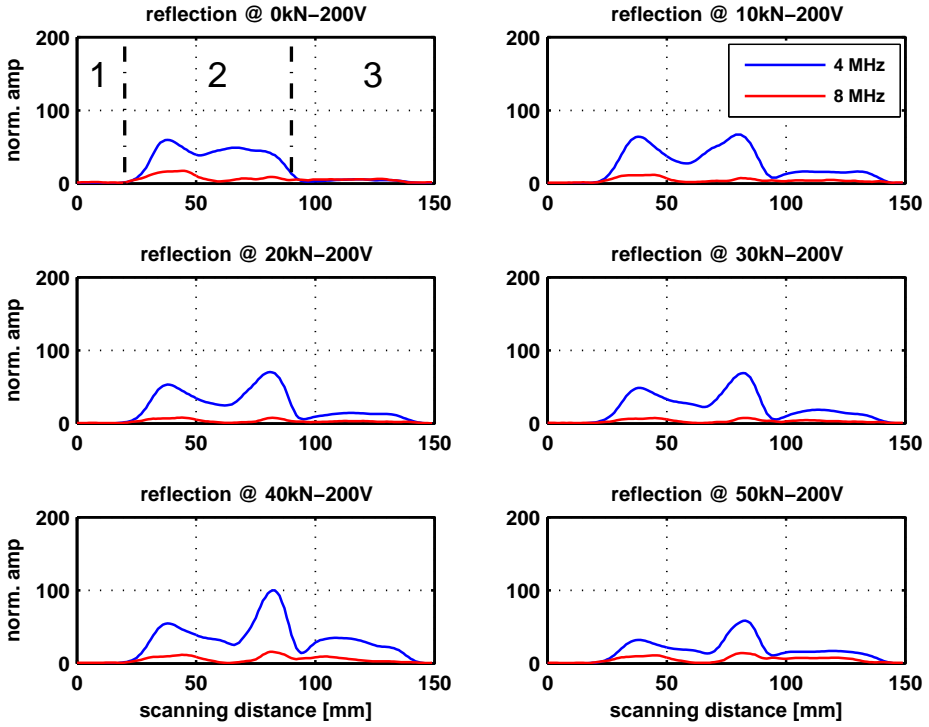


Figure C.1: Normalized amplitudes of reflected harmonics of different traces at 200 V_{pp} - 24 cycles against increased load. All magnitudes are normalized to the amplitude corresponding to the first trace of crack tip response (trace 20).

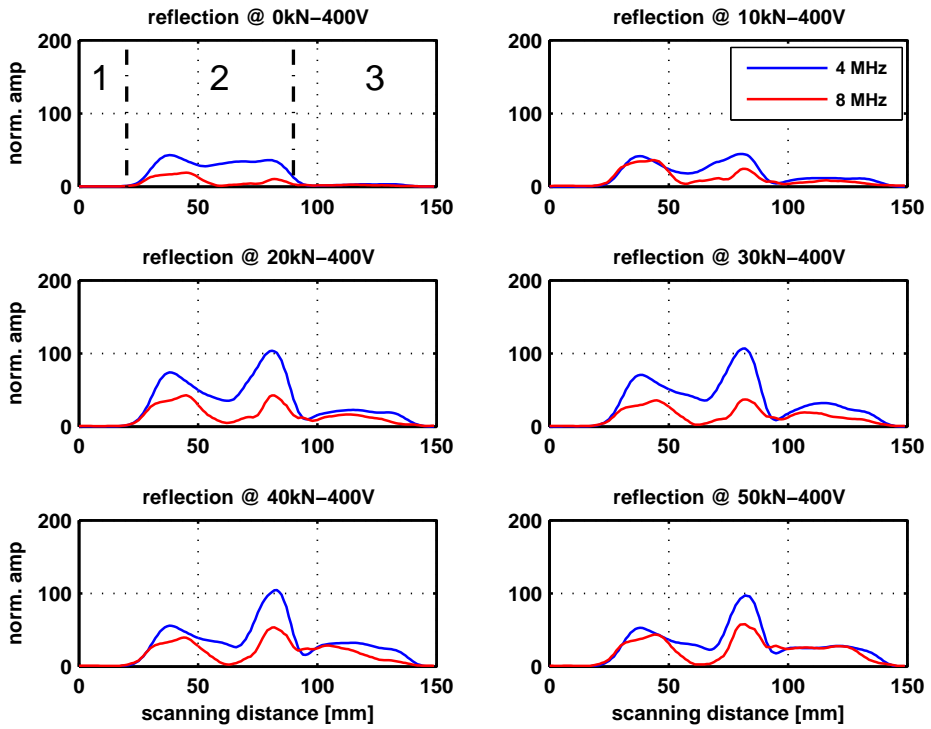


Figure C.2: Normalized amplitudes of reflected harmonics of different traces at 400 V_{pp} - 24 cycles against increased load. All magnitudes are normalized to the amplitude corresponding to the first trace of crack tip response (trace 20).

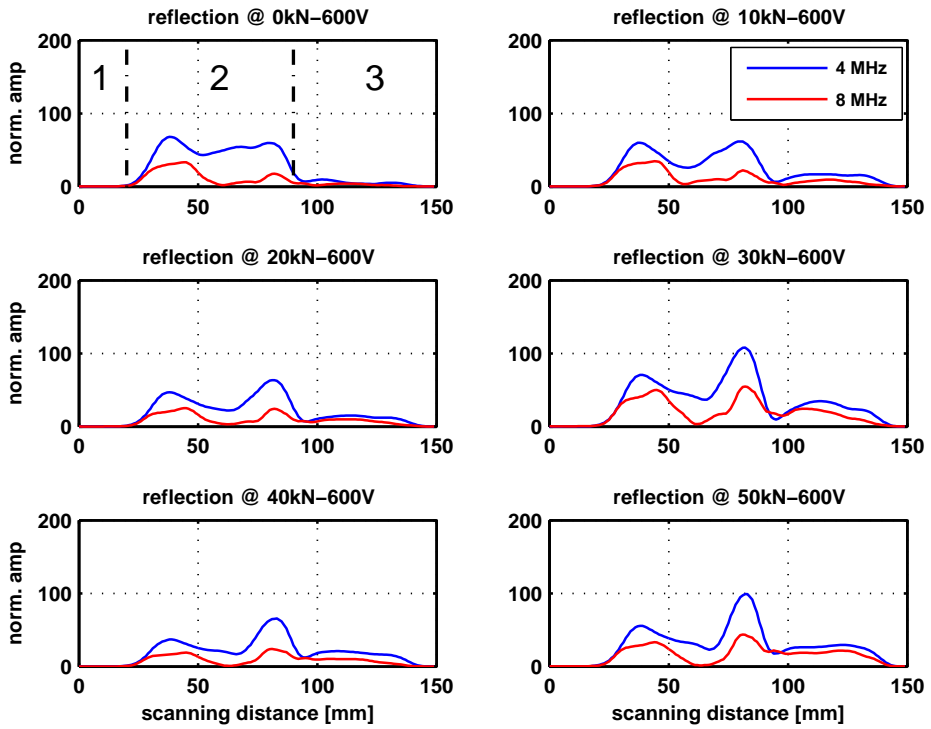


Figure C.3: Normalized amplitudes of reflected harmonics of different traces at 600 Vpp - 24 cycles against increased load. All magnitudes are normalized to the amplitude corresponding to the first trace of crack tip response (trace 20).

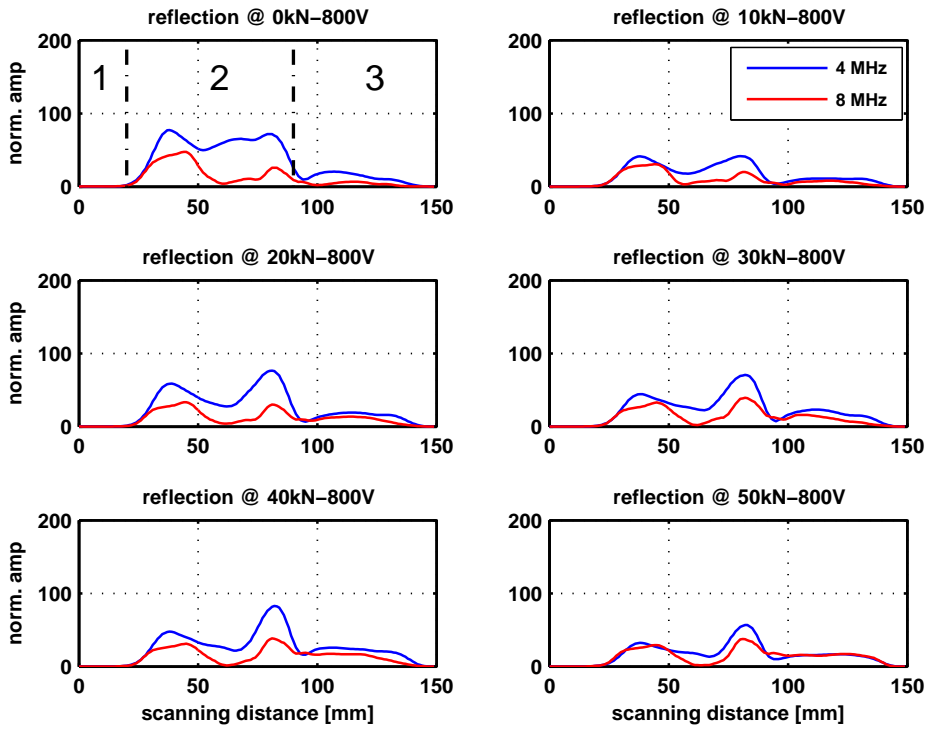


Figure C.4: Normalized amplitudes of reflected harmonics of different traces at 800 Vpp - 24 cycles against increased load. All magnitudes are normalized to the amplitude corresponding to the first trace of crack tip response (trace 20).

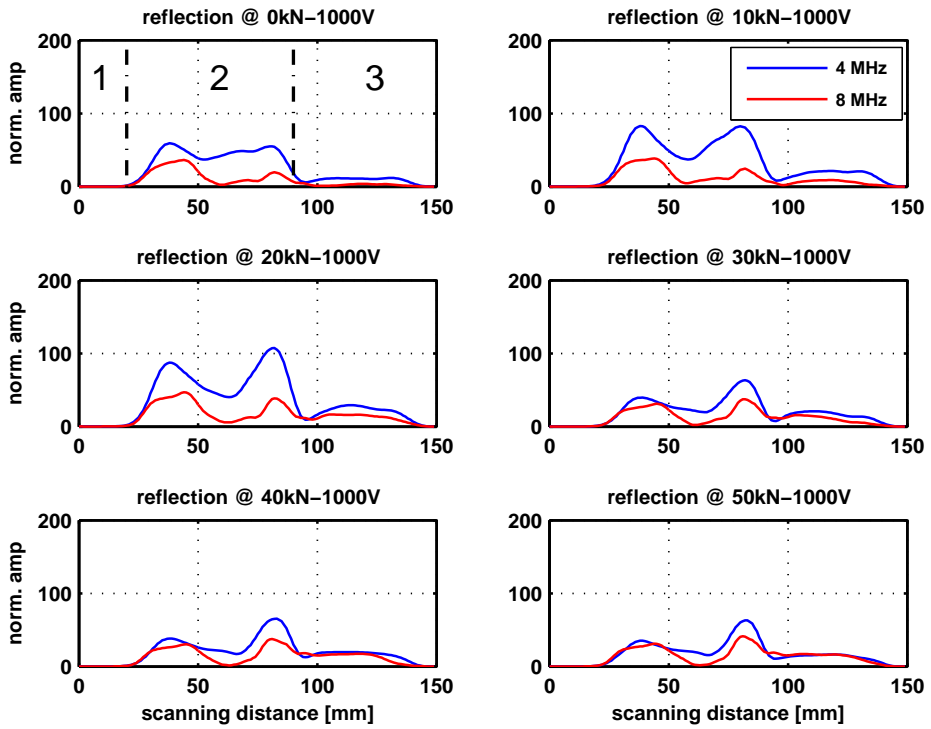


Figure C.5: Normalized amplitudes of reflected harmonics of different traces at 1000 Vpp - 24 cycles against increased load. All magnitudes are normalized to the amplitude corresponding to the first trace of crack tip response (trace 20).

C.2 Transmitted harmonics

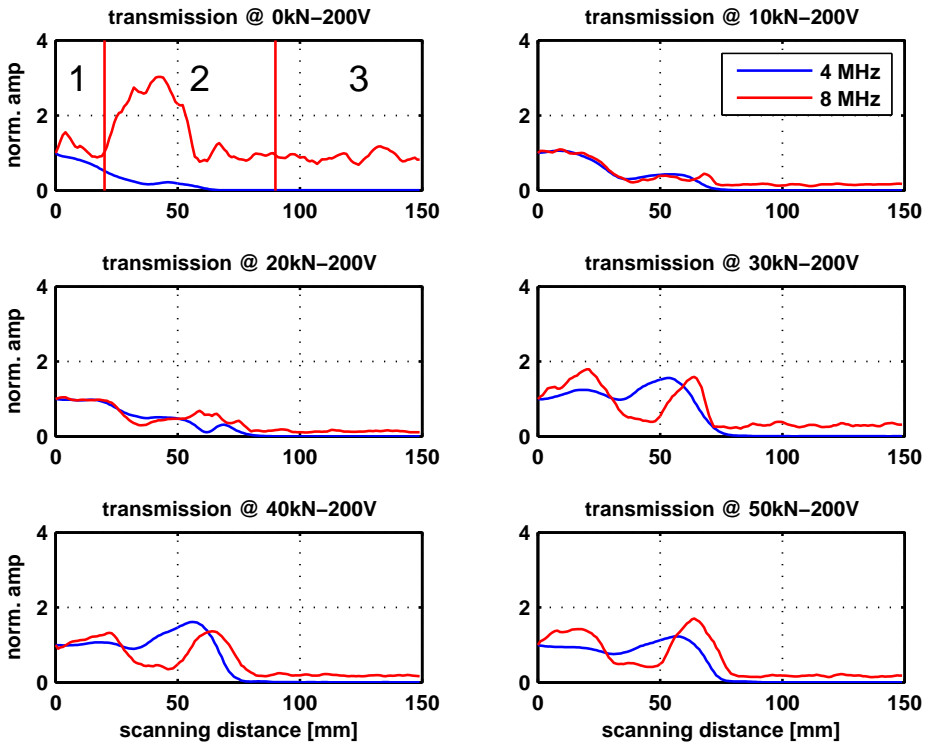


Figure C.6: Normalized magnitudes of transmitted harmonics of different traces at 200 V_{pp} - 24 cycles against increased load. All magnitudes are normalized to the amplitude corresponding to trace 1 regarded as a reference.

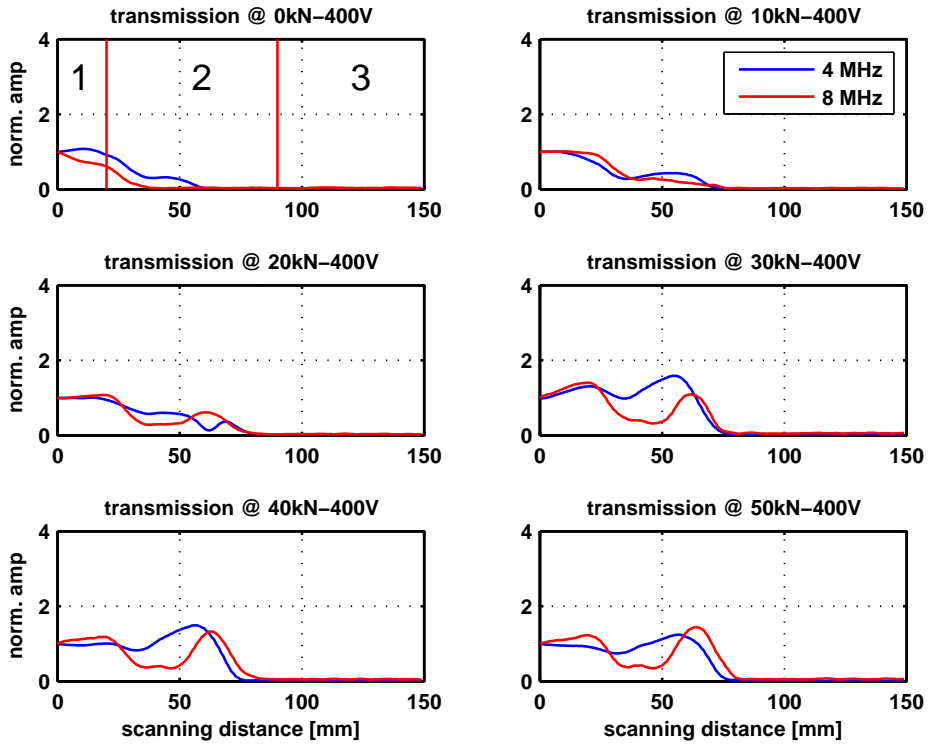


Figure C.7: Normalized magnitudes of transmitted harmonics of different traces at 400 V_{pp} - 24 cycles against increased load. All magnitudes are normalized to the amplitude corresponding to trace 1 regarded as a reference.

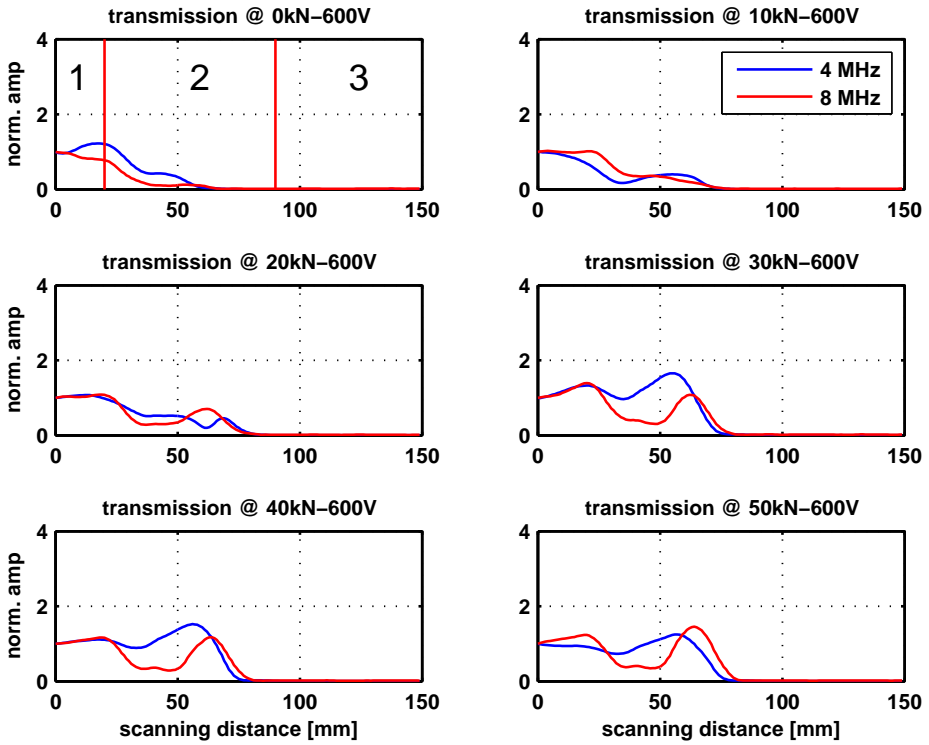


Figure C.8: Normalized magnitudes of transmitted harmonics of different traces at 600 V_{pp} - 24 cycles against increased load. All magnitudes are normalized to the amplitude corresponding to trace 1 regarded as a reference.

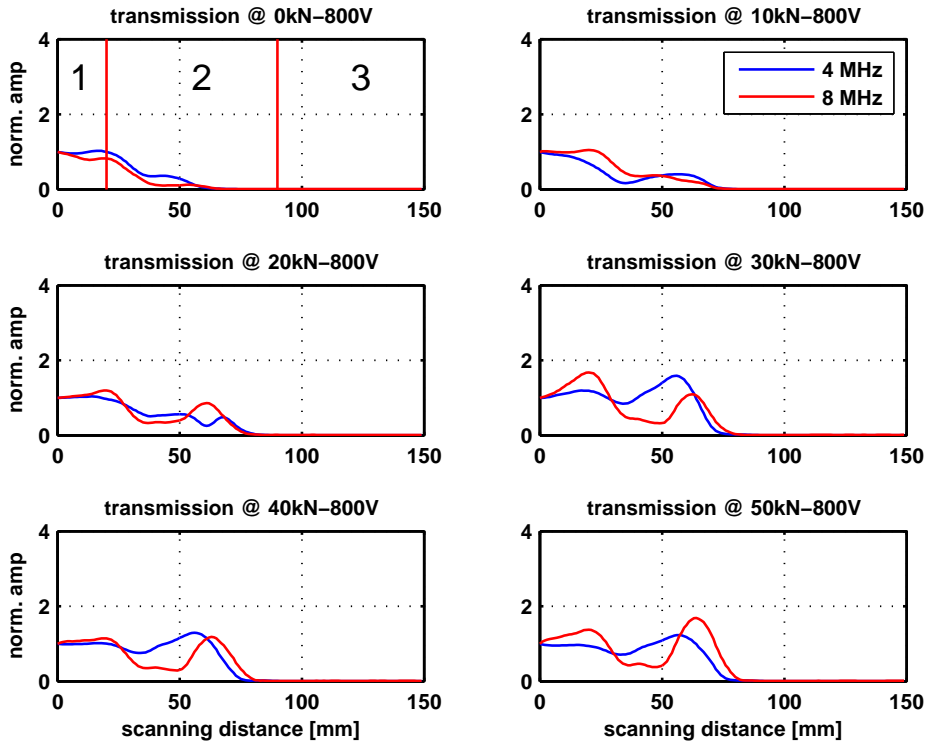


Figure C.9: Normalized magnitudes of transmitted harmonics of different traces at 800 V_{pp} - 24 cycles against increased load. All magnitudes are normalized to the amplitude corresponding to trace 1 regarded as a reference.

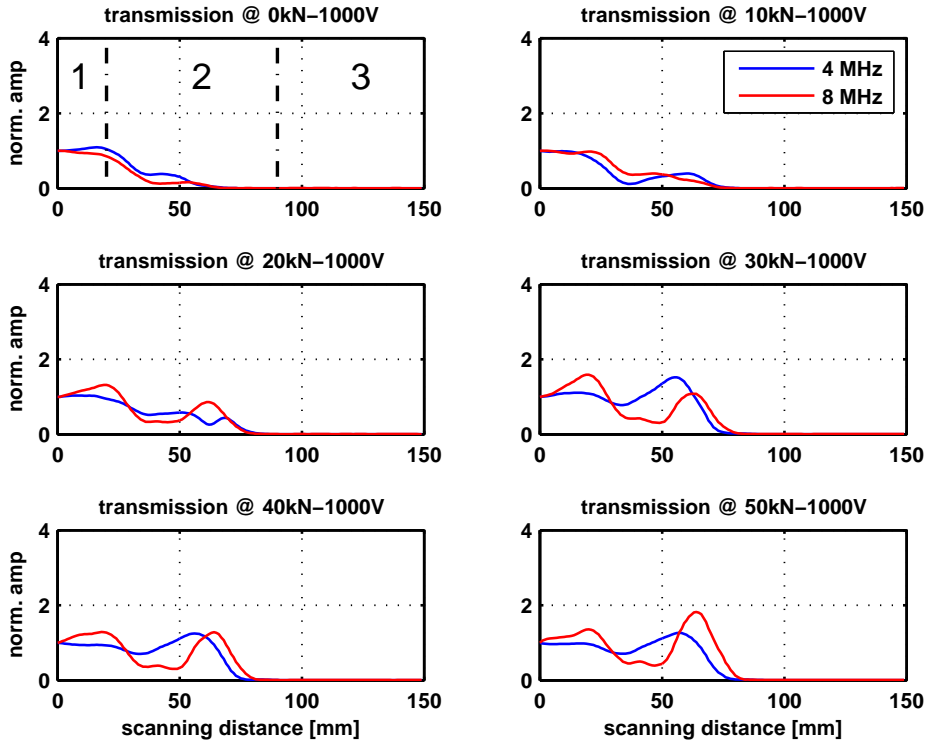
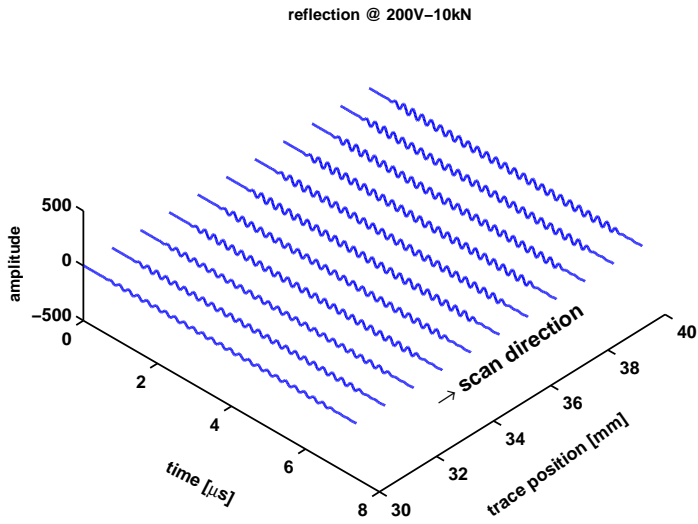


Figure C.10: Normalized magnitudes of transmitted harmonics of different traces at 1000 V_{pp} - 24 cycles against increased load. All magnitudes are normalized to the amplitude corresponding to trace 1 regarded as a reference.

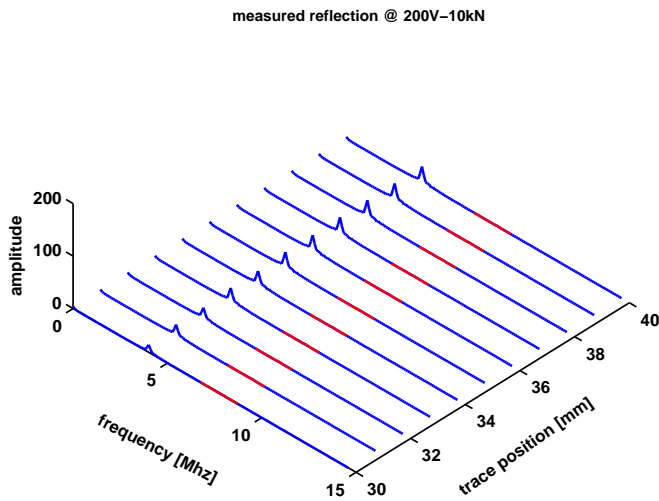
Appendix D

Power spectra at various
excitation voltages and a fixed
load

D.1 Reflection

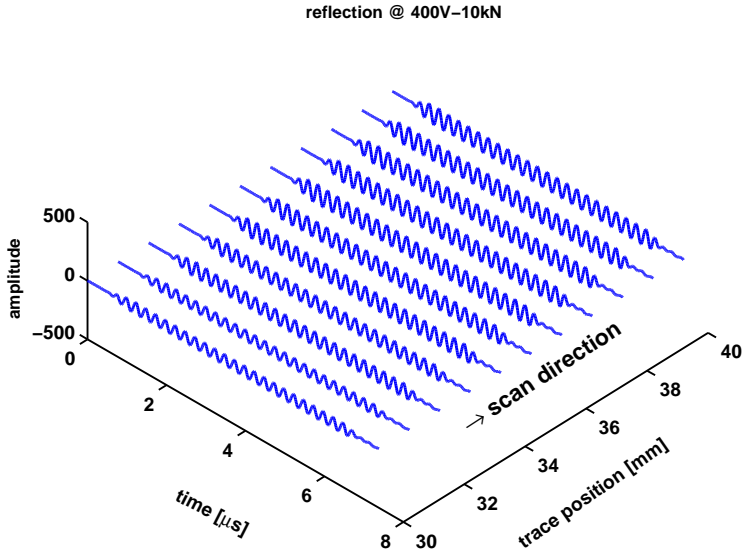


(a)

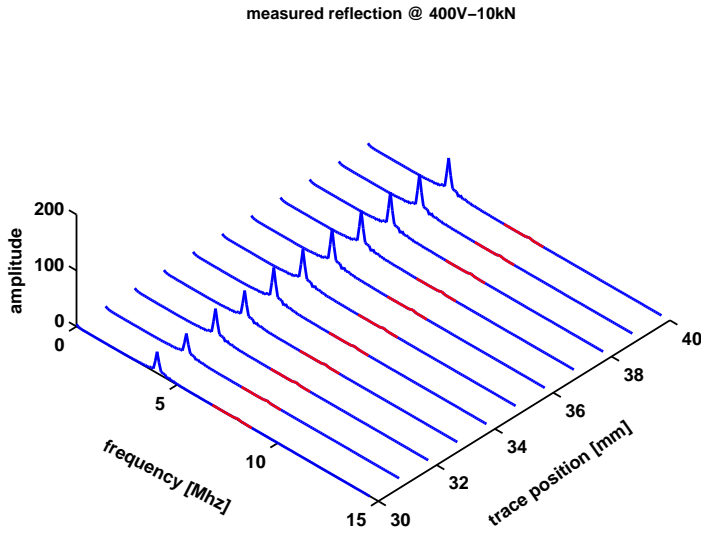


(b)

Figure D.1: Waveforms collected by the reflection channel C1 – C1 at 10 kN between traces 30 and 40 (a) with the related frequency spectrum (b) at 200 V_{pp} and 24 cycles.

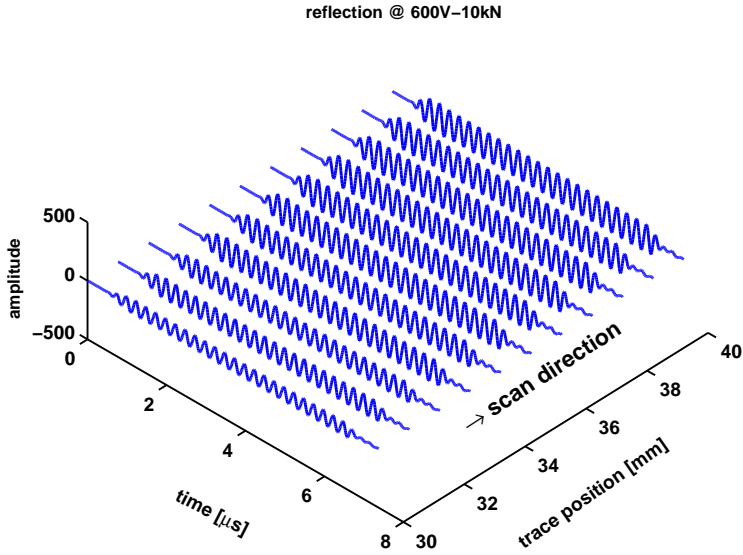


(a)

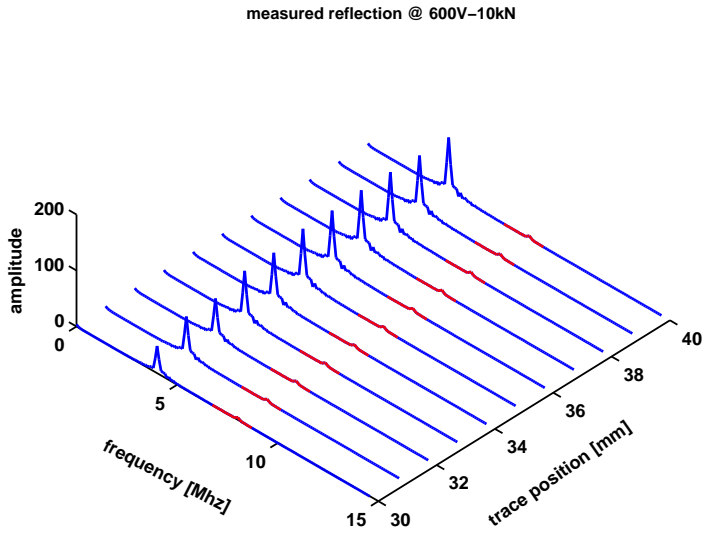


(b)

Figure D.2: Waveforms collected by the reflection channel C1 – C1 at 10 kN between traces 30 and 40 (a) with the related frequency spectrum (b) at 400 V_{pp} and 24 cycles.



(a)



(b)

Figure D.3: Waveforms collected by the reflection channel C1 – C1 at 10 kN between traces 30 and 40 (a) with the related frequency spectrum (b) at 600 V_{pp} and 24 cycles.

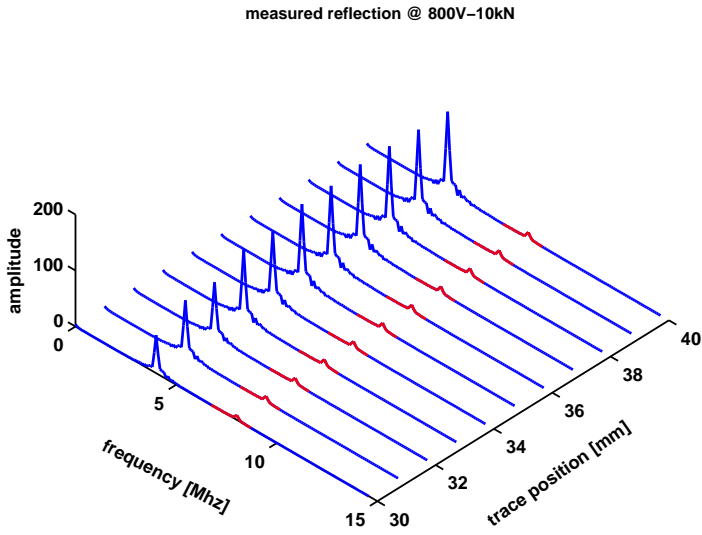
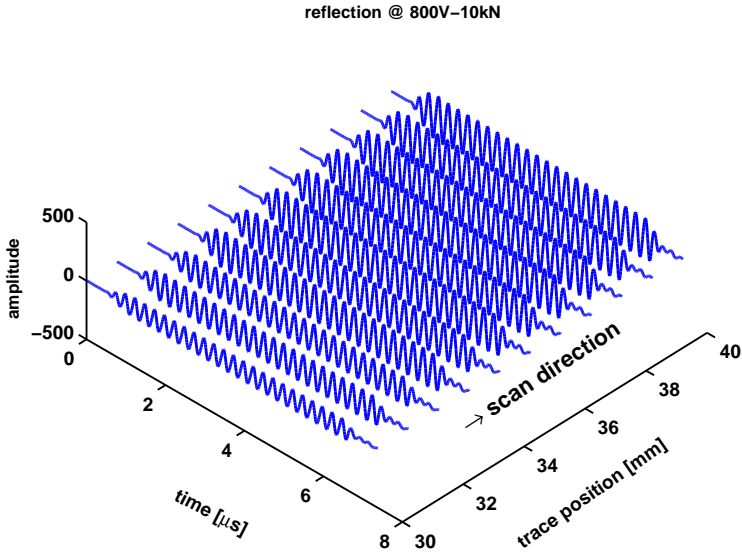
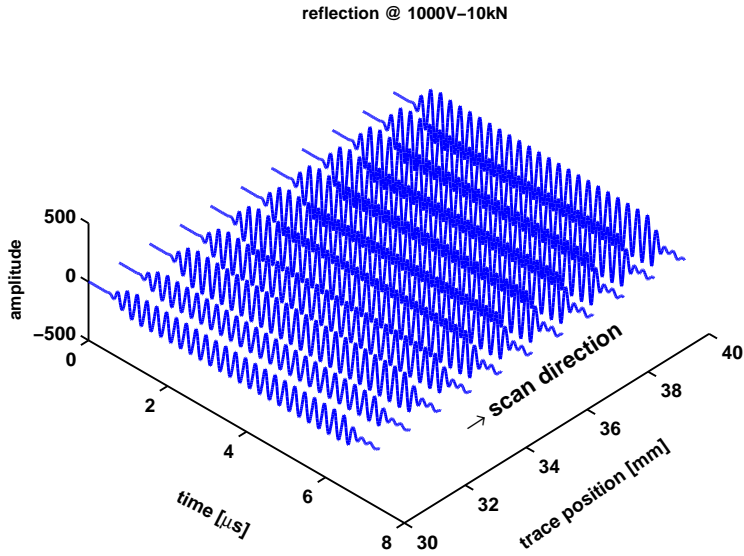
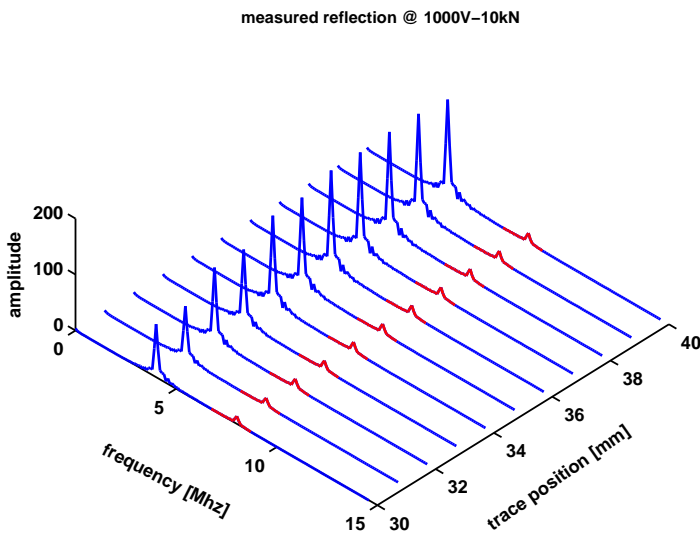


Figure D.4: Waveforms collected by the reflection channel C1 – C1 at 10 kN between traces 30 and 40 (a) with the related frequency spectrum (b) at 800 V_{pp} and 24 cycles.



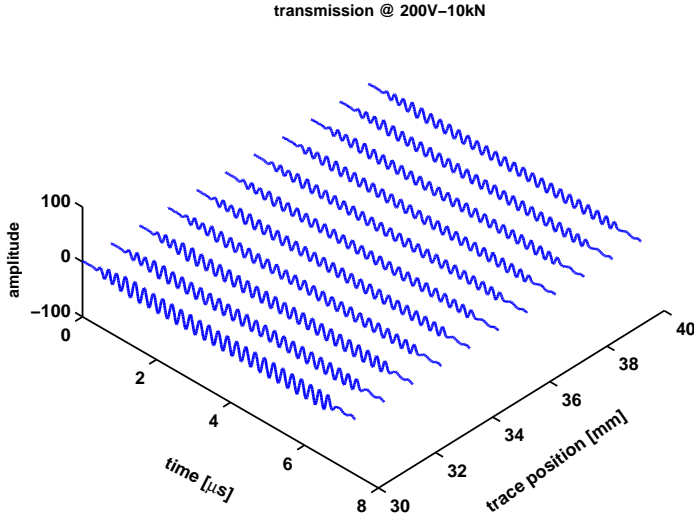
(a)



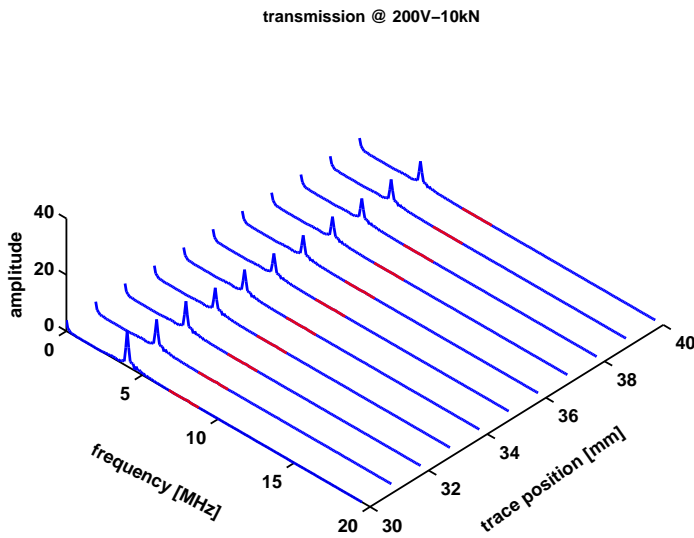
(b)

Figure D.5: Waveforms collected by the reflection channel C1 – C1 at 10 kN between traces 30 and 40 (a) with the related frequency spectrum (b) at 1000 V_{pp} and 24 cycles.

D.2 Transmission

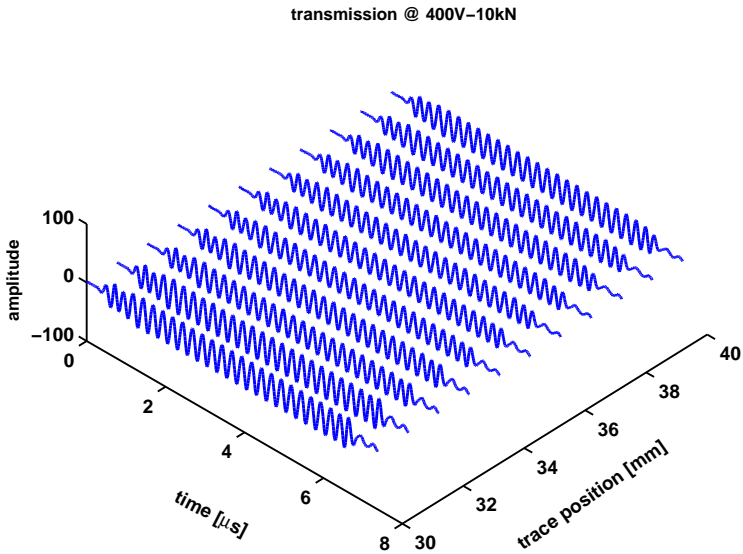


(a)

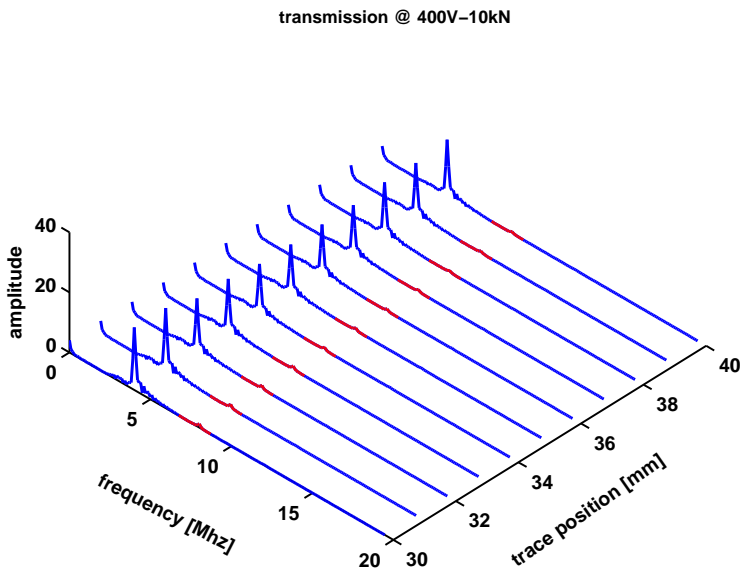


(b)

Figure D.6: Waveforms collected by the transmission channel C1–C2 at 10 kN between traces 30 and 40 (a) with the related frequency spectrum (b) at 200 V_{pp} and 24 cycles.

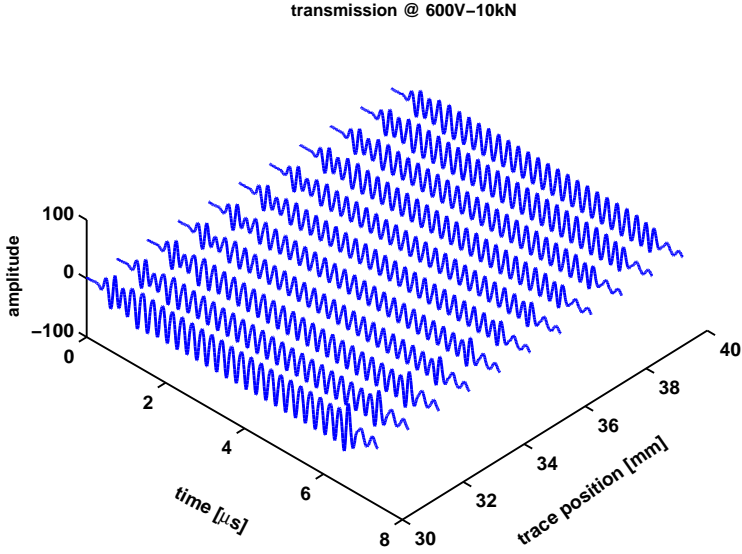


(a)

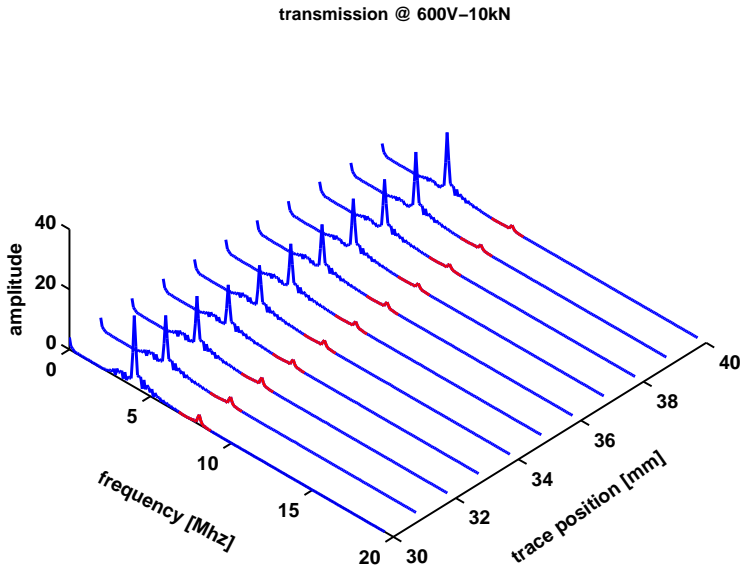


(b)

Figure D.7: Waveforms collected by the transmission channel C1–C2 at 10 kN between traces 30 and 40 (a) with the related frequency spectrum (b) at 400 V_{pp} and 24 cycles.

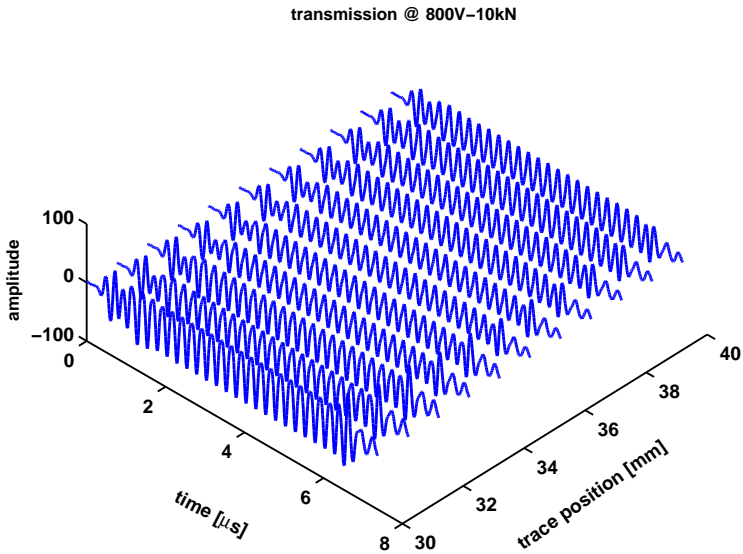


(a)

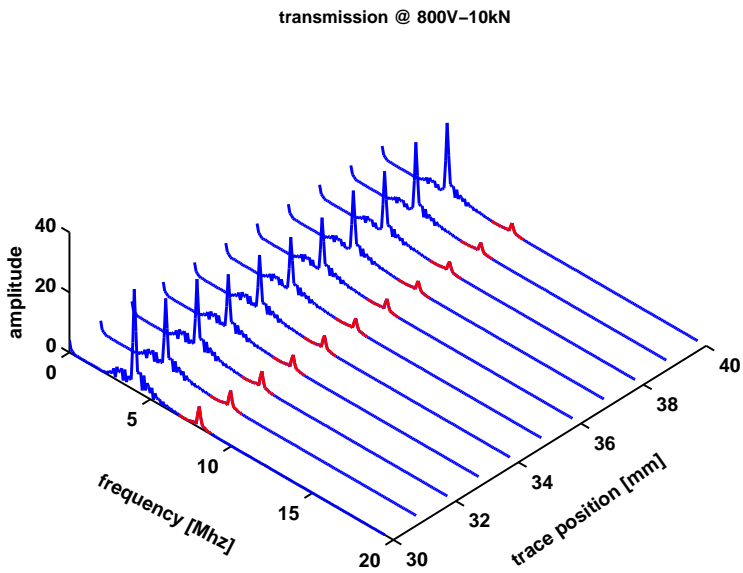


(b)

Figure D.8: Waveforms collected by the transmission channel C1–C2 at 10 kN between traces 30 and 40 (a) with the related frequency spectrum (b) at 600 V_{pp} and 24 cycles.

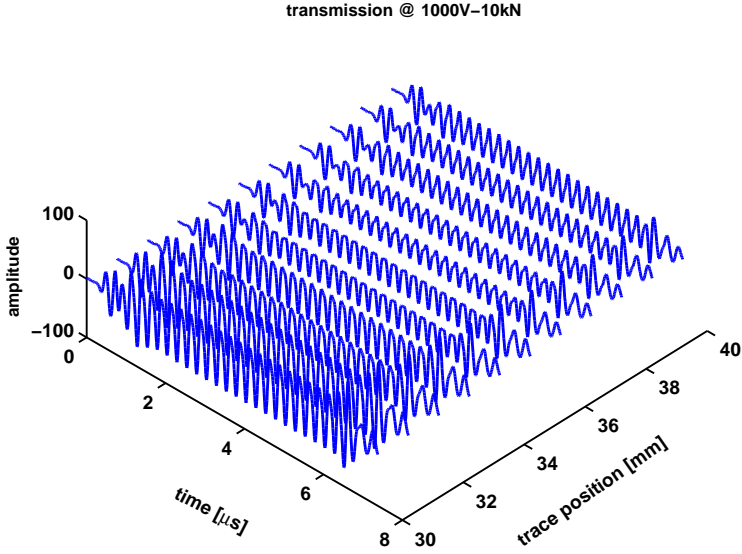


(a)

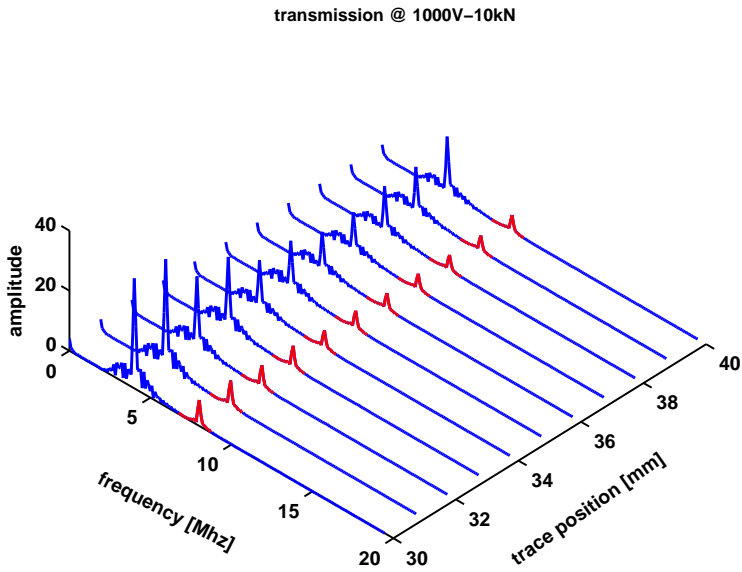


(b)

Figure D.9: Waveforms collected by the transmission channel C1–C2 at 10 kN between traces 30 and 40 (a) with the related frequency spectrum (b) at 800 V_{pp} and 24 cycles.



(a)



(b)

Figure D.10: Waveforms collected by the transmission channel C1 – C2 at 10 kN between traces 30 and 40 (a) with the related frequency spectrum (b) at 1000 V_{pp} and 24 cycles.

Bibliography

- Abeele, V. D., Johnson, P. A. & Sutin, A. M. (2000), 'Nonlinear elastic wave spectroscopy (NEWS) techniques to discern material damage. part I: Nonlinear wave modulation spectroscopy', *Res Nondestr Eval* **12**, 17–30.
- Biwa, S., Hiraiwa, S. & Matsumoto, E. (2006), 'Experimental and theoretical study of harmonic generation at contacting interface', *Ultrasonics* **44**, 1319–1322.
- Biwa, S., Nakajima, S. & Ohno, N. (2004), 'On the acoustic nonlinearity of solid-solid contact with pressure-dependent interface stiffness', *Journal of Applied Mechanics* **71**(4), 508–515.
- Bouakaz, A. & de Jong, N. (2003), 'Native tissue imaging at superharmonic frequencies', *IEEE Transactions on Ultrasonics, Ferroelectrics, and Frequency Control* **50**(5), 496–506.
- Brown, L. (2000), 'Dislocation plasticity in persistent slip bands', *Materials science and engineering* **A285**, 35–42.
- Bruneau, M. & Potel, C. (2012), *Materials and Scoustics Handbook*, ISTE Ltd.
- Buck, O., Morris, W. L. & Richardson, J. M. (1978), 'Acoustic harmonic generation at unbonded interfaces and fatigue cracks', *Applied Physics Letters* **33**(5), 371–373.
- Charlesworth, J. P. & Temple, J. A. G. (2001), *Engineering applications of ultrasonic time-of-flight diffraction*, second edn, North America Taylor and Francis Inc.
- de Raad, J. A. & Dijkstra, F. H. (2007), *Inspection of pipeline girth welds by AUT*, Applus RTD.
- Dijkstra, F. (2012), *Ultrasonic testing of austenitic welds and other coarse-grained, anisotropic materials*, Applus RTD.
- Drinkwater, B. W., Dwyer-Joyce, R. S. & Cawley, P. (1996), 'A study of the interaction between ultrasound and a partially contacting solid-solid interface', *Proceedings: Mathematical, Physical and Engineering Sciences* **452**(1955), 2613–2628.
- Fischer-Cripps, A. C. (2007), *Introduction to contact mechanics*, second edn, Springer Science + Business Media, LLC.

- Ginzel, E. (2006), *Automated ultrasonic testing for pipeline girth welds: A Handbook*, Olympus NDT.
- Gisolf, A. & Verschuur, E. (2011), *The principles of quantitative acoustical imaging*, EAGE Publications bv.
- Grierson, D. S., Flater, E. E. & Carpick, R. W. (2005), 'Accounting for the JKR-DMT transition in adhesion and friction measurements with atomic force microscopy', *Journal of Adhesion Science and Technology* **19**(3-5), 291–311.
- Griffiths, D. (2004), *Introduction to quantum mechanics*, second edn, Benjamin-Cummings Pub Co.
- Harumi, K. (1986), 'Computer simulation of ultrasonics in a solid', *NDT International* **19**(5), 315–332.
- Holmes, H., Drinkwater, B. W. & Wilcox, P. D. (2005), 'Post-processing of ultrasonic phased array data for optimal performance', *Insight* **47**(2), 88–90.
- Hörschens, L., Deleye, X. & Chougrani, K. (2013), 'Ultrasonic imaging of welds using boundary reflections', *AIP Conference Proceedings* **1511**, 1051–1058.
- Kim, N., Lee, T., Jhang, K. & Park, I. (2009), 'Nonlinear behavior of ultrasonic wave at crack', *AIP Conference Proceedings* **1211**, 313–318.
- Korshak, B., Solodov, I. Y. & Ballard, E. M. (2002), 'DC effects, sub-harmonics, stochasticity and "memory" for contact acoustic non-linearity', *Ultrasonics* **40**, 707–713.
- Krautkrämer, J. (1977), *Ultrasonic Testing of Materials*, second edn, Springer-Verlag Berlin Heidelberg New York.
- Kuttruff, H. (1991), *Ultrasonics fundamentals and applications*, Elsevier Science Publishers LTD.
- Maugis, D. (1991), 'Adhesion of spheres: The JKR-DMT transition using a Dugdale model', *Journal of Colloid and Interface Science* **150**(1), 243–296.
- Maugis, D. (1999), *Contact, Adhesion and Rupture of Elastic Solids*, Springer-Verlag Berlin Heidelberg New York.
- Mughrabi, H. (2002), 'On 'multi-stage' fatigue life diagrams and the relevant life-controlling mechanisms in ultrahigh-cycle fatigue', *Fatigue Fract Engng Mater Struct* **25**, 755–764.
- Ohara, Y., Mihara, T. & Yamanaka, K. (2006), 'Effect of adhesion force between crack planes on subharmonic and DC responses in nonlinear ultrasound', *Ultrasonics* **44**, 194–199.
- Olympus (2004), *Introduction to phased array ultrasonic technology applications*, Olympus NDT.
- Parsegian, V. A. (2006), *Van der Waals forces, A handbook for biologists, Chemists, Engineers, and Physicists*, first edn, Cambridge University Press.

- Pörtzgen, N. (2007), Imaging of defects in girth welds using inverse wave field extrapolation of ultrasonic data, PhD thesis, Delft University of Technology.
- Pörtzgen, N., Gisolf, A. & Blacquièrre, G. (2007), 'Inverse wave field extrapolation: a different NDI approach to imaging defects', *IEEE Transactions on Ultrasonics, Ferroelectrics, and Frequency Control* **54**(1), 118–126.
- Ravenscroft, F. A., Newton, K. & Scruby, C. B. (1991), 'Diffraction of ultrasound by cracks: comparison of experiment with theory', *Ultrasonics* **29**, 29–37.
- Reynolds, A. C. (1978), 'Boundary conditions for the numerical solution of wave propagation problems', *Geophysics* **43**(6), 1099–1110.
- Richardson, J. M. (1979), 'Harmonic generation at an unbonded interface-I. planar interface between semi-infinite elastic media', *International Journal of Engineering Sciences* **17**, 73–85.
- Ritchie, R. O. (1999), 'Mechanisms of fatigue-crack propagation in ductile and brittle solids', *International Journal of Solids* **100**, 55–83.
- Sasaki, R., Ogata, T., Ohara, Y., Mihara, T. & Yamanaka, K. (2005), 'Simulation and analysis of subharmonics and tail effect for ultrasonic nondestructive evaluation of closed cracks', *Japanese Journal of Applied Physics* **44**(6B), 4389–4393.
- Schijve, J. (2001), *Fatigue of Structures and Materials*, Kluwer Academic Publishers.
- Shapiro, R. S., Wagreich, J., Parsons, R. B., Stancato-Pasik, A., Yeh, H. C. & Lao, R. (1998), 'Tissue harmonic imaging sonography: Evaluation of image quality compared with conventional sonography', *American Journal of Roentgenology* **171**(5), 1203–1206.
- Solodov, I. Y. (1994), 'Nonlinear NDE using contact acoustic nonlinearity (CAN)', *Ultrasonic Symposium Proceedings* **2**, 1279–1283.
- Solodov, I. Y. (1998), 'Ultrasonics of non-linear contacts: propagation, reflection, and NDE-applications', *Ultrasonics* **36**, 393–390.
- Solodov, I. Y. (2010), 'Non-classical nonlinearity in solids for defect-selective imaging NDE', *IUTAM Symposium on Recent Advances of Acoustic Waves in Solids* **26**, 53–63.
- Solodov, I. Y., Krohn, N. & Busse, G. (2002), 'CAN: an example of nonclassical acoustic nonlinearity in solids', *Ultrasonics* **40**, 621–625.
- Suresh, S. (2003), *Fatigue of Materials*, second edn, University Press Cambridge.
- Sutton, M. A., Orteu, J. J. & Schreier, H. W. (2009), *Image correlation for shape, motion and deformation measurements, basic concepts, theory and applications*, Springer Science+Business Media, LLC.
- Verkooijen, J. & Boulavinov, A. (2005), 'Sampling phased array—a new technique for ultrasonic signal processing and imaging', *Insight* **50**(3), 153–157.
- Virieux, J. (1984), 'SH-wave propagation in heterogeneous media: Velocity-stress finite-difference method', *Geophysics* **49**(11), 1933–1957.

- Virieux, J. (1986), 'P-SV wave propagation in heterogeneous media: Velocity-stress finite-difference method', *Geophysics* **51**(4), 889–901.
- Wells, P. (2000), 'Current status and future technical advances of ultrasonic imaging', *IEEE Engineering in Medicine and Biology* pp. 14–20.
- Yamanaka, K., Mihara, T. & Tsuji, T. (2004), 'Evaluation of closed cracks by model analysis of subharmonic ultrasound', *Japanese Journal of Applied Physics* **43**(5B), 3082–3087.
- Yamanaka, K., Shintaku, Y., Oguma, M. & Ohara, Y. (2011), 'Two-dimensional analysis of subharmonic ultrasound generation at closed cracks by damped double nodes', *Applied Physics Express* **4** (076601).
- Yim, H. & Choi, Y. (2000), 'Simulation of ultrasonic waves in various types of elastic media using the mass spring lattice model', *Materials Evaluation* **58**(7), 889–896.
- Yim, H. & Sohn, Y. (2000), 'Numerical simulation and visualization of elastic waves using mass-spring lattice model', *IEEE Transactions on Ultrasonics, Ferroelectrics, and Frequency Control* **47**(3), 549–558.
- Zheng, Y., Maev, R. G. & Solodov, I. Y. (2000), 'Nonlinear acoustic applications for material characterization: A review', *Canadian Journal of Physics* **77**(12), 927–967.

Summary

Detection of cracks in fatigued components using conventional ultrasound is a major challenge in nondestructive testing. Due to fatigue loading and compressive stresses surrounding cracked areas, bridging between crack asperities may occur resulting in an acoustical transparent behavior of such cracks. To face this challenge and to increase detection capabilities of the existing inspection approach, various nondestructive techniques are applied and combined giving more insight into the crack response. Although these techniques are combined, difficulties in terms of detection and sizing of such cracks still remain.

This thesis describes a new ultrasonic approach, where non-linear features of acoustically transparent cracks are exploited. The basic principle in this approach is that the crack acts as a source of harmonics when it is excited at a certain frequency, carrying high ultrasonic amplitudes. This technique is called harmonic generation, and it is widely used in medical applications for enhanced imaging providing valuable information on the imaging target. For nondestructive testing, however, this technique is not yet implemented and far from maturity due to its complexity and hardware requirements. The key difference in both applications is the way by which harmonics are generated and exploited. In the case of nondestructive testing, only harmonics generated at a crack interface are considered, while in medical applications, higher harmonics arising from non-linear propagation are used.

Taking advantage from the contact acoustic non-linearity phenomenon at contacting interfaces, the presented work investigates crack closure and harmonic generation theoretically and experimentally. Related experiments are carried out on an artificial and a fatigue crack interface. To understand and explain some of the features observed in these experiments, a detailed modeling approach based on an adaptive mass-spring lattice scheme is presented. The proposed scheme uses a dynamic elasticity model derived from the van der Waals interaction force, which represents the stiffness of the cracked area. This dynamic elasticity is updated as a function of the opening and closing of the cracked cell element when interacting with an incident wavefield. Depending on the input frequency and the ratio between the crack opening and the strength of the excitation source, crack closure and harmonic generation are successfully modeled.

A major advantage of the proposed van der Waals elasticity model is the simplicity of computing the elasticity of a crack area directly from material properties at a given

crack opening. Implementation of this model in the mass-spring lattice model allows for a better understanding of the non-linear behavior of closed cracks and it explains relevant non-linear features observed in the performed experiments. The model is validated by comparing results from the simulated and real crack responses qualitatively and quantitatively. It is shown that, by updating the crack shape in the mass-spring lattice scheme, the simulated and the measured crack responses exhibit a good agreement in terms of amplitude, crack closure and harmonic generation along the crack length.

Reflection and transmission of ultrasonic waves through a crack interface strongly depends on the contact area between crack asperities and the excitation amplitude driving this contact. As a result, the magnitudes of the fundamental and the second harmonic may vary characterizing the level of non-linearity of such a contact. This information is valuable for the detection of (partially) closed cracks, especially when combining the fundamental and second harmonic data. Consequently, the probability of detection and sizing of such cracks improves sufficiently as imaging using harmonics becomes possible.

The outcome of this research, confirms the generation of harmonics at (partially) closed cracks and outlines the great potential of the proposed van der Waals elasticity model to understand the essential features revealed in the experiments. For the implementation of harmonic imaging in nondestructive testing, more investigations are required for achieving a practical setup allowing for non-linear measurements in field conditions (probes, wave generators, amplifiers, etc...). Another issue that remains and will play a role in the future is the acceptance of non-linear imaging technologies by the industry and by the codes and standards bodies regulating the application of new technologies in the world of nondestructive testing.

Samenvatting

In het niet-destructief onderzoek met behulp van conventionele ultrasone technieken is detectie van scheuren in installaties met vermoeiing een grote uitdaging. Als gevolg van vermoeiing en drukspanningen rondom gebieden met scheurvorming kan innig contact tussen scheurvlakken optreden, met als gevolg een akoestisch transparant gedrag van dergelijke scheuren. Om toch de detectiemogelijkheden van de huidige inspectie-aanpak te verbeteren worden diverse niet-destructieve technieken toegepast en gecombineerd, zodat meer inzicht in de respons van de scheur verkregen kan worden. Maar ondanks deze combinatie van technieken blijft detectie van dergelijke scheuren, en de bepaling van hun grootte, moeilijk.

Dit proefschrift beschrijft een nieuwe ultrasone aanpak, waarbij niet-lineaire eigenschappen van een akoestisch transparante scheur worden benut. Het basisprincipe van deze benadering is dat de scheur optreedt als een bron van harmonische componenten wanneer zij met een bepaalde frequentie wordt aangeslagen, gebruik makend van hoge ultrasone amplituden. Deze techniek wordt aangeduid als opwekking van harmonischen en wordt veel gebruikt in de medische toepassingen als verbetering van de huidige afbeeldingstechnieken, waarmee waardevolle informatie over het te inspecteren object verkregen kan worden. In het niet-destructief onderzoek is deze techniek nog niet geïmplementeerd vanwege zijn complexiteit en de gestelde hardware-eisen. Het belangrijkste verschil tussen beide toepassingen is de manier waarop harmonischen worden gegenereerd en gebruikt. Bij niet-destructief onderzoek worden alleen de harmonischen beschouwd die aan een scheurspleet worden opgewekt, terwijl in de medische toepassingen hogere harmonischen uit niet-lineaire propagatie worden benut.

In dit werk worden de sluiting van de scheur en de opwekking van harmonischen zowel theoretisch als experimenteel onderzocht, gebruik makend van akoestische niet-lineaire contactverschijnselen aan elkaar rakende oppervlakken. Daaraan gerelateerde experimenten zijn uitgevoerd op een kunstmatig spleet en een vermoeiingsscheur. Om de uitkomsten van deze experimenten te begrijpen en te verklaren wordt een gedetailleerd model voorgesteld, gebaseerd op een adaptief massa-veer-roostersysteem. Het voorgestelde schema maakt gebruik van een dynamisch elasticiteitsmodel, afgeleid uit het principe van de de van der Waals - interactiekracht, die de stijfheid van het gescheurde gebied voorstelt. Deze dynamische elasticiteit wordt bepaald als functie van het openen en sluiten van het gescheurde roosterelement, wanneer dit blootgesteld wordt aan een golfveld. Afhankelijk van de ingangsfrequentie en de verhouding tussen de scheuropening

en de sterkte van de excitatiebron worden scheursluiting en het opwekken van harmonischen met succes gemodelleerd.

Een groot voordeel van het voorgestelde van der Waals - elasticiteitsmodel is de eenvoud waarmee de elasticiteit van een scheurgebied, bij een bepaalde scheuropening, direct uit de materiaaleigenschappen berekend kan worden. De implementatie van dit model in het massa-veer-roostermodel zorgt voor een beter begrip van het niet-lineaire gedrag van gesloten scheuren en het verklaart relevante niet-lineaire eigenschappen die tijdens de experimenten werden waargenomen. Het model is gevalideerd door het vergelijken van de responses van een gesimuleerde scheur en een vermoeiingscheur, zowel kwalitatief als kwantitatief. Er wordt aangetoond dat door een aanpassing van de scheurvorm in het massa-veer-roostermodel, de gesimuleerde en de gemeten scheurresponses een goede overeenkomst vertonen in termen van amplitude, scheursluiting en opwekking van harmonischen langs de lengte van de scheur.

Reflectie en transmissie van ultrasone golven aan een scheurinterface zijn sterk afhankelijk van de grootte van de contactoppervlakte tussen de scheurvlakken en de excitatie-amplitude. Dit heeft tot gevolg dat de sterkten van de eerste en tweede harmonischen kunnen variëren, en als zodanig de mate van niet-lineariteit van de scheurvlakken kunnen karakteriseren. Deze waarneming is waardevol voor het detecteren van dergelijke scheuren, vooral wanneer de data van de eerste en tweede harmonischen worden gecombineerd. Hierdoor wordt de waarschijnlijkheid van detectie alsmede de groottebepaling van dergelijke scheuren voldoende verbeterd, doordat het maken van een afbeelding met gebruikmaking van harmonischen mogelijk wordt.

De uitkomst van dit onderzoek bevestigt het dat (gedeeltelijk) gesloten scheuren harmonischen opwekken en geeft de grote potentie van het voorgestelde van der Waals-elasticiteitsmodel aan voor het begrip van de essentiële waarnemingen uit deze experimenten. Voor het implementeren van harmonische afbeeldingen in het niet-destructief onderzoek is meer onderzoek vereist, om een praktische opstelling te kunnen realiseren die de meting van niet-lineaire verschijnselen mogelijk maakt (tasters, functiegeneratoren, versterkers, enz...). Een ander probleem dat blijft bestaan en in de toekomst een rol zal gaan spelen is de acceptatie van niet-lineaire afbeeldingstechnologieën door de industrie, en door de instanties die codes en normen opstellen die de toepassing van nieuwe technologieën in de wereld van het niet-destructief onderzoek reguleren.

Curriculum vitae



Khalid Chougrani was born in Morocco on April 15, 1976. After finishing his Bachelor's degree in Oujda University, Morocco, he followed a Master program in Applied Physics at Delft University of Technology, The Netherlands. After his Master's graduation, he joined Applus RTD. Since 2008, he is leading the Physics Team of the Technological Center, while he was conducting his PhD at Delft University of Technology.

Acknowledgements

Now, the PhD journey is finished, but let us start from the beginning...

My first contact with Applus RTD was in 2003 during my traineeship at the Technological Center. At that moment of time, I realized that Applus RTD is a great company and is the place to be with a huge potential for developing own skills, and serving the NDT industry by implementing advanced technologies. After one year of joining Applus RTD, the idea of initiating a PhD project beside my full-time job became very attractive, especially when we started a feasibility study on the inspection of deepwater risers. The complexity of detecting defects in some fatigued samples was the trigger to formulate a project plan on this topic, which was fully supported by my colleagues and the Technological Center management. Special thanks to Casper Wassink, Frits Dijkstra and Niels Pörtzgen for supporting the idea and for their technical advice. The next step was to find a dedicated research group, where the research topic could be supported and supervised. Thanks to the good cooperation with the Acoustical Wavefield Imaging at Delft University and their experience with a similar PhD project structure, I was very welcomed by Prof. Gisolf to start the research journey at his group. Special thanks to him and for his enthusiasm and guidance on the topic and the very fruitful discussions during our progress meetings. I would like to acknowledge Rienk de Vries for supporting me to make time during the last months of writing and finalizing the thesis. Special thanks to our CEO Iain Light who kept asking me about my defense date, while I was still working on the thesis. Now I proudly can say: It is on the 21st of February 2014, you are very welcome to attend the event and thank you for encouraging and supporting valuable technologies.

One of the challenges in this project was to design a mechanical setup to perform the measurements. Very special thanks to Nico 't Hooft for making time in the early mornings and detailing the setup design accurately. His experience and his enthusiasm were very important to make a robust and a reliable setup for the experiments. I liked his creative attitude for keeping sharpening and fine-tuning the setup and making it happen, whatever the challenge was. On the electronic side, I am grateful to Stefan Kleijer who managed to get the setup files ready for use. His flexibility and understanding of the electronics helped me to proceed on the experiments. Also thanks to Huib Rundberg who helped me with choosing and purchasing the equipment.

I would like to thank Leo Schröder who helped me in every step of the experiments and challenged me with "difficult questions" on the topic and for the nice time we spent in

the faculty lab of Aerospace Engineering in Delft. His practical insight and his enthusiasm were the key elements behind reliable and successful measurements. He was very creative even though during the scans by breaking the routine till the next scan starts.

Also many thanks to Berthil Grasholf the responsible of faculty lab, who facilitated and arranged the availability of the testing machine and helped me with all the preparations during the project. Many thanks to Paul van der Valk, Martin Verweij and Karel van Dalen for arranging the laser vibrometer, René Parie en Gerrit van Dijk for their input on the probe manufacturing. Many thanks to van der Klift who machined the steel block needed for the experiments and helped me to get the block ready in a short period of time. Special thanks to Humberto Figueroa of Shell Global Solutions in Houston for providing me with some fatigued samples.

On the theoretical side, there were challenges as well, I would like to thank Lars Hörchens for his theoretical support on modeling, laser vibrometer experiments and thesis review. I admired his practical and efficient approach to tackle the problem. Furthermore, I would like to thank, Eric Verschuur and Arno Volker for their feedback and advice on the modeling. Also, my acknowledgement to my team at Applus RTD and all colleagues for their motivation and interest in the research topic.

Many thanks to my room mates, Hannes Kutscha, Ahmad Ghazali, Gert-Jan van Groenestijn for the very nice times and discussions, especially on Friday's and during the cappuccino time. Hannes thank you for your help with Latex and your time when I had questions. We had a hard time in the evenings during our writing routines, but we were encouraging each other and finally succeeded to finish the thesis. Also thanks to Gabriel Lopez and Mikail Davydenko for keeping the room busy after the leave of Ahmad and Get-Jan. My thanks to Henry den Bok and Margaret van Fessem for their technical and administrative support during my working days at the university. Also my thanks to other TU Delft colleagues, Peter Haffinger, Nesli Ozmen, Alok Soy. Now, it is time to leave you and go back to the industry.

Last but not least, I am proud of my family, Mohamed, Sakina, Abdelkader, Yamina, Zoulikha, Ahmed, Mohamadine, Belcacem, El-Houcine, Abdenasser who motivated me when I was a child and supported me through the long journey with all the available means. Special thanks to friends, Ramdane, Mostafa, Abdelhafid, Abderrahime, Mourad, Mohamed, Ismail, Rabah, Azeddine with whom I shared my research challenges and other interesting topics. I would like to express my gratitude to my wife who directly experienced the last steps of my journey and motivated me through the last months to keep going, breathing and finally touching the finish-line.

In fact, the start of the journey wasn't 5 years ago, but It was earlier. I am proudly indebted to my parents who offered their life to make the impossible possible and helped us to reach the ultimate goal regardless time and place. My father passed away years before this moment of writing, but he had the patience and the feeling that this moment will come, and there I am now...

Delft, February 2014

Khalid Chougrani

Index

- atom-atom interaction, 17
- AUT, 6
- closed crack, 11, 13, 18, 19, 22, 27, 36–39, 72, 77–80
- Contact acoustic non-linearity, 18
- conventional techniques, 5, 10
- crack asperities, 10–13, 15, 22, 23, 36, 51, 59, 60, 67, 68, 72, 77
- crack closure, 11–15, 18, 19, 26, 27, 42, 46, 47, 51–53, 57, 59, 72, 77–79
- crack growth, 10, 11
- crack initiation, 10, 11, 13
- crack opening displacement, 22–24, 27
- crack transparency, 26, 27, 36, 72
- detection and sizing, 5, 8, 13, 18, 78–80
- dynamic elasticity, 13, 15, 22, 23, 27, 72, 77–79
- fatigue, 10, 11, 50–54, 72, 77, 78
- finite difference, 19
- fracture modes, 11
- harmonic generation, 77
- harmonic generation, 13–15, 18, 19, 26, 29, 30, 36, 42, 50, 53, 57, 59, 72, 77–79
- harmonic imaging, 10, 78–80
- imaging techniques, 5, 8, 79, 80
- IWEX, 8–10, 79, 80
- Lennard-Jones force, 84
- Lennard-Jones potential, 16, 19, 84
- mass-spring lattice model, 19, 20, 22, 23, 26, 72, 77, 79
- NDT, 5, 8, 10, 11, 13, 78, 80
- subharmonic generation, 19
- van der Waals forces, 13, 15, 16, 77
- van der Waals stress, 17, 84
- wave equation, 19, 26